A TECHNIQUE FOR THE MEASUREMENT OF RELATIVE VELOCITY BETWEEN

PARALLEL PLATE ELECTRODES IN MICROMACHINED STRUCTURES

Except where reference is made to the work of others, the work described in this dissertation is my own or was done in collaboration with my advisory committee. This dissertation does not include proprietary or classified information.

_____
Robert Neal Dean, Jr.

Certificate of Approval:

_____
George Flowers
Professor
Mechanical Engineering

_____
R. Wayne Johnson, Chair
Samuel Ginn Professor
Electrical & Computer Engineering

_____
A Scottedward Hodel
Associate Professor
Electrical & Computer Engineering

_____
Thaddeus A. Roppel
Associate Professor
Electrical & Computer Engineering

_____
Thomas A. Baginski
Professor
Electrical & Computer Engineering

_____
Stephen L. McFarland
Acting Dean
Graduate School

A TECHNIQUE FOR THE MEASUREMENT OF RELATIVE VELOCITY BETWEEN

PARALLEL PLATE ELECTRODES IN MICROMACHINED STRUCTURES

Robert Neal Dean, Jr.

A Dissertation

Submitted to

the Graduate Faculty of

Auburn University

in Partial Fulfillment of the

Requirements for the

Degree of

Doctor of Philosophy

Auburn, Alabama
May 11, 2006

A TECHNIQUE FOR THE MEASUREMENT OF RELATIVE VELOCITY BETWEEN

PARALLEL PLATE ELECTRODES IN MICROMACHINED STRUCTURES

Robert Neal Dean, Jr.

_____
Signature of Author

_____
Date of Graduation

VITA

Robert Neal Dean, Jr., son of Robert Neal, Sr. and Betty Jo (Killian), was born July 16, 1964 in Fanwood, New Jersey. He graduated from North Springs High School in Atlanta, Georgia in 1982. He received the degrees of Bachelor of Electrical Engineering and Master of Science in Electrical Engineering from Auburn University in 1988 and 1991, respectively. He worked for Dynetics, Inc. in their Fort Walton Beach, Florida office (1991-1992) and in their Huntsville, Alabama office (1992-1997) where he performed electronics development and data analysis. He then worked for SY Technology in Huntsville, Alabama (1997-1999) where he conducted MEMS research and development. In 1999, he was hired into the Center for Advanced Vehicle Electronics at Auburn University to conduct and manage microsystems research. He married Kristin (Anderson) Dean, daughter of William Alfred and Elaine Vicki Anderson on March 2, 1996. His children Jessica, Rebecca and Thomas were born June 15, 1998, June 5, 2001 and March 29, 2004, respectively.

DISSERTATION ABSTRACT

A TECHNIQUE FOR THE MEASUREMENT OF RELATIVE VELOCITY BETWEEN

PARALLEL PLATE ELECTRODES IN MICROMACHINED STRUCTURES

Robert Neal Dean, Jr.

Doctor of Philosophy, May 11, 2006
(M.S., Auburn University, 1991)
(B.E.E., Auburn University, 1988)

170 Typed Pages

Directed by R. Wayne Johnson

Numerous applications exist for microstructures that contain two parallel oriented electrodes that experience relative motion. It is often desirable to measure the relative velocity between the two electrodes and then utilize this information. Relative velocity can readily be measured in these types of microsystems if the relative motion of the electrodes is constrained such that the partial derivative of the capacitance between the electrodes with respect to the electrode separation distance is constant, by measuring the current flowing through the time varying capacitor. However, for electrostatic parallel plate actuators and other microstructures that experience similar motion, where the partial derivative of the capacitance between the electrodes with respect to the electrode

separation distance is time varying, this technique results in nonlinear distortion in the relative velocity measurement and is therefore not utilized.

In this dissertation, this relative velocity measurement technique is applied to electrostatic parallel plate actuator and similar microsystems, and the resulting nonlinearities inherent in this approach are investigated and characterized. It is shown that if the parallel electrodes experience small amplitude relative motion compared to the electrode separation distance at rest, then the nonlinear distortion in the relative velocity measurement is minimal and the total harmonic distortion estimation can be utilized to determine the minimum ratio of the electrode separation distance at rest to the amplitude of relative motion that can be tolerated for a particular application to obtain the required quality level in the relative velocity measurement. It is also shown that this technique accurately detects the direction of relative velocity even if the relative electrode motion is large compared to the electrode separation distance at rest. The results from experimentally validating the theoretical development through the testing of a prototype relative velocity sensor are also presented.

ACKNOWLEDGEMENT

Style manual or journal used: Auburn University Graduate School Guide to Preparation and Submission of Theses and Dissertations, Bibliography follows the style of IEEE Sensors Journal

Computer software used: Microsoft® Word 2002

TABLE OF CONTENTS

LIST OF FIGURES

xi

CHAPTER 1

INTRODUCTION

Numerous applications have been developed for parallel electrode microstructures that require the measurement or estimation of relative velocity between two or more electrodes. Examples include accelerometers [1], vibration control in a beam [2], enhancement of the stable operating range of parallel plate actuators [3, 4], advanced controller design for MEMS devices [5, 6 ,7] and active vibration isolation control laws that could be applied to microsystems [8]. In all of these examples where real systems were implemented, the relative velocity term was estimated using either an observer or recorded displacement measurements. The development and integration of a sensor for directly measuring the relative velocity between microstructures would simplify and/or improve each of these microdevices.

The contribution of this dissertation is the development and verification of a technique, suitable for use with parallel electrode microstructures experiencing translational motion normal to their opposing faces, to detect the direction of relative velocity or to measure the absolute relative velocity between the two microstructures and to determine under what conditions the technique can be applied. Senturia [9] presented a technique for measuring relative velocity between two electrodes in motion by applying a constant voltage across the capacitor formed by the two electrodes and then measuring

the current flowing through the capacitor. When the partial derivative of capacitance with respect to electrode separation distance ($\partial C/\partial x$) is constant, as is the case with tangential electrostatic actuators such as comb drive actuators, the current flowing through the capacitor is linearly proportional to the relative velocity between the two electrodes. However, for parallel plate actuators and other microstructures with similar motion, $\partial C/\partial x$ is not constant, which introduces nonlinear distortion into the measurement. The technique for measuring relative velocity explained in this dissertation applies the technique described by Senturia [9] to these applications where $\partial C/\partial x$ is not constant and explores the limitations of this approach.

The remainder of this dissertation is organized as follows. Chapter 2 presents a detailed literature review of electrostatic microelectromechanical systems, including published techniques for measuring relative displacement and relative velocity between microstructures. The research objectives are presented at the end of Chapter 2. Chapter 3 presents the theoretical development of the technique for measuring relative velocity between parallel electrodes in translational motion normal to their opposing faces. Chapter 4 presents the development of a prototype relative velocity sensor that was used to verify the theoretical technique for measuring relative velocity that was developed in Chapter 3. Chapter 5 presents the test set up, test procedure, recorded data and analysis results from evaluating the prototype relative velocity sensor described in Chapter 4. The conclusions obtained from this research are presented in Chapter 5. Recommendations for future research are presented in Chapter 6. The appendix contains supporting material that is referenced throughout this dissertation.

CHAPTER 2

DETAILED LITERATURE REVIEW

The area of research covered in this literature review relates to the broad topic of electrostatic microelectromechanical systems (MEMS). Specifically, the topics of capacitive microstructures, electrostatic parallel plate actuators, electrostatic comb drive actuators, system modeling of MEMS structures, relative displacement measurement in MEMS devices and relative velocity measurement in MEMS devices are covered in detail. The coverage includes both a solid introduction to the technology and a discussion of the current state of the art through recent publications. The fundamental groundwork laid out in this chapter leads into the theoretical development of a relative velocity sensor for parallel electrode microstructures in Chapter 3.

2.1 Capacitive Microstructures

Single crystal silicon substrates are commonly utilized to realize MEMS devices. Fabrication processes such as deep reactive ion etching (DRIE), wafer bonding, HF release of devices patterned into the device layer of silicon-on-insulator (SOI) wafers, etc… are well suited for realizing parallel plate capacitors where doped silicon is used for the electrodes. Thin film metal electrodes can also be utilized in MEMS devices, either

structurally as the electrode or as the conductive coating on an otherwise nonconductive electrode structure. A simple parallel plate capacitor is illustrated in Figure 2.1 and can be described by the first order model

$$C = \frac{\varepsilon_o \varepsilon_r A}{d},$$
(2.1)

where C is the calculated capacitance between two parallel plate electrodes of area A and separation distance d, with a dielectric material between the two electrodes whose permittivity is modeled by $\varepsilon_o \varepsilon_r$ [10]. It should be pointed out that this model ignores the effects of fringing, which can result in greater capacitance than predicted in (2.1). Consider the calculated capacitance of a unit micro-capacitor, with square electrodes that are 1μm across and separated by 1μm in a vacuum. Using (2.1), this micro-capacitor has an estimated capacitance of only 0.008854fF.
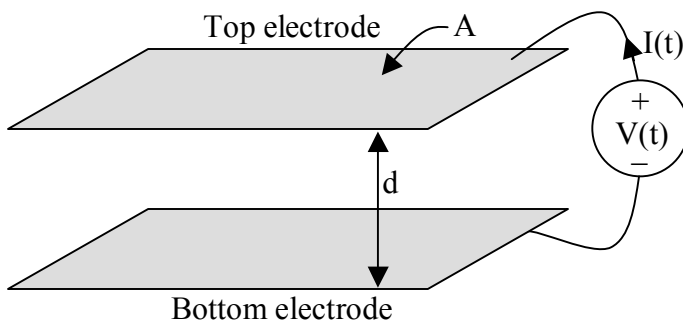
Figure 2.1. An illustration of a simple parallel plate capacitor.

Consider a realistic vertical capacitor fabricated between a patterned device layer and the handle layer of an SOI wafer after the 1µm thick box layer between the electrodes has been removed. A reasonable size electrode area could be a square that is 100µm across. The calculated capacitance in a vacuum is therefore 88.54fF. Furthermore, assume that the device layer is 150µm thick and two of the four sides are used to realize horizontal capacitors with other structures patterned in the device layer, as illustrated in Figure 2.2. The "floating" structure in the middle of the device layer is assumed to be attached to supports outside the plane of the drawing. When the hypothetical device is at rest, the two horizontal capacitors, C_1 and C_2, are equal and each has a calculated capacitance of 16.601fF.
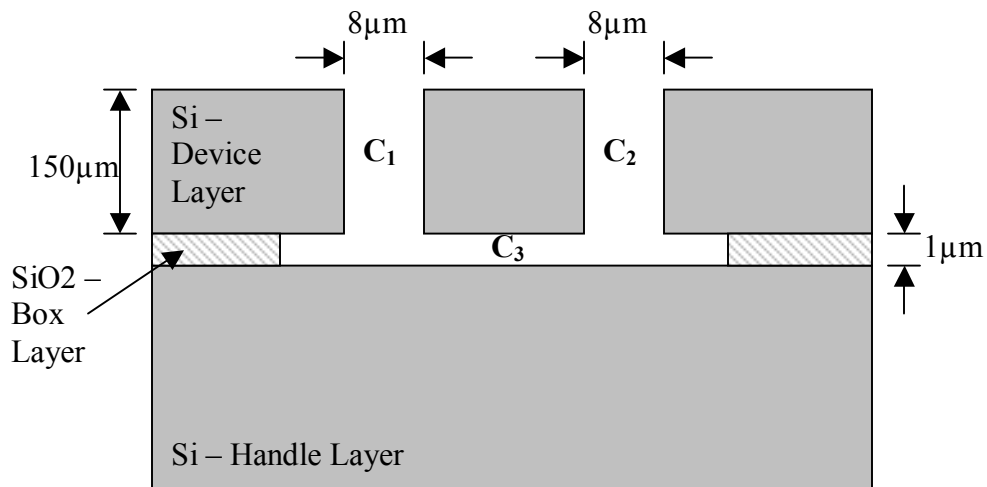
Figure 2.2. An illustration of a microfabricated device with horizontal and vertical capacitors.

Now consider the case where the center structure in the device layer can move horizontally such that C_1 gets larger as C_2 gets smaller, and that the range of motion is

limited to -7.9μm to 7.9μm. Figure 2.3 presents the calculated capacitances for C_1 and C_2 as a function of the C_1 electrode separation distance. The capacitances for C_1 and C_2 range from 8.35fF to 1328.1fF over the specified range of motion.

C1 and C2 Vs C1 Electrode Distance
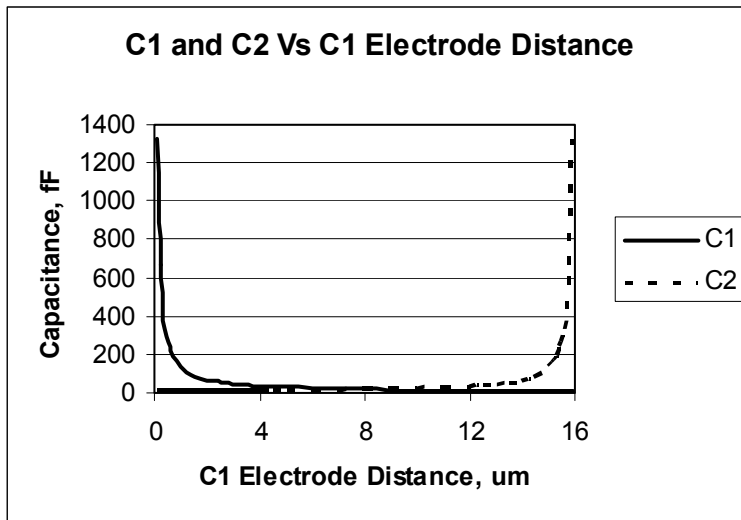
Figure 2.3. A plot of C_1 and C_2 as a function of the C_1 electrode separation distance.

Suppose that the displacement of the middle structure in the device layer is measured using an AC voltage divider consisting of C_1 and C_2, as illustrated in Figure 2.4, where the stationary electrode of C_2 is the AC voltage source input, the stationary electrode of C_1 is grounded and the output signal is measured off of the movable structure in the middle of the device layer. For a 1V sinusoidal input to the voltage divider, a plot of Vout over the possible range of motion is presented in Figure 2.5. The response is linear as a function of the horizontal motion of the middle structure in the device layer.
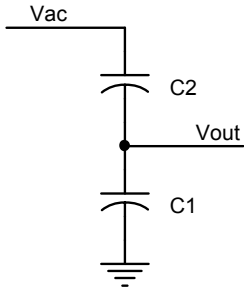
Figure 2.4. A schematic diagram of the AC voltage divider utilized to measure displacement.
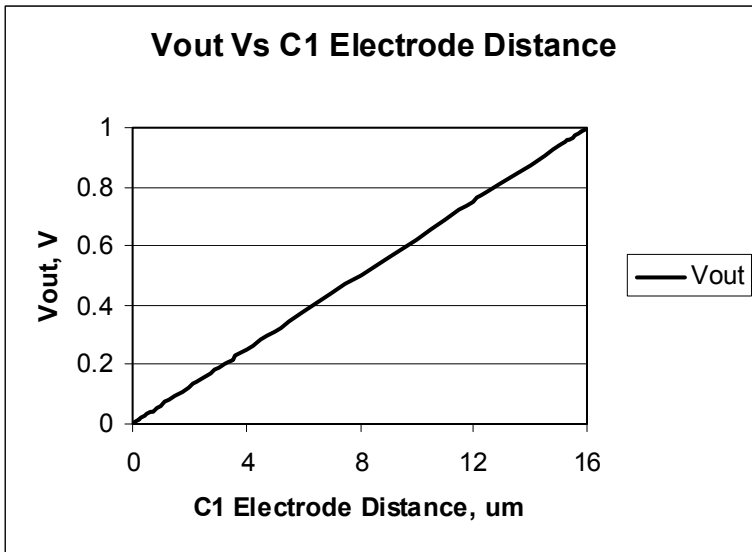
Figure 2.5. A plot of the output voltage from the AC voltage divider versus C1 electrode separation distance for a 1V sinusoidal input.

Now consider the effect of C_3 if the handle layer is grounded. C_3 is now electrically in parallel with C_1, as illustrated in Figure 2.6. Ignoring fringing effects in the calculation of C_3, so that C_3 is modeled as a constant capacitance of 88.54fF over the entire range of motion, then Figure 2.7 presents the response of the voltage divider when

7

C_3 is included in the electrical model. The resulting output voltage has a smaller dynamic range and is a nonlinear function of the motion of the middle structure in the device layer due to the effects of the stray capacitance modeled by C_3.
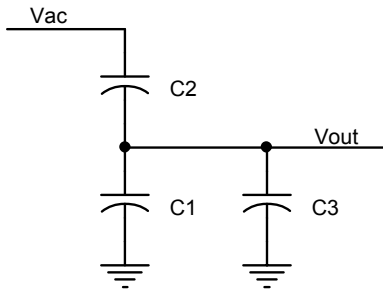
Figure 2.6. A schematic diagram of the AC voltage divider utilized to measure displacement with C_3 included in the model.
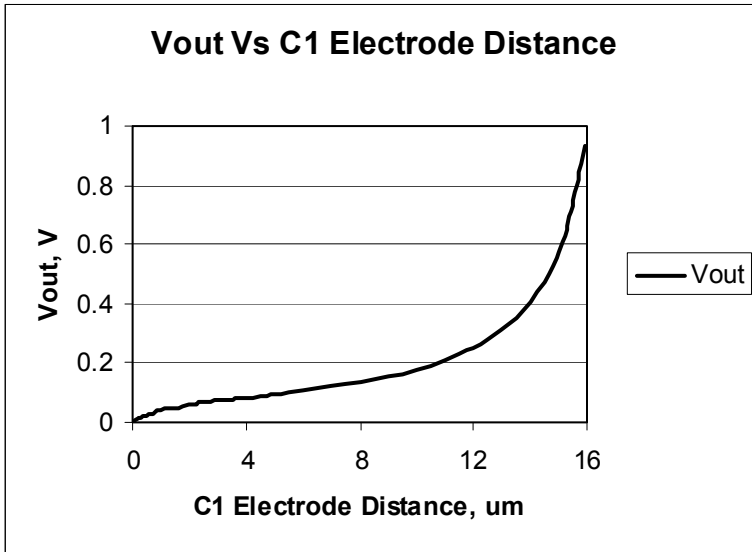
Figure 2.7. A plot of the output voltage from the AC voltage divider versus C1 electrode separation distance for a 1V sinusoidal input with C_3 included in the model.

Due to the relatively small values of capacitance encountered in MEMS structures, every effort should be made to minimize the effects of stray capacitance. This includes careful layout of the fabricated structure or structures; careful selection of which features to inject signals into, to read signals from, to ground or to leave floating; and locating the interface electronics as close as possible to the MEMS structure. Direct attachment of the interface electronics die to the MEMS device die is a good practice whenever possible.

2.2 Electrostatic Parallel Plate Actuators

The simplest electrostatic parallel plate actuator (PPA) consists of two parallel plate electrodes where one electrode is fixed and the other is able to move toward or away from the fixed electrode, as illustrated in Figure 2.8. The motion of the movable electrode is restrained by one or more springs. When the voltage across the electrodes is zero, the electrostatic force between the electrodes is also zero, resulting in a rest electrode separation distance, x_o, also called the rest gap distance. As the voltage between the two electrodes is increased from zero, the resulting electrostatic force between the two electrodes pulls the movable electrode toward the fixed electrode until the electrostatic force equals the spring force.

Bao [11] gave an excellent discussion on the derivation of the equation for the electrostatic force produced in a PPA and on the limits of stable operation, which are summarized below. The energy stored in the PPA capacitance, E_c, at any position, $x_o - x$, is

$$E_c = \frac{CV_s^2}{2}.$$ (2.2)
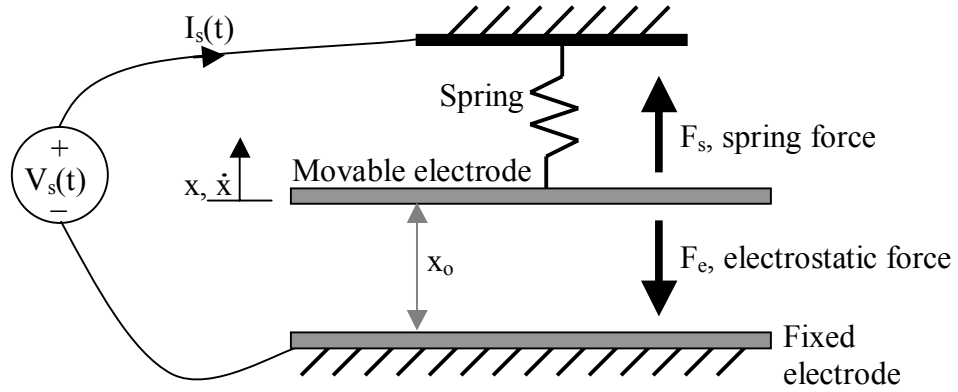
Figure 2.8. An illustration of an electrostatic parallel plate actuator.

Substituting (2.1) into (2.2) yields

$$E_c = \frac{\varepsilon_o \varepsilon_r A V_s^2}{2d}.$$ (2.3)

However, since

$$d = x_o + x$$ (2.4)

then

$$E_c = \frac{\varepsilon_o \varepsilon_r A V_s^2}{2(x_o + x)}.$$ (2.5)

10

If the top electrode is allowed to move an infinitesimally small distance, Δx, toward the bottom electrode while the voltage across the electrodes, $V_s(t)$, is held constant, the actuator will gain energy and the power supply will give up internal energy. Therefore the energy balance equation becomes

$$F_e \Delta x = \frac{dE_c}{dx} \Delta x - \frac{dE_p}{dx} \Delta x , \qquad (2.6)$$

where $F_e \Delta x$ equals the energy gained by the PPA capacitance minus the internal energy lost by the power supply. By dividing both sides of (2.6) by Δx, the equation for F_e can be simplified to

$$F_e = \frac{dE_c}{dx} - \frac{dE_p}{dx} , \qquad (2.7)$$

where

$$\frac{dE_c}{dx} = \frac{V_s^2}{2} \frac{\partial C(x)}{\partial x} = -\frac{V_s^2 \varepsilon_o \varepsilon_r A}{2(x_o + x)^2} \qquad (2.8)$$

and

$$\frac{dE_p}{dx} = V_s \frac{\partial q(x)}{\partial x} . \qquad (2.9)$$

11

But since

$$q(x) = C(x)V_s,$$
(2.10)

therefore

$$\frac{dE_p}{dx} = V_s^2 \frac{\partial C(x)}{\partial x} = -\frac{V_s^2 \varepsilon_o \varepsilon_r A}{(x_o + x)^2}.$$
(2.11)

Substituting the results of (2.9) and (2.11) into (2.7) yields the equation for the electrostatic force

$$F_e = -\frac{V_s^2 \varepsilon_o \varepsilon_r A}{2(x_o + x)^2} + \frac{V_s^2 \varepsilon_o \varepsilon_r A}{(x_o + x)^2} = \frac{V_s^2 \varepsilon_o \varepsilon_r A}{2(x_o + x)^2}.$$
(2.12)

Observe that the electrostatic force is proportional to the drive voltage squared, but it is also inversely proportional to the electrode separation distance squared. Referring back to the illustration of a simple PPA in Figure 2.8, where the movable electrode has a mass, m, and the mechanical system has damping which can be modeled by c, the equation describing the system dynamics is

$$m\ddot{x} + c\dot{x} + kx = -F_e.$$
(2.13)

The negative sign in front of F_e results from the definition that a positive electrostatic force results in a movable electrode motion in the negative x direction, as defined in Figure 2.8.

After a small constant nonzero voltage, V_s, has been applied to the actuator and the movable electrode velocity has decayed to zero, the resulting force balance equation is

$$kx = -\frac{\varepsilon_o \varepsilon_r A V_s^2}{2(x_o + x)^2},$$
(2.14)

where k is the system spring constant. If the applied voltage is slowly increased from zero, two solutions exist for x, which yield two equilibrium points, one stable and one unstable. For an applied voltage just greater than zero, the stable equilibrium point resides almost at x = 0, while the unstable equilibrium point resides almost at the x = x_o. As the voltage is further increased, the two equilibrium points move toward each other and finally converge into one unstable equilibrium point. This equilibrium point convergence occurs when the electrode separation distance equals one third of the rest gap distance, x_o. The voltage at which this occurs is called the pull-in voltage, V_{pi}, where

$$V_{pi} = \sqrt{\frac{8kx_o^3}{27\varepsilon_o \varepsilon_r A}}.$$
(2.15)

13

A voltage equal to or greater than V_{pi} results in an unstable condition where the movable electrode snaps into contact with the fixed electrode. This occurs because the spring force is now always less than the electrostatic force. Therefore for open loop operation, the PPA range of motion is limited to less than one third of x_o. Several techniques have been developed to increase the stable operating range of motion, but they usually result in a penalty such as higher required operating voltage [12, 13].

PPAs have been utilized in numerous applications in MEMS devices. Examples include individual mirror elements in reflective spatial light modulators [14], movable lenses for optical and hard disk drives [15, 16], miniature active vibration isolation mounts [17], seismic mass position control in accelerometers [18], the actuator for micro-grippers [19], levitation control of micro elements [20] and actuators for tunable RF devices [21, 22].

2.3 Electrostatic Comb Drive Actuators

Consider the parallel plate capacitor illustrated in Figure 2.9, where two flat, parallel electrodes of width b are kept a fixed distance apart, d_o, but are allowed to move in the direction of x. The motion experienced by the electrodes is referred to as tangential electrode motion. If a voltage, $V_s(t)$, is applied across the electrode pair, the resulting electrostatic force produces a tangential force on the movable electrode that attempts to increase the amount of electrode overlap to 100%, which maximizes the capacitance under the presumed constraints.

14
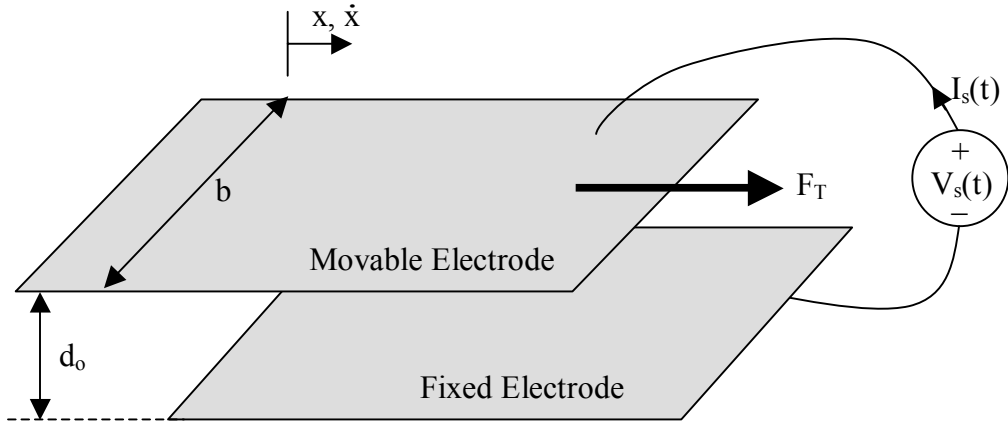
Figure 2.9. An illustration of tangential capacitive electrode motion.

Following the energy balance equation set forth in (2.6), with the exception that F_T, the electrostatic tangential force, is in the same direction as positive displacement, then if the movable electrode is moved an infinitesimally small distance, Δx, in the positive x direction, the energy balance equation becomes

$$-F_T \Delta x = \frac{dE_c}{dx} \Delta x - \frac{dE_p}{dx} \Delta x ,$$

(2.16)

which can be rearranged to yield

$$F_T \Delta x = \frac{dE_p}{dx} \Delta x - \frac{dE_c}{dx} \Delta x ,$$

(2.17)

which states that $F_T\Delta x$ equals the energy lost by the power supply minus the energy gained by the tangential actuator capacitance. Equation (2.17) can be reduced to

$$F_T = \frac{dE_p}{dx} - \frac{dE_c}{dx}.$$

<div align="right">(2.18)</div>

The equation for capacitance of the tangential actuator as a function of x is

$$C(x) = \frac{\varepsilon_o \varepsilon_r bx}{d_o}.$$

<div align="right">(2.19)</div>

Therefore if $V_s(t)$, is held constant, then

$$\frac{dE_p}{dx} = V_s^2 \frac{\partial C(x)}{\partial x} = \frac{V_s^2 \varepsilon_o \varepsilon_r b}{d_o}$$

<div align="right">(2.20)</div>

and

$$\frac{dE_c}{dx} = \frac{V_s^2}{2} \frac{\partial C(x)}{\partial x} = \frac{V_s^2 \varepsilon_o \varepsilon_r b}{2d_o}.$$

<div align="right">(2.21)</div>

Substituting (2.20) and (2.21) into (2.18) yields the equation for the tangential electrostatic force

$$F_T = \frac{V_s^2 \varepsilon_o \varepsilon_r b}{d_o} - \frac{V_s^2 \varepsilon_o \varepsilon_r b}{2d_o} = \frac{V_s^2 \varepsilon_o \varepsilon_r b}{2d_o} \ . \tag{2.22}$$

Observe that the force produced by the tangential electrostatic actuator is proportional to the applied voltage squared, but is not a function of the displacement. Therefore, for a movable electrode with a mass, m, that is restrained by a spring system with a system spring contact, k, with system mechanical damping modeled by c, the equation describing the system dynamics is

$$m\ddot{x} + c\dot{x} + kx = F_T \ . \tag{2.23}$$

After a small constant nonzero voltage, V_s, has been applied to the actuator and the movable electrode velocity has decayed to zero, the resulting force balance equation is

$$kx = \frac{V_s^2 \varepsilon_o \varepsilon_r b}{2d_o} \ , \tag{2.24}$$

Therefore unlike the PPA, the tangential actuator does not experience an unstable condition where the electrostatic force is always greater than the spring force after a certain displacement has been reached.

Consider the device illustrated in Figure 2.10 that consists of two interdigitated comb structures, where one comb is fixed in position while the other comb is allowed to

move into the fixed comb against the restraining force of two springs. When a voltage, $V_s(t)$, is applied across the two comb structures, the cumulative tangential electrostatic force from the interdigitated fingers pulls the movable comb structure into the fixed comb structure against the spring force. This type of electrostatic tangential force actuator is called a comb drive actuator.
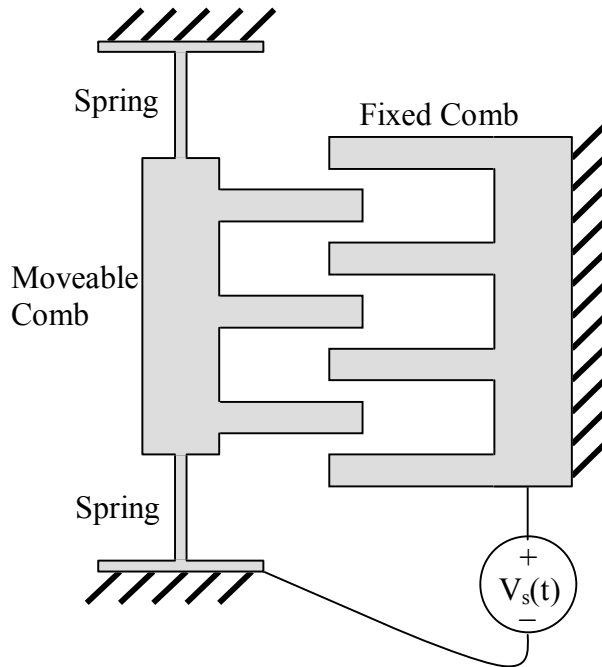
Figure 2.10. An illustration of a comb drive actuator.

According to Bao [11], the composite electrostatic force of a comb drive actuator can be modeled by

$$F_T = \frac{n\beta b \varepsilon_o \varepsilon_r V_s^2}{d_o},$$ (2.25)

where F_T is the composite tangential electrostatic force that pulls the movable comb structure into the fixed comb structure, n is the number of utilized teeth in the movable comb, β is a correction factor the accounts for the effects of fringing, b is the overlapping height of the comb teeth, $\varepsilon_o \varepsilon_r$ is the permittivity of the dielectric material between the comb teeth, $V_s(t)$ is the drive voltage and d_o is the fixed distance between the movable comb teeth and the fixed comb teeth. As with the two-electrode tangential actuator previously discussed, the comb drive actuator does not experience an unstable condition in the direction of motion where the spring force is always less than the electrostatic force beyond a certain displacement. However, stability issues do arise with regard to the lateral motion of the movable comb relative to the fixed comb as the drive voltage is increased [23]. When this occurs, the movable comb structure can be pulled laterally into contact with the fixed comb structure.

Many variants of the comb drive actuator have been developed, including comb drive actuators that produce rotary motion [24], comb drive actuators that produce motion normal to the plane of the substrate [25], comb drives with teeth of various shapes to tailor the composite electrostatic force [26] and comb drives actuators where the length of the individual teeth varies across one of the comb structures [27]. Comb drive actuators have been utilized in many applications, including resonators [28], microengines [29], positioning of micro-optics [30], tunable capacitors [31] and inertial sensors [32].

19

2.4 System Modeling of MEMS Structures

Many passive micromachined structures consist of floating structures that are suspended from fixed anchor points by beams. Active micromachined structures generally consist of similar passive structures with one or more integrated actuators. The floating structures and the anchors are generally considered to be rigid, while the beams are treated as elastic springs. The rigid floating structure is modeled by a mass, m, while the composite effect of the springs is lumped into a linear system spring constant, k. The micromachined structure possesses damping from internal sources such as thermoelastic damping [33] and from external sources such as squeeze film damping [34]. The composite damping effects are modeled by a single linear damping term, c. As illustrated in Figure 2.11, the complex micromachined structure is modeled by a linear second order spring-mass-damper system.
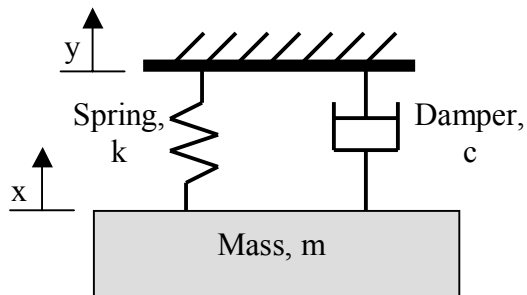
Figure 2.11. An illustration of a MEMS device modeled as a linear second order spring-mass-damper system.

In many applications, the input to a microsystem is a physical displacement to the anchor or frame, y(t), and the output is the displacement of the floating structure, x(t).

20

However, even in systems where this is not the case, this model is useful for evaluating the motion of floating structures due to disturbances to the system resulting from external forces acting on the frame. The differential equation describing the system dynamics is

$$m\ddot{x} + c(\dot{x} - \dot{y}) + k(x - y) = 0. \tag{2.26}$$

Therefore the transfer function is

$$T(s) = \frac{X(s)}{Y(s)} = \frac{\dfrac{\omega_n}{Q}s + \omega_n^2}{s^2 + \dfrac{\omega_n}{Q}s + \omega_n^2}, \tag{2.27}$$

where ω_n is the natural frequency of the second order system model and can be calculated from

$$\omega_n = \sqrt{k/m} \tag{2.28}$$

and Q is the system quality factor and can be calculated from

$$Q = \frac{\sqrt{km}}{c}. \tag{2.29}$$

The quality factor, Q, can be replaced by ζ, the damping coefficient, using the following relationship

$$\varsigma = \frac{1}{2Q} \, .$$

(2.30)

The magnitude response of (2.27) is called the transmissibility [35] and is

$$|T(j\omega)| = \frac{\sqrt{(\frac{\omega_n \omega}{Q})^2 + \omega_n^4}}{\sqrt{(\omega_n^2 - \omega^2)^2 + (\frac{\omega_n \omega}{Q})^2}}$$

(2.31)

and the phase response is

$$\theta = \tan^{-1}(\frac{(\omega/\omega_n)^3}{Q((1 - \omega/\omega_n)^2 + (\omega/\omega_n Q)^3)}) \, .$$

(2.32)

Figure 2.12 presents a graph of several plots of the transmissibility for various values of Q where the natural frequency, f_n, has been normalized to 1Hz.
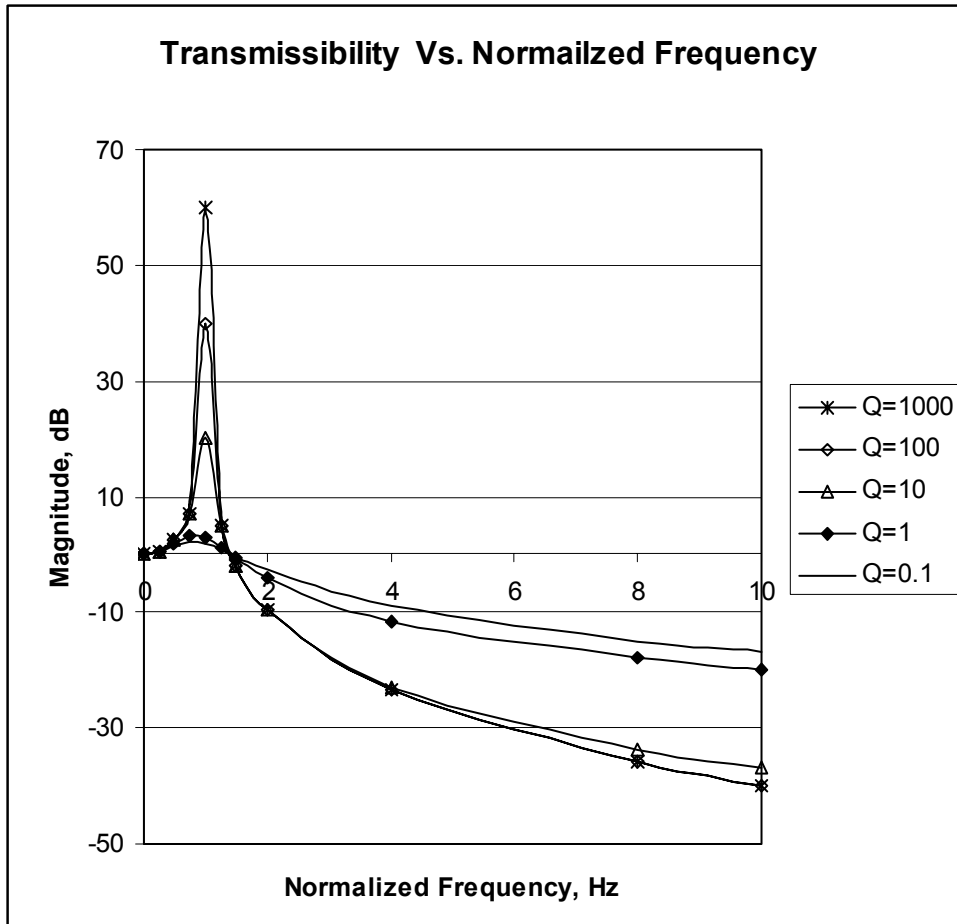
Figure 2.12. A graph of several plots of the transmissibility for various values of Q for a normalized natural frequency of 1Hz.

Although the magnitude response in Figure 2.12 is a second order low-pass filter response, the zero in the numerator of (2.27) results in some interesting properties. When $Q \geq 5$, the magnitude of ($T(j\omega)$) at the natural frequency, ω_n, is approximately equal to Q, the system quality factor. Also, the magnitude of ($T(j\omega)$) is always greater than one at the natural frequency, ω_n, for any value of Q. The stopband attenuation is dependent on the value of Q. Consider the stopband response for three values of Q, 1, 10 and 1000.

23

For Q = 1, the attenuation between $2\omega_n$ and $20\omega_n$ is 21.85dB, which is approximately the attenuation achieved in a first order lowpass system. For Q = 10, the attenuation between $2\omega_n$ and $20\omega_n$ is 35.64dB. For Q = 1000, the attenuation between $2\omega_n$ and $20\omega_n$ is 42.48dB, which is approximately the attenuation achieved in a second order low pass system.

Suppose that an actuator is utilized to apply a force to the spring mass damper such that

$$m\ddot{x} + c(\dot{x} - \dot{y}) + k(x - y) = f(x - y, \dot{x} - \dot{y}). \qquad (2.33)$$

Furthermore, suppose that the force can consist of two terms, where one term is proportional to the measured relative displacement and the second term is proportional to the measured relative velocity between the floating structure and the frame, such that

$$m\ddot{x} + c(\dot{x} - \dot{y}) + k(x - y) = k'(x - y) + c'(\dot{x} - \dot{y}). \qquad (2.34)$$

For the first case where only the relative displacement measurement is utilized in a linear feedback control law, the differential equation describing the system dynamics is

$$m\ddot{x} + c(\dot{x} - \dot{y}) + k(x - y) = k'(x - y) \qquad (2.35)$$

where k' is a constant gain proportional to the relative displacement between the floating structure and the frame. The transfer function is therefore

24

$$T(s) = \frac{X(s)}{Y(s)} = \frac{\dfrac{\omega'_n}{Q'}s + \omega'^2_n}{s^2 + \dfrac{\omega'_n}{Q'}s + \omega'^2_n},$$ (2.36)

where

$$\omega'_n = \sqrt{\frac{k-k'}{m}}$$ (2.37)

and

$$Q' = \frac{\sqrt{(k-k')m}}{c}$$ (2.38)

Therefore position or relative displacement feedback can be utilized to adjust the natural frequency and the quality factor, but not independently.

For the second case where only the relative velocity information is utilized in a linear feedback control law, the differential equation describing the system dynamics is

$$m\ddot{x} + c(\dot{x} - \dot{y}) + k(x - y) = c'(\dot{x} - \dot{y})$$ (2.39)

where c' is a constant gain proportional to the relative velocity between the floating structure and the frame. The transfer function for this case is

$$T(s) = \frac{X(s)}{Y(s)} = \frac{\dfrac{\omega_n}{Q'}s + \omega_n^2}{s^2 + \dfrac{\omega_n}{Q'}s + \omega_n^2}, \tag{2.40}$$

where

$$\omega_n = \sqrt{\frac{k}{m}} \tag{2.41}$$

and

$$Q' = \frac{\sqrt{km}}{c - c'}. \tag{2.42}$$

With velocity feedback, the quality factor can be adjusted without affecting the natural frequency.

The third case is when both relative position and relative velocity measurements are utilized, with the resulting transfer function being

$$T(s) = \frac{X(s)}{Y(s)} = \frac{\dfrac{\omega'_n}{Q'}s + \omega'^2_n}{s^2 + \dfrac{\omega'_n}{Q'}s + \omega'^2_n}, \tag{2.43}$$

where

$$\omega'_n = \sqrt{\frac{k - k'}{m}}$$
(2.44)

and

$$Q' = \frac{\sqrt{(k - k')m}}{c - c'}.$$
(2.45)

A control law that utilizes both relative position and relative velocity feedback allows both the natural frequency and the quality factor to be independently adjusted.

2.5 Relative Displacement Measurement in MEMS Devices

A number of techniques are commonly used to measure relative displacement in MEMS devices. Piezoresistive techniques can be used to indirectly measure deflection of micromachined structures [36]. Piezoresistors are strain gauges that change in resistance as they are physically strained, i.e. as they experience a dimensional change. The gauge factor (GF) is a dimensionless measure of the relative change in resistance compared to a relative change in a dimension. For example, the gauge factor for a relative change in length of a piezoresistor is expressed as

$$GF = \frac{\Delta R / R}{\Delta L / L},$$
(2.46)

where R is the nominal resistance, ΔR is the change in resistance, L is the nominal length and ΔL is the change in length. Metal foil and thin-film metal strain gauges have been used for many years and possess gauge factors ranging from one to five. The piezoresistive effect in metal strain gauges is primarily due to dimensional changes in the device as it is strained. Semiconductor strain gauges, however, posses much higher gauge factors than metallic strain gauges, with gauge factors as large as 200 for p-type silicon and -140 for n-type silicon. The piezoresistive effect in semiconductor strain gauges is primarily due to changes in the majority carrier mobilities in the device as it is strained. Depending on the type of doping used, semiconductor strain gauges can have positive or negative gauge factors. Semiconductor strain gauges are also very dependant on crystal plane orientation and are much more sensitive to temperature than metal strain gauges. Full-active Wheatstone resistive bridge structures can be realized by either fabricating two p-type and two n-type semiconductor piezoresistors on the same device or by careful orientation of four semiconductor piezoresistors of the same type, for micro-structure displacement measurement. The Hygrometrix HMX2000 micromachined silicon humidity sensor uses this technique to measure ambient relative humidity by detecting the strain in four micromachined beams that are coated with a polymeric material that strains each beam in proportion to the amount of absorbed moisture [37]. Each beam has an integrated piezoresistive strain gauge, where two of the beams have positive gauge factor strain gauges while the other two beams have negative gauge factor strain gauges. The four strain gauges are electrically connected to realize a Wheatstone bridge.

28

Optical techniques can also be used to measure displacements in MEMS devices. Borovic et al [38] described an electrostatic actuator driven MEMS device that utilized optical modulation to sense displacement. Specifically, two comb drive actuators were used to move a shutter which modulated a beam of light between a laser diode and a photodetector. The output voltage from the photodetector was then used to determine the displacement of the shutter assembly.

Displacement or position measurement can be accomplished by measuring the capacitance across an electrostatic actuator and comparing the measurement to an accurate model of the actuator. A similar technique is to fabricate a second capacitor, called the sense capacitor, physically in parallel with the electrostatic actuator, but electrically isolated from it, and then determine the displacement of the electrostatic actuator by measuring the displacement of the sense capacitor. This architecture isolates the displacement measurement circuitry from the actuator drive voltage circuitry, which allows low voltage measurement circuitry and high voltage actuator drive circuitry. Baxter [39] described a technique for measuring capacitance suitable for this architecture, where the displacement was measured by realizing an RC oscillator with the sense capacitor and then the oscillator frequency was measured to determine the capacitance.

Figure 2.13 presents a schematic diagram of a low impedance op amp current-to-voltage conversion circuit that is a common interface circuit for detecting the current flowing through a micromachined capacitor [40]. The micromachined capacitor is electrically connected between the drive voltage, $V_c(t)$, and a virtual ground, which prevents the current detection circuitry from loading the micromachined capacitor drive circuit. The current flowing through the capacitor, $I_c(t)$, flows through the amplifier

29

feedback resistor, R_b, and is converted to the amplifier output voltage, $V_o(t)$. For clocked capacitive interface circuit architectures, such as those implemented with switched capacitor circuits, the feedback resistor, R_b, may be replaced with or augmented with a feedback capacitor. This type of amplifier is often referred to as a charge amplifier. For capacitive micromachined structures that possess a differential capacitive architecture, a high impedance interface amplifier is sometimes used, where the center electrode is connected to the high impedance amplifier input. This amplifier circuit is typically used to measure the voltage at the center electrode.
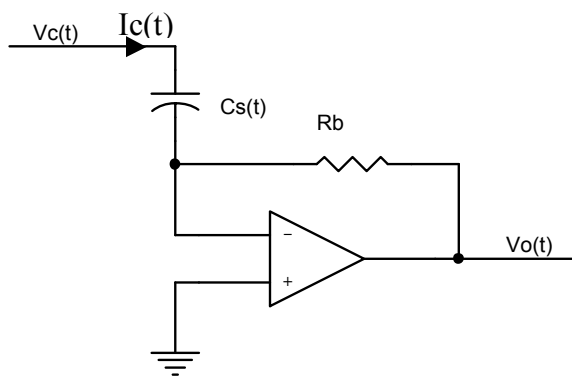
Figure 2.13. A schematic diagram of a current-to-voltage conversion circuit utilized to detect the current flowing through a micromachined capacitor.

Wang [2] suggested a technique for measuring the displacement of a micromachined beam tip that was located between two stationary electrodes that resulted in a differential PPA pair. The technique consisted of superimposing a low voltage, high frequency sinusoidal excitation signal on top of the high voltage, low frequency PPA drive signals. Displacement measurement was accomplished by using the two

differentially configured PPA's as an AC voltage divider for the low voltage, high frequency excitation signal.

Switched capacitor circuits [41] consisting of CMOS switches and subcircuits, and integrated capacitors are particularly useful for detecting the electrode displacement of micromachined capacitive structures, since charge can be placed onto one capacitor and then moved to a second capacitor with the process controlled by digital clocks. Lu et al [42] utilized a switched capacitor interface circuit to measure the displacement of a micromachined z-axis parallel plate accelerometer. The interface circuit measured the capacitance of the micromachined capacitor by placing a known voltage across the capacitor for a set period of time and them transferring the accumulated charge into another capacitor, with a known fixed capacitance, using a charge amplifier. The resulting voltage across the second capacitor was proportional to the capacitance of the micromachined capacitor. The frequency of the clocks used to control the movement of charge through the interface circuit was much higher than the mechanical bandwidth of the micromachined device. The output voltage from this type of interface circuit can be read at the end of the second period and digitized, or it can be low pass filtered if an analog output is desired. Paemel [43] described a switched capacitor interface circuit for an accelerometer with a differential capacitor architecture. The center electrode was connected to a virtual ground. During the first period, one capacitor was connected to a potential of $+V_M$ while the other capacitor was connected to a potential of $-V_M$. During the second period, the difference in the charge accumulated in each capacitor was transferred to a fixed capacitor through the virtual ground. The resulting output voltage

31

across the fixed capacitor was proportional to the difference in capacitance between the two capacitors that comprised the accelerometer.

Synchronous detection is another technique utilized to measure displacement of micromachined capacitive structures. Van Kamen et al [44] used this technique to measure the displacement of the proof mass in an accelerometer with a differential capacitor architecture. The center electrode was connected to a low impedance amplifier circuit through the virtual ground. The other two electrodes were driven with 1MHz antiphase sinusoids with fixed 1V amplitudes. The amplitude of the amplifier output voltage was proportional to the proof mass displacement. This signal was demodulated by multiplying it with a 1MHz squarewave that was obtained from the subcircuit that generated the 1MHz antiphase sinusoids. The output of the multiplier was then low pass filtered to obtain a baseband voltage proportional to the proof mass displacement.

For some applications, it is advantageous to use force feedback to keep a proof mass equally positioned between two electrodes using differentially configured PPA's. For this case, it may be sufficient to just detect the direction that the proof mass has moved away from equilibrium. Kraft et al [45] proposed a modified sigma-delta approach for detecting the direction of displacement of a proof mass between two electrodes in a force balanced accelerometer. A high frequency sinusoid was applied to one of the two electrodes while an antiphase sinusoid was applied to the other electrode. The output signal from the proof mass center electrode was fed into a charge amplifier circuit and the resulting output voltage was then clocked into a sample and hold circuit at the moment the output voltage from the charge amplifier was at its peak. The output from the sample and hold was fed into a comparator circuit to produce a logic "1" or "0."

A "1" indicated that the proof mass was closer to the upper electrode and a "0" indicated that the proof mass was closer to the lower electrode. The logic levels were then used by the control algorithm to move the proof mass back to its equilibrium position. This was accomplished by the controller superimposing a high voltage, fixed magnitude control voltage onto the low voltage, high frequency sinusoid excitation signal going to the outer electrode that was further away from the proof mass. This type of displacement measurement system operated under the assumption that the proof mass only encountered small displacements from the equilibrium point.

2.6 Relative Velocity Measurement in MEMS Devices

Fewer techniques exist for detecting relative velocity in MEMS devices than for detecting relative displacement. Senturia [9] described a technique for directly measuring the relative velocity between two micromachined capacitor electrodes based on measuring the current flowing through the capacitor in response to a voltage applied across it:

$$i_c(t) = C(x)\frac{dV(t)}{dt} + V(t)\frac{\partial C}{\partial x}\frac{dx}{dt}, \qquad (2.47)$$

where x is the electrode displacement coordinate. If V(t) is a constant, V_b, then (2.47) reduces to

$$i_c(t) = V_b \frac{\partial C}{\partial x} \frac{dx}{dt}.$$ (2.48)

The current flowing through the capacitor, $i_c(t)$ is linearly proportional to the velocity of the electrode displacement coordinate if and only if the partial derivative of the capacitance with respect to the electrode displacement coordinate is a constant. Consider the application to an electrostatic tangential actuator where the electrode displacement variable, x(t), is

$$x(t) = x_o + x_A \sin(\omega t)$$ (2.49)

and

$$\dot{x}(t) = x_A \cos(\omega t)$$ (2.50)

Therefore the equation for the capacitance between the two electrodes from (2.19) becomes

$$C(t) = \frac{\varepsilon_o \varepsilon_r b (x_o + x_A \sin(\omega t))}{d_o}$$ (2.51)

and

$$C(x) = \frac{\varepsilon_o \varepsilon_r b x}{d_o}.$$ (2.52)

Taking the partial derivative of C(x) with respect to x yields

$$\frac{\partial C}{\partial x} = \frac{\varepsilon_o \varepsilon_r b}{d_o} = K_{TA} \qquad (2.53)$$

which is a constant. Therefore the current flowing through the capacitor with a constant voltage, V_b, applied across it is

$$i_c(t) = V_b K_{TA} \frac{dx(t)}{dt} = K_{TA} x_A \omega \cos(\omega t), \qquad (2.54)$$

which is proportional to the relative velocity between the two electrodes.

Now consider the application of (2.47) to a PPA while using the same electrode displacement variable, x(t) in (2.49), as was used with the electrostatic tangential actuator. From (2.1), the equation for the capacitance of the parallel plate capacitor becomes

$$C(x) = \frac{\varepsilon_o \varepsilon_r A}{x}. \qquad (2.55)$$

Therefore the partial derivative of C(x) with respect to x is

$$\frac{\partial C(x)}{\partial x} = -\frac{\varepsilon_o \varepsilon_r A x}{x^2} \qquad (2.56)$$

35

which is not a constant since x(t) is a function of time. Therefore the statement that the current flowing through the capacitor is linearly proportional to the velocity of the electrode displacement coordinate is not true for the PPA or for any parallel plate electrodes in motion normal to their opposing faces.

Realizing the difficulty of measuring the relative velocity between two parallel plate electrodes, a number of researchers have developed and utilized strategies to estimate relative velocity between micromachined parallel plate electrodes. Marco et al [1] described a micromachined accelerometer that consisted of two PPA's differentially located on opposing sides of the proof mass. The interface circuit measured the proof mass displacement and generated a voltage that was proportional to the proof mass displacement. A differentiator was then used to determine the direction of proof mass velocity, which was then utilized in a velocity feedback control law to adjust the mechanical Q. Wang [2] described a technique for electrostatically controlling the effects of vibrations on a micromachined beam using two differentially located PPA's with a feedback control law that required relative displacement and velocity measurements. Beam displacement was measured as described in the previous section. Then beam velocity was estimated using the previously measured beam displacement samples. Maithripala et al [3, 4] developed techniques for improving the stable operating range of PPA's using nonlinear controllers and concluded that velocity estimates would be required to achieve significant performance improvement in the transient behavior of lightly damped PPA's. Since, "…this velocity is extremely difficult to sense directly during normal operation of the device," they developed a reduced order nonlinear estimator to estimate the velocity of the movable electrode. Toshiyoshi et al [46] used a

commercially available laser Doppler velocimetry measurement system to analyze the performance of their PPA based MEMS device. However, this type of velocity measurement system is generally limited to laboratory use.

Therefore a number of applications exist that could benefit from a technique for directly measuring the relative velocity between micromachined parallel plate electrodes. In addition to the previously discussed applications that utilized estimated relative velocity in micromachined devices, other applications exist that could benefit from utilizing the measured relative velocity between parallel plate electrodes to augment desired closed loop control laws. Liu et al [8] described several velocity feedback control laws that could be applied to macro- or microsystems for active vibration isolation. Lee and Cho [5], as well as Kampen et al [6], described MEMS devices that utilized PPA's to adjust a gap width in order to tune the level of achieved squeeze-film damping in the device. Nguyen and Howe [7] described a MEMS resonator embedded in a transimpedance amplifier control loop that employed negative or positive feedback to increase or decrease the quality factor of the device. With an integrated relative velocity sensor, more advanced control laws that use either velocity feedback or velocity and position feedback could be integrated into these types of microsystems to improve performance.

2.7 Research Objectives

In this dissertation, the author reexamines the velocity measurement technique presented by Senturia [9] and applies it to MEMS applications where the relative velocity

between two or more microstructures is such that the partial derivative of capacitance with respect to electrode separation distance ($\partial C/\partial x$) is not constant, resulting in nonlinear distortion in the relative velocity measurement. The characteristics of the nonlinear distortion are examined and strategies are proposed for mitigating the effects of the nonlinearities. A prototype relative velocity sensor is developed to evaluate and verify the developed theoretical concepts. The resulting experimental data is then correlated against the developed theoretical model. Therefore the research objectives are (1) apply the relative velocity measurement technique developed by Senturia [9] to applications where $\partial C/\partial x$ is not constant, (2) explore and characterize the nonlinear behavior of the developed relative velocity measurement technique, (3) explore the limitations of the developed relative velocity measurement technique, (4) develop a prototype relative velocity sensor to experimentally verify the relative velocity measurement technique and (5) correlate the experimental data with the developed theoretical model of the relative velocity measurement technique.

CHAPTER 3

THEORETICAL DEVELOPMENT OF THE RELATIVE VELOCITY SENSOR

As previously discussed in Chapter 2, applications have been developed for parallel electrode microstructures that require the measurement or estimation of relative velocity between two or more structures. Examples include accelerometers [1], vibration control in a beam [2], PPA stable operating range enhancement [3, 4], advanced controller design for MEMS devices [5, 6, 7] and active vibration isolation control laws that could be applied to microsystems [8]. In all of these examples where real systems were implemented, the relative velocity term was estimated using either an observer or recorded displacement measurements. Senturia [9] presented a technique for measuring relative velocity between two electrodes that consisted of applying a constant voltage between the two electrodes and measuring the current flowing through the resulting capacitor. As was shown through mathematical derivation in Chapter 2, this technique does produce a current linearly proportional to the relative velocity if the two electrodes are in relative tangential motion. However, if the electrodes are in translational motion normal to their opposing faces, then the resulting current is not linearly proportional to the relative motion of the electrodes. In this Chapter, the technique presented by Senturia [9] will be applied to parallel plate electrodes in translational motion normal to their

opposing faces to develop a relative velocity sensor for parallel plate microstructures experiencing this type of motion.

3.1 Single Electrode Motion

Consider the illustration of the two parallel plate electrodes in Figure 3.1, where one electrode is fixed in position while the other is allowed to move in a direction normal to the face of the fixed electrode [47]. Let the motion of the movable electrode be sinusoidal such that

$$x(t) = x_A \sin(\omega t). \tag{3.1}$$
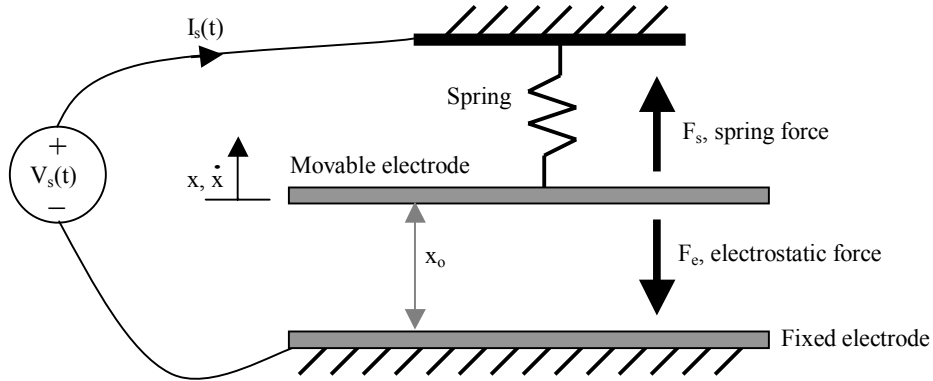
Figure 3.1. An illustration of two parallel plate electrodes.

Taking the first time derivative of (3.1) yields the velocity of the movable electrode with respect to the fixed electrode, such that

$$\dot{x}(t) = x_A \omega \cos(\omega t).$$ (3.2)

Since the relative motion between the two electrodes is sinusoidal, the equation for the capacitance between the two electrodes, $C_s(t)$, from (2.1) is

$$C_s(t) = \frac{\varepsilon_o \varepsilon_r A}{x_o + x_A \sin(\omega t)},$$ (3.3)

where x_o is the rest distance between the two electrodes and x_A is the amplitude of the sinusoidal relative motion between the electrodes, with frequency, ω. As was previously derived in Chapter 2 with (2.56), $\partial C/\partial x$ is not a constant since x is time varying as defined by (3.1).

If a small voltage, $V_s(t)$, which is less than the pull-in voltage, is applied across the two electrodes, then charge, q(t) accumulates in the time varying capacitor, $C_s(t)$, according to the equation

$$q(t) = C_s(t)V_s(t).$$ (3.4)

The current into the capacitor, $C_s(t)$, can be obtained by taking the time derivative of q(t), resulting in

$$I_s(t) = C_s(t)\frac{dV(t)}{dt} + V_s(t)\frac{dC_s(t)}{dt}.$$ (3.5)

41

Suppose that $V_s(t)$ is constrained to be a small, constant DC voltage, V_b. Therefore the current flowing into $C_s(t)$ becomes

$$I_s(t) = V_b \frac{dC_s(t)}{dt} = -\frac{V_b \varepsilon_o \varepsilon_r A x_A \omega \cos(\omega t)}{(x_o + x_A \sin(\omega t))^2}.$$

(3.6)

The negative sign in the numerator indicates that current flows out of the capacitor when the distance between the two electrodes is increasing, which is correct since the capacitance is decreasing. Likewise, when the distance between the electrodes is decreasing, capacitance is increasing, resulting in current flow into the sense capacitor and a positive value for $I_s(t)$.

A convenient interface circuit consists of a low impedance op amp current to voltage conversion circuit, as illustrated in Figure 3.2.
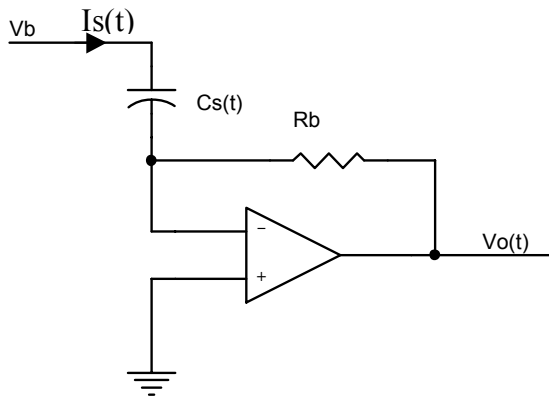
Figure 3.2. A conceptual schematic diagram of the first stage of the sensor interface circuit.

$I_s(t)$, the current flowing into the sensor, $C_s(t)$, flows through the gain resistor R_b to generate $V_o(t)$. Therefore the amplifier gain is equal to $-R_b$. Including $-R_b$ with (3.6), the equation for $V_o(t)$ becomes

$$V_o(t) = -R_b I_s(t) = \frac{R_b V_b \varepsilon_o \varepsilon_r A x_A \omega \cos(\omega t)}{(x_o + x_A \sin(\omega t))^2}. \qquad (3.7)$$

Consider the case where the motion of the movable electrode is small, such that $x_A \ll x_o$. For this case the current flowing into the capacitor can be approximated as

$$V_o(t) \approx \frac{R_b V_b \varepsilon_o \varepsilon_r A x_A \omega \cos(\omega t)}{x_o^2} = K_{2E} x_A \omega \cos(\omega t), \qquad (3.8)$$

where

$$K_{2E} = \frac{R_b V_b \varepsilon_o \varepsilon_r A}{x_o^2}. \qquad (3.9)$$

K_{2E} is the two electrode relative velocity constant. Notice that by comparing (3.8) with (3.2), the output voltage of the interface circuit, $V_o(t)$ is proportional to the relative velocity between the two electrodes. Therefore the capacitor can serve as a sensor for the relative velocity between the two electrodes for small motions, normal to the opposing electrode faces, relative to the rest gap distance.

43

3.2 Two Electrode Motion

Next consider the case where both electrodes are in motion, as illustrated in Figure 3.3.
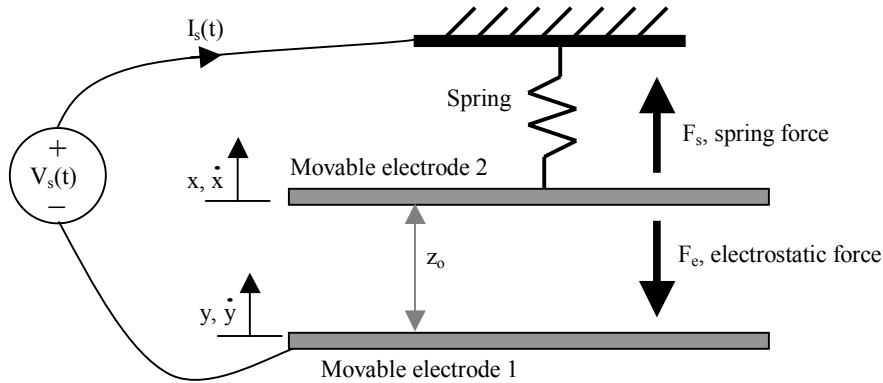
Figure 3.3. An illustration of two parallel plate electrodes with both electrodes in motion.

The motion of the movable electrode 1 is described by

$$y(t) = y_A \sin(\omega t) \qquad (3.10)$$

and

$$\dot{y}(t) = y_A \omega \cos(\omega t), \qquad (3.11)$$

while the motion of the movable electrode 2 is described by

$$x(t) = x_A \sin(\omega t + \theta) \tag{3.12}$$

and

$$\dot{x}(t) = x_A \omega \cos(\omega t + \theta). \tag{3.13}$$

Therefore the relative motion between the two electrodes is described by

$$z(t) = x(t) - y(t) = z_A \sin(\omega t + \phi) \tag{3.14}$$

and

$$\dot{z}(t) = z_A \omega \cos(\omega t + \phi). \tag{3.15}$$

Using (2.1), the equation for $C_s(t)$ becomes

$$C_s(t) = \frac{\varepsilon_o \varepsilon_r A}{z_o + z_A \sin(\omega t + \phi)}. \tag{3.16}$$

Integrating (3.16) into (3.7) with $V_s(t)$ equal to the small, constant voltage V_b yields the current flowing into the capacitor, $I_s(t)$, where

$$I_s(t) = -\frac{V_b \varepsilon_o \varepsilon_r A z_A \omega \cos(\omega t + \phi)}{(z_o + z_A \sin(\omega t + \phi))^2}.$$ (3.17)

The same sensor interface circuit can be used as with the two electrode configuration with one electrode fixed and one in motion, as illustrated in Figure 3.2. The resulting sensor output voltage is then

$$V_o(t) = -R_b I_s(t) = \frac{R_b V_b \varepsilon_o \varepsilon_r A z_A \omega \cos(\omega t + \phi)}{(z_o + z_A \sin(\omega t + \phi))^2}$$ (3.18)

Observe that (3.18) has the same form as (3.7) where x_o and z_o represent the rest distance between the two electrodes and x_A and z_A represent the amplitude of the relative sinusoidal motion between the two electrodes, respectively. Therefore the case of two parallel plate electrodes, where one electrode is fixed while the other is in motion normal to their opposing electrode faces, is a subset of the broader case of two parallel plate electrodes where both electrodes are in motion normal to their opposing electrode faces. For small amplitudes of relative sinusoidal motion such that $z_o \gg z_A$, (3.18) can be approximated by

$$V_o(t) \approx \frac{R_b V_b \varepsilon_o \varepsilon_r A z_A \omega \cos(\omega t + \phi)}{z_o^2} = K_{2Eb} z_A \omega \cos(\omega t + \phi),$$ (3.19)

where

$$K_{2Eb} = \frac{R_b V_b \varepsilon_o \varepsilon_r A}{z_o^2}.$$

(3.20)

Once again, by comparing (3.19) with (3.15), the output voltage from the interface circuit, $V_o(t)$, is proportional to the relative velocity between the two electrodes for $z_o \gg z_A$. Therefore the capacitor serves as a sensor for the relative velocity between the two electrodes for small relative motions, normal to the opposing electrode faces, of the electrodes relative to the rest gap distance.

3.3 Three Electrode Differential Motion

Consider the case where a movable electrode with a potential $V_s(t)$ is centered directly between two fixed electrodes, each at 0V, as illustrated in Figure 3.4. If an external force, $F_{ex}(t)$, is applied to the movable electrode, the movable electrode will experience a motion described by $x(t)$, such that the distance between the top fixed electrode and the movable electrode equals $x_o - x(t)$ while the distance between the bottom fixed electrode and the movable electrode equals $x_o + x(t)$.
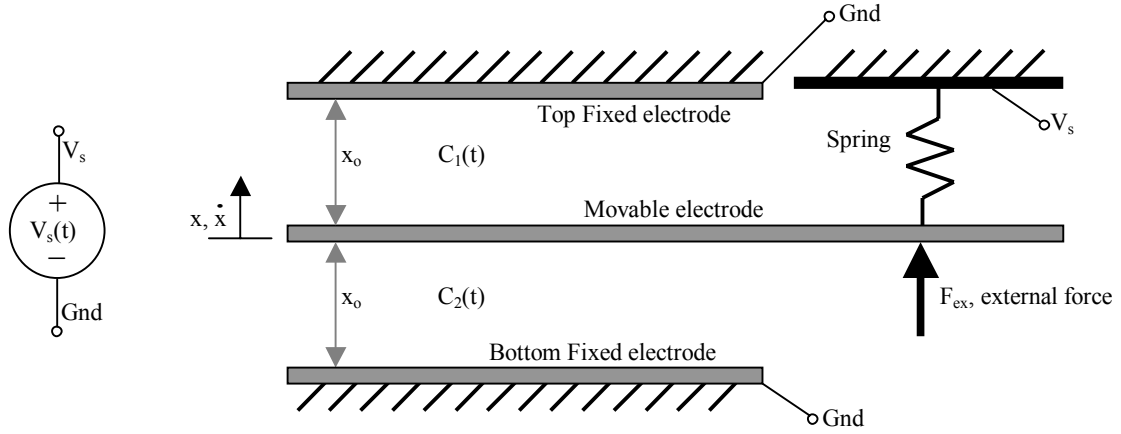
Figure 3.4. An illustration of a three electrode configuration with differential motion.

Therefore the time varying capacitance between the movable electrode and the top fixed electrode, $C_1(t)$, is modeled by

$$C_1(t) = \frac{\varepsilon_o \varepsilon_r A}{x_o - x_A \sin(\omega t)},$$ (3.21)

while the time varying capacitance between the movable electrode and the bottom fixed electrode, $C_2(t)$, is modeled by

$$C_2(t) = \frac{\varepsilon_o \varepsilon_r A}{x_o + x_A \sin(\omega t)}.$$ (3.22)

If $V_s(t)$ is constrained to be a small, constant DC voltage, V_b, then the current flowing into each capacitor can be calculated as

$$I_1(t) = V_b \frac{dC_1(t)}{dt} = \frac{V_b \varepsilon_o \varepsilon_r A x_A \omega \cos(\omega t)}{(x_o - x_A \sin(\omega t))^2} \qquad (3.23)$$

and

$$I_2(t) = V_b \frac{dC_2(t)}{dt} = -\frac{V_b \varepsilon_o \varepsilon_r A x_A \omega \cos(\omega t)}{(x_o + x_A \sin(\omega t))^2}. \qquad (3.24)$$

Consider the sensor interface circuit illustrated in Figure 3.5, consisting of two equal, low impedance, transimpedance amplifiers that convert the currents flowing into each capacitor into the voltages $V_1(t)$ and $V_2(t)$, each with a gain of R_b.
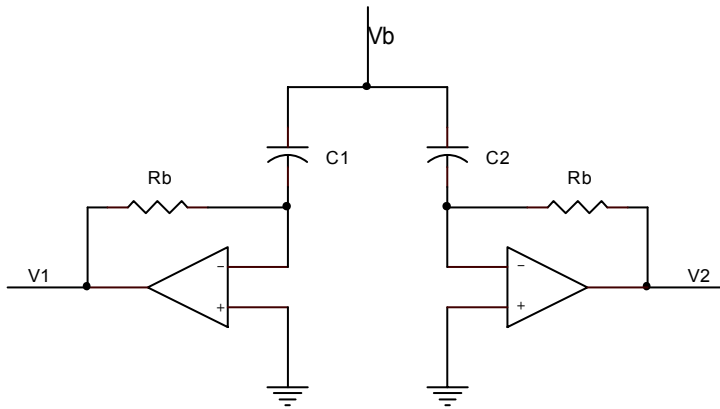
Figure 3.5.   An illustration of the sensor interface circuit for the three electrode differential relative velocity sensor.

Therefore the equations for $V_1(t)$ and $V_2(t)$ are

$$V_1(t) = -R_b I_1(t) = -\frac{R_b V_b \varepsilon_o \varepsilon_r A x_A \omega \cos(\omega t)}{(x_o - x_A \sin(\omega t))^2} \qquad (3.25)$$

and

$$V_2(t) = -R_b I_2(t) = \frac{R_b V_b \varepsilon_o \varepsilon_r A x_A \omega \cos(\omega t)}{(x_o + x_A \sin(\omega t))^2} . \qquad (3.26)$$

A sensor output voltage, $V_o(t)$ can be defined as

$$V_o(t) = V_2(t) - V_1(t), \qquad (3.27)$$

Therefore

$$V_o(t) = R_b V_b \varepsilon_o \varepsilon_r A x_A \omega \cos(\omega t) [\frac{1}{(x_o - x_A \sin(\omega t))^2} + \frac{1}{(x_o + x_A \sin(\omega t))^2}], \qquad (3.28)$$

which can be rewritten as

$$V_o(t) = R_b V_b \varepsilon_o \varepsilon_r A x_A \omega \cos(\omega t) [\frac{(x_o - x_A \sin(\omega t))^2 + (x_o + x_A \sin(\omega t))^2}{(x_o - x_A \sin(\omega t))^2 (x_o + x_A \sin(\omega t))^2}]. \qquad (3.29)$$

50

The following algebraic identities can be used to simplify (3.29)

$$(x+a)^2 = x^2 + 2xa + a^2,$$ (3.30)

$$(x-a)^2 = x^2 - 2xa + a^2,$$ (3.31)

$$(x+a)^2 + (x-a)^2 = 2x^2 + 2a^2,$$ (3.32)

and

$$(x+a)^2(x-a)^2 = x^4 - 2a^2x^2 + a^4.$$ (3.33)

Since (3.29) has the following form

$$\frac{(x-a)^2 + (x+a)^2}{(x-a)^2(x+a)^2} = \frac{2x^2 + 2a^2}{x^4 - 2a^2x^2 + a^4},$$ (3.34)

(3.29) can be rearranged to yield

$$V_o(t) = R_b V_b \varepsilon_o \varepsilon_r Ax_A \omega \cos(\omega t)[\frac{2x_o^2 + 2(x_A \sin(\omega t))^2}{x_o^4 - 2(x_A \sin(\omega t))^2 x_o^2 + (x_A \sin(\omega t))^4}].$$ (3.35)

For the case where $x_o \gg x_A$, (3.35) can be approximated by

51

$$V_o(t) = \frac{2R_bV_b\varepsilon_o\varepsilon_r Ax_A\omega\cos(\omega t)}{x_o^2} = K_D x_A\omega\cos(\omega t) \tag{3.36}$$

where

$$K_D = \frac{2R_bV_b\varepsilon_o\varepsilon_r A}{x_o^2}. \tag{3.37}$$

Notice that for the differential three electrode configuration, the proportionality constant, K_D, is twice the magnitude of the proportionality constant for the two electrode configuration, K_{2E}.

3.4 Characterization

For the two electrode relative velocity sensor, consider a normalized version of the equation for the output voltage of the velocity sensor interface circuit from (3.7), where ωt has been replaced with ϕ such that

$$V_o(t) = \frac{Kx_A\cos(\phi)}{(x_o + x_A\sin(\phi))^2}, \tag{3.38}$$

where

$$K = \frac{x_o^2}{x_A} \tag{3.39}$$

and

$$x_o = 10 \mu m.$$ (3.40)

Equation (3.38) can be used to investigate the nonlinear effects in the sensor performance due to the $x_A\sin(\phi)$ term in the denominator. Figure 3.6 presents a graph of the normalized sensor response from (3.38) for $0 < \phi < 2\pi$, compared to the response of an ideal or perfect relative velocity sensor (referred to in Figure 3.6 as "normalized velocity"), for various ratios of x_o to x_A. Observe that the sensor response quickly deviates from the desired response as the ratio of x_o/x_A falls below 100. However, notice that the points where the velocity changes direction do not deviate from the desired sensor response as the ratio of x_o/x_A varies. This indicates that the two electrode relative velocity sensor serves best as a relative velocity direction sensor, where the polarity of the output voltage from the sensor interface circuit or the direction of the current flowing into or out of the sense capacitor indicates the direction of relative velocity between the two electrodes. Also observe that the distortion is much greater during the second half of the relative velocity cycle than during the first half. This phenomenon occurs because of two characteristics related to the system dynamics. The first characteristic is the nonlinear relationship between capacitance and the distance between the two electrodes. The second characteristic is that the electrodes are closer to each other during the second half of the velocity cycle than during the first half, because the relative velocity leads the relative displacement by 90° for a sinusoidal relative displacement. In addition to the distortion that corrupts the relative velocity measurements for small ratios of x_o/x_A, the

53

sensor output voltage will spike negative and then positive during the second half of the velocity cycle. Therefore if the sensor is utilized to detect the direction of relative velocity for small ratios of x_o/x_A, the sensor interface circuit will have to be designed to handle the resulting voltage spikes in order to avoid amplifier saturation, which will further distort the signal and possibly corrupt the otherwise accurate information about when the relative velocity changes direction.

Normalized Sensor Response as a Function of x_o/x_A

Vo(t), V vs Phi, radians

Legend:
- normalized velocity
- sensor (xo/xa = 100)
- sensor (xo/xa = 10)
- sensor (xo/xa = 5)
- sensor (xo/xa = 3.33)
- sensor (xo/xa = 2.5)
- sensor (xo/xa = 2.0)
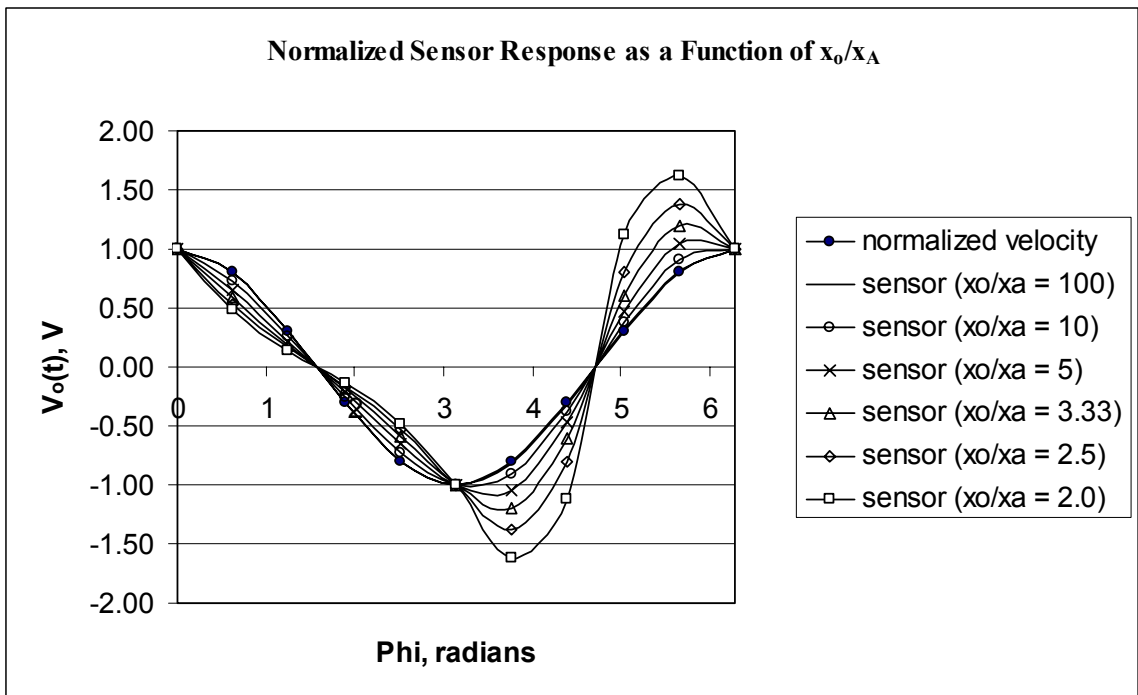
Figure 3.6. A graph of the performance of the normalized two electrode relative velocity sensor for various ratios of x_o/x_A.

Another measure of the performance of the two electrode relative velocity sensor is the total harmonic distortion (THD) of the normalized sensor response as the ratio of x_o to x_A varies. The THD was calculated using a MATLAB™ routine, and an example

54

M-file for the THD calculation is presented in Appendix A. The algorithm began with the computation of a 1024 point FFT, p(i), on 1024 samples of $V_o(\phi)$ from (3.38) for $0 < \phi < 2\pi$. P(1) was the DC term and was not utilized in the THD calculation. P(2) was the fundamental frequency term and P(3) through P(512) were the higher harmonic terms. The THD was calculated by dividing the square root of the sum of the squares of the higher harmonic terms by the fundamental frequency term. A table of the calculated THD values for various x_o/x_A ratios is presented in Table 3.1. Observe that the THD can be approximated by x_A/x_o for x_o/x_A ratios greater than 1.5. As would be expected from

x_o/x_A	THD	x_A/x_o
100	0.0100	0.0100
10	0.1005	0.1000
5	0.2044	0.2000
3.33	0.3158	0.3003
2.5	0.4390	0.4000
2	0.5833	0.5000
1.5	0.9161	0.6667
1.1	2.4370	0.9091

Table 3.1. The total harmonic distortion values for the normalized two electrode relative velocity sensor response for various ratios of x_o/x_A.

the data in Figure 3.6, the THD increases rapidly as the ratio of x_o to x_A falls below 100.
For a purely sinusoidal relative velocity input to the sensor, the nonlinearity results in
higher frequency harmonics being present in the sensor output voltage. To illustrate this,
a 1024 point FFT was performed on the ideal normalized sensor response and on the
normalized sensor responses for x_o/x_A equal to 5 and x_o/x_A equal to 25, where the 1024
input data points were taken over exactly ten cycles of a 1KHz sinusoid with a 1V

Figure 3.7. A comparison of the FFT spectral responses of the ideal normalized two
electrode relative velocity sensor with normalized two electrode relative velocity sensors
of $x_o/x_A = 5$ and $x_o/x_A = 25$.

56

amplitude. The graph in Figure 3.7 presents the FFT spectral responses from 0Hz to 10KHz. The ideal sensor and both modeled sensors had approximately the same amount of energy in the fundamental component at 1KHz. Both modeled sensors had considerable energy in higher harmonics, at 2KHz, 3KHz, 4KHz, etc…, all 1KHz apart, which resulted from the nonlinear characteristics of the sensor. However, the amount of energy present in the higher harmonics increased as the ratio of x_o/x_A decreased.

For the three electrode relative velocity sensor with differential motion, consider a normalized version of the equation for the velocity sensor output voltage from (3.35), such that

$$V_o(t) = Kx_A \cos(\phi)[\frac{2x_o^2 + 2(x_A \sin(\phi))^2}{x_o^4 - 2(x_A \sin(\phi))^2 x_o^2 + (x_A \sin(\phi))^4}], \qquad (3.41)$$

where

$$K = \frac{x_o^2}{2x_A} \qquad (3.42)$$

and

$$x_o = 10\mu m . \qquad (3.43)$$

Equation (3.41) can be used to investigate the effects of the nonlinearities in the differential electrode sensor model. Figure 3.8 presents a graph of the normalized sensor response from (3.41) for $0 < \phi < 2\pi$, compared to the ideal response of the sensor (referred to in Figure 3.8 as "normalized velocity"), for various ratios of x_o/x_A. Observe
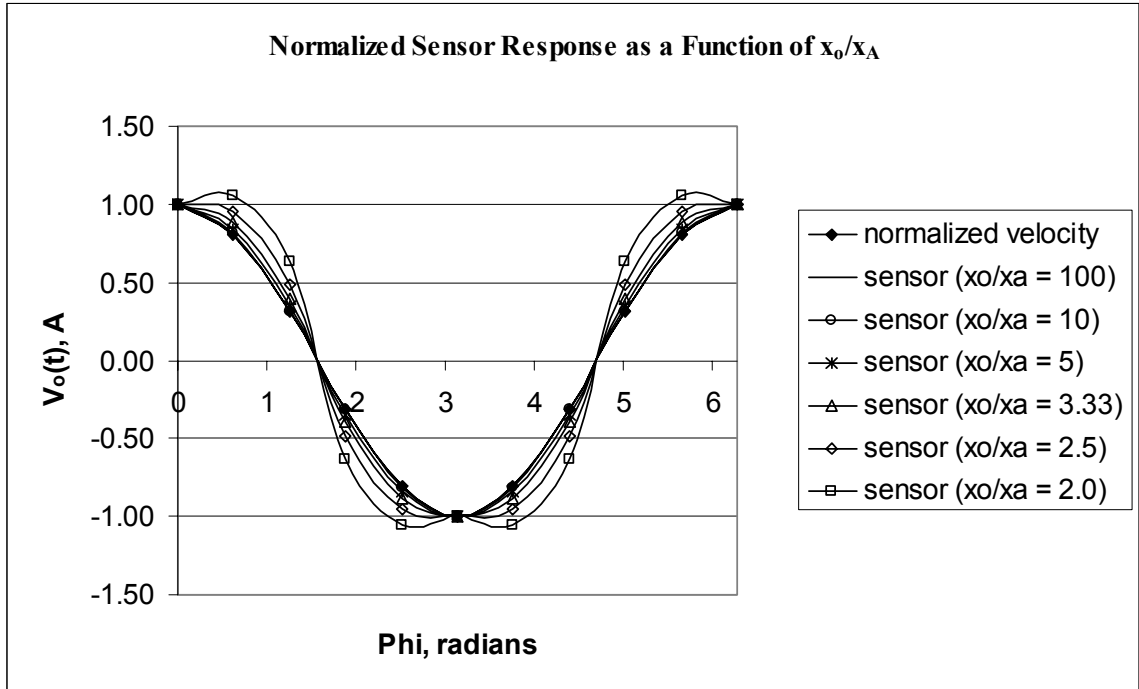
Figure 3.8. A graph of the performance of the normalized three electrode differential relative velocity sensor for various ratios of x_o/x_A.

that although the sensor response deviates from the desired response as the ratio of x_o/x_A falls below 100, the amount of deviation is less than in the two electrode velocity sensor response for the same ratio of x_o/x_A. Additionally, the sensor response is symmetric over the entire cycle of motion. As with the two electrode relative velocity sensor, the points where the velocity changes direction do not deviate from the desired sensor response as

58

the ratio of x_o/x_A varies. Therefore as with the two electrode relative velocity sensor, the three electrode differential relative velocity sensor appears to function best as a velocity direction sensor.

The THD was calculated for the normalized three electrode differential relative velocity sensor response using the same algorithm as was used to compute the THD for the two electrode relative velocity sensor. The calculated THD values are presented in Table 3.2. Similar to the two electrode configuration, the THD for the three electrode configuration can be approximated by $(x_A/x_o)^2$ for ratios of x_o/x_A equal to or greater than 1.5. A 1024 point FFT was also performed on the ideal normalized three electrode

x_o/x_A	THD	$(x_A/x_o)^2$
100	7.479×10^{-5}	1×10^{-4}
10	7.538×10^{-3}	0.0100
5	0.0306	0.0400
3.33	0.0709	0.0902
2.5	0.1310	0.1600
2	0.2169	0.2500
1.5	0.4510	0.4444
1.1	1.6043	0.8264

Table 3.2. The total harmonic distortion values for the normalized three electrode differential relative sensor response for various ratios of x_o/x_A.

differential relative velocity sensor response and on the normalized sensor responses for x_o/x_A equal to 5 and x_o/x_A equal to 25, where the 1024 input data points were taken over exactl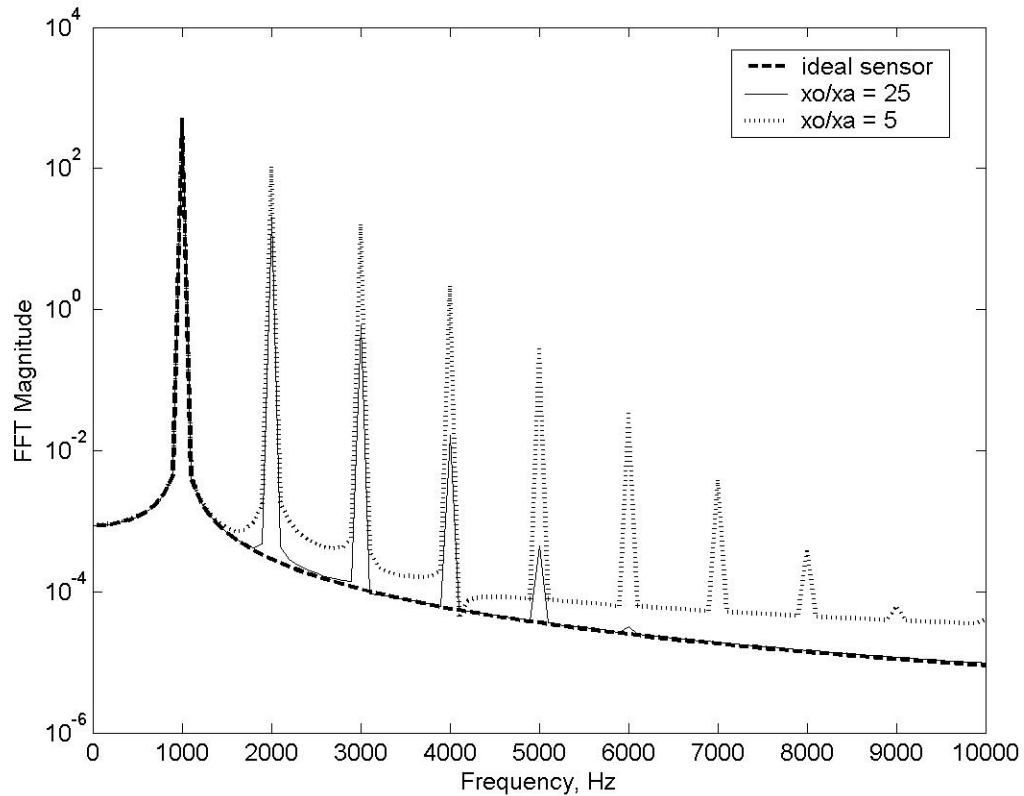y ten cycles of a 1KHz sinusoid with a 1V amplitude. The graph in Figure 3.9 presents the FFT spectral responses from 0Hz to 10KHz. The ideal sensor and both modeled sensors had approximately the same amount of energy in the fundamental
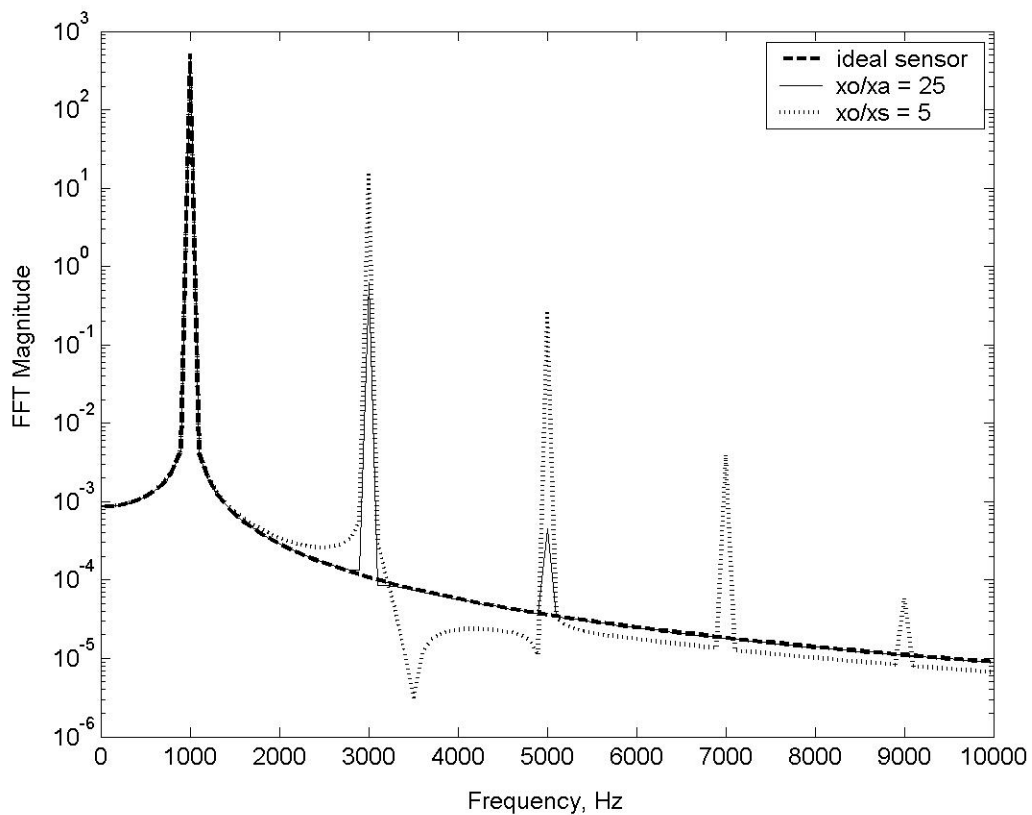
Figure 3.9. A comparison of the FFT spectral responses of the ideal normalized three electrode differential relative velocity sensor with normalized three electrode differential relative velocity sensors of $x_o/x_A = 5$ and $x_o/x_A = 25$.

component at 1KHz. Both modeled sensors had considerable energy in higher

harmonics, at 3KHz, 5KHz, 7KHz, etc..., all 2KHz apart, which resulted from the

nonlinear characteristics of the sensor. The amount of energy present in the higher

harmonics increased as the ratio of x_o to x_A decreased.

Figure 3.10 presents a plot of the THD versus the x_o/x_A ratios for both the two

electrode and the three electrode relative velocity sensors. The THD for both sensors

grows rapidly as the x_o/x_A ratio decreases toward one. However, the THD of the three

electrode differential relative velocity sensor is much lower than the THD of the two

electrode relative velocity sensor as the x_o/x_A ratio increases greatly from one. Therefore
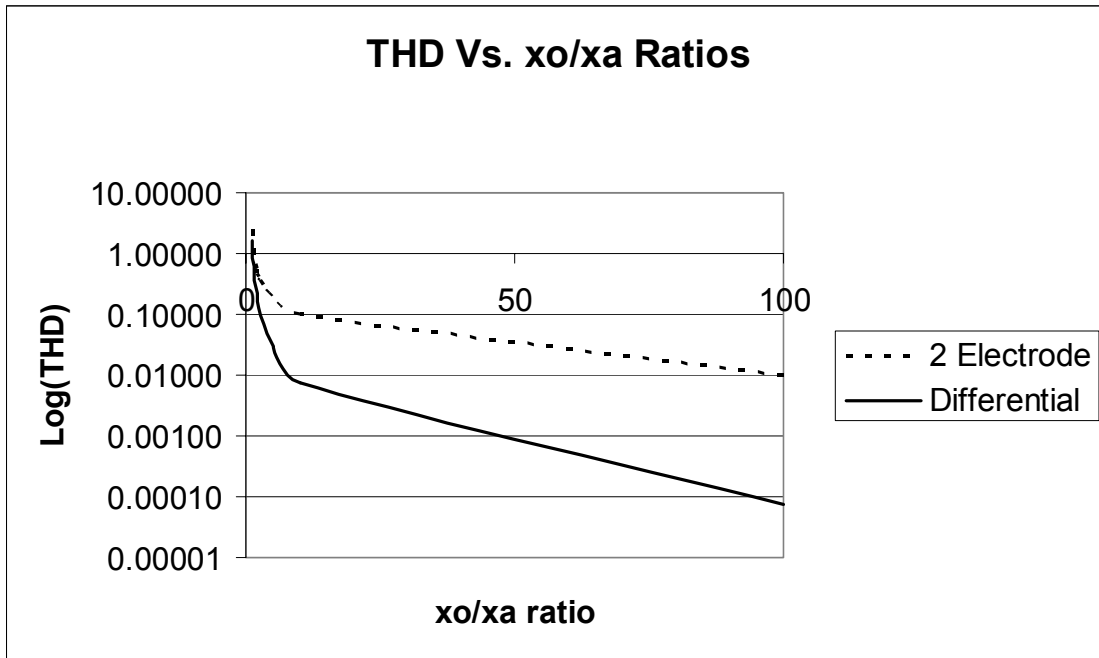
Figure 3.10. A plot of the THD versus x_o/x_A ratios for both the two electrode and the

three electrode relative velocity sensors.

the three electrode differential relative velocity sensor is a more precise relative velocity sensor if actual relative velocity measurements are required. Both sensors equally detect the direction of relative velocity, as long as the high voltage spikes associated with the points of highest distortion, which occur during the second half of each relative velocity cycle in the two electrode sensor and equally in both cycles in the three electrode differential sensor, can be properly handling in the sensor interface circuit. The THD estimate can be used to determine the minimum x_o/x_A ratio that can be tolerated for a particular application to maintain a minimum level of quality in the relative velocity measurement.

CHAPTER 4

DEVELOPMENT OF THE RELATIVE VELOCITY SENSOR PROTOTYPE

In order to verify the theoretical investigation into a relative velocity sensor for measuring relative velocity between two parallel electrodes with motion normal to the electrode opposing faces, a prototype relative velocity sensor was developed. This chapter presents the background, development and assembly of the prototype sensor.

4.1 Background

The prototype relative velocity sensor was developed in conjunction with the development of a micromachined passive vibration isolation platform for the MBARS MEMS gyroscopic sensor, a comb drive actuated resonating gyroscope architecture [32]. The MBARS device resonated at approximately 3KHz. Some potential applications, such as small missiles, generate environmental vibrations with components that exceed 3KHz [48]. If the MBARS gyroscopic sensor were utilized in these applications, external vibrations close to the device resonating frequency could potentially couple into the sensor and corrupt its performance or possibly even damage the sensor. Therefore Auburn University worked with Morgan Research Corporation to develop a

micromachined passive vibration isolation platform to significantly attenuate external vibrations close to the MBARS resonating frequency. The vibration isolation platform was designed to be integrated into the packaging of the MBARS sensor die and functioned as a mechanical low pass filter. Figure 4.1 presents an illustration of the passive micromachined mechanical filter prototype. The filter structure consisted of a center proof mass pad onto which the gyro was attached, eight springs that attached the proof mass pad to a surrounding frame, and the surrounding frame.
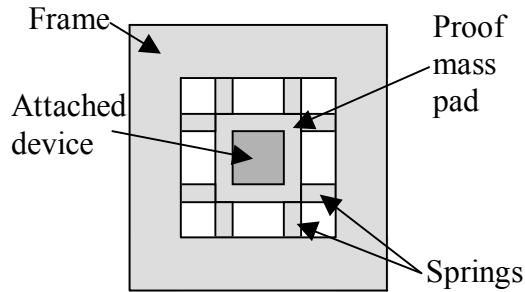
Figure 4.1. An illustration of the prototype micromachined passive filter chip.

The filter chip was fabricated from an n-type (100) silicon wafer using bulk micromachining techniques, primarily deep reactive ion etching (DRIE). The frame and proof mass pad had the same height, approximately 375μm. The spring design and layout were selected to minimize rotational motion about the out-of-plane or z-axis. For small deflections in the z-axis, the system spring constant, K_s, can be approximated by

$$K_s = \frac{8wt^3}{l^3},$$

(4.1)

where E is the Young's modulus of silicon, w is the width of the springs, t is the thickness of the springs and l is the length of the springs.   The prototype filter had a frame that was 19.6mm long, 3.5mm across and approximately 375µm thick. The proof mass pad was 10mm by 10mm and approximately 375µm thick, and was designed to support an attached die that was 5mm by 5mm and 560µm thick. Each of the eight springs was 1300µm long and 225µm wide. To obtain a filter natural frequency of 900Hz, the spring thickness should be approximately 30µm.   However, since there can be significant variability in the spring thickness due to the etching rate, varying the thickness from 20µm to 40µm results in a natural frequency range of 490Hz to 1390Hz for the device. The equation for the filter natural frequency is

$$\omega_n = \sqrt{\frac{K_s}{M_s}},$$

(4.2)

where K_s is the system spring constant and M_s is the mass of the proof mass pad and the attached MBARS gyroscope die.

The FEA based MEMS CAD tool IntelliSuite™ was used to simulate the micromachined filter structure with the MBARS die attached. The nominal dimensions of the Si MBARS die were 5000µm wide by 5000µm long by 560µm thick.   The MBARS die was modeled as a solid block centered on top of the filter proof mass pad for the FEA analysis. Silicon was modeled with a Young's modulus value of 176GPA and a density of 2.35 g/cm^3 for the FEA analysis. Figure 4.2 presents the IntelliSuite™ FEA solid model of the filter structure with the attached MBARS die.
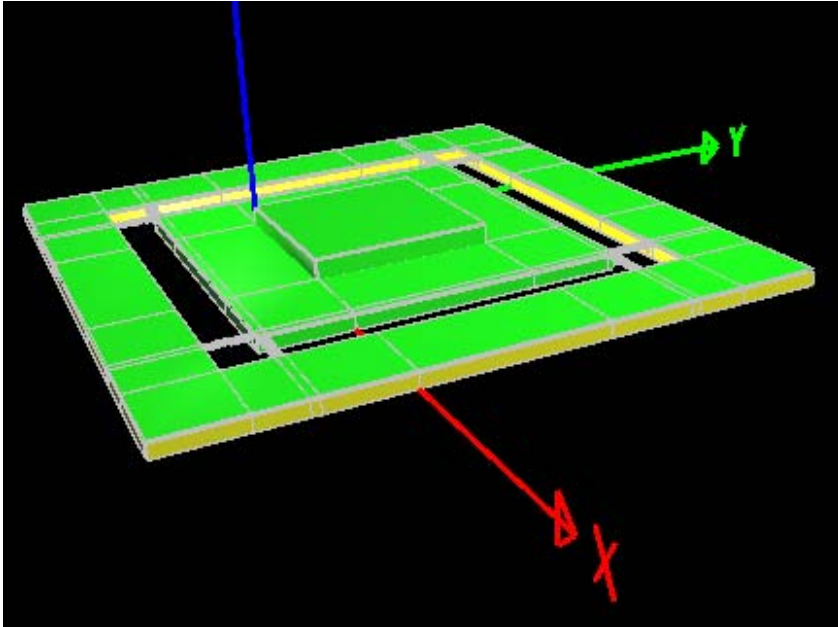
Figure 4.2. The FEA model of the filter structure with the attached MBARS sensor die.

The first five vibration modes were simulated using IntelliSuite™, and had the following resonant frequencies, mode 1: 901.992Hz, mode 2: 1832.66Hz, mode 3: 1832.66Hz, mode 4: 25,528.7Hz and mode 5: 25,528.7Hz.   Mode 1 is the z-axis translational mode and is the primary mode of interest for this application.   The exaggerated mode 1 response, as modeled in IntelliSuite™, is presented in Figure 4.3. Illustrations of the exaggerated responses of the first 4 higher order modes from the IntelliSuite™ simulation, mode 2 through mode 5, are presented in Figures 4.4 through 4.7.
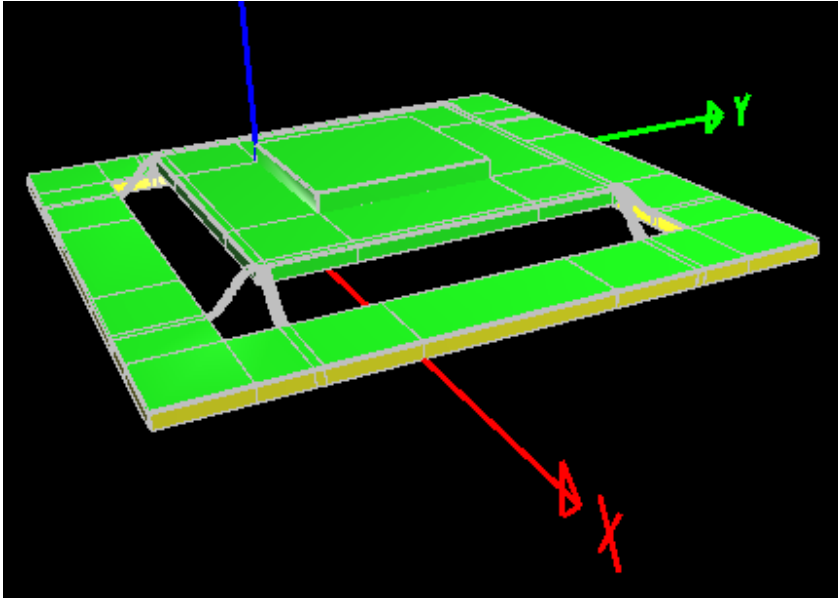
Figure 4.3. The results from an FEA simulation illustrating the exaggerated mode 1 z-axis translational response of the passive filter structure.
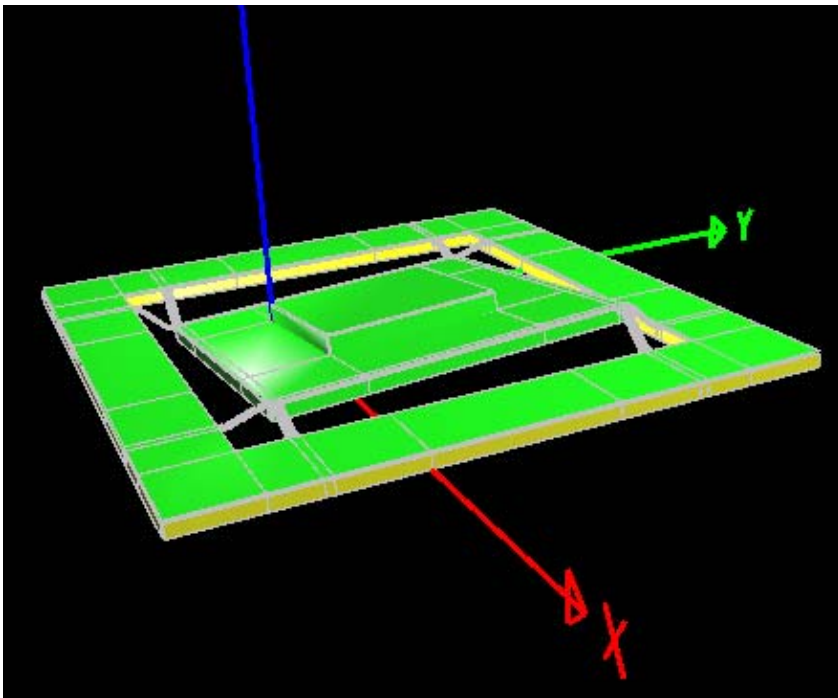
Figure 4.4. The results from an FEA simulation illustrating the exaggerated mode 2 response.
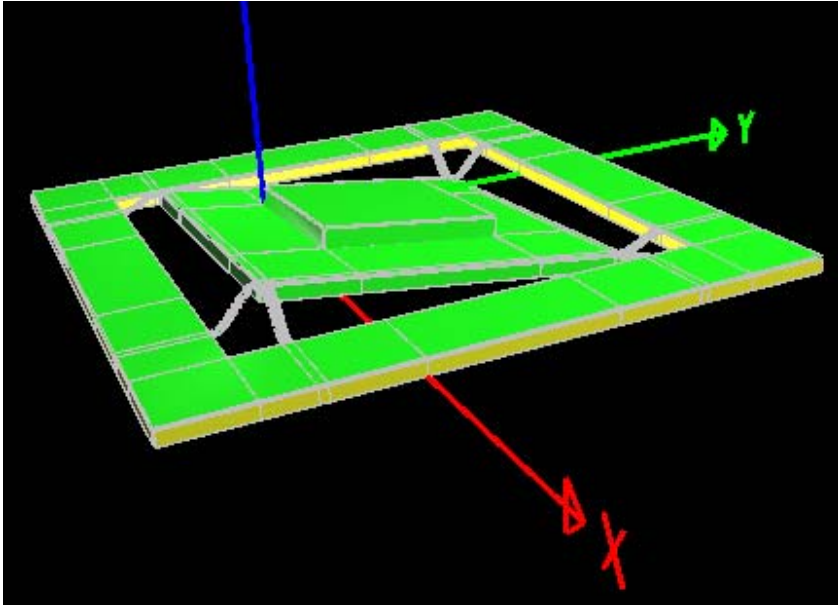
Figure 4.5. The results from an FEA simulation illustrating the exaggerated mode 3 response.
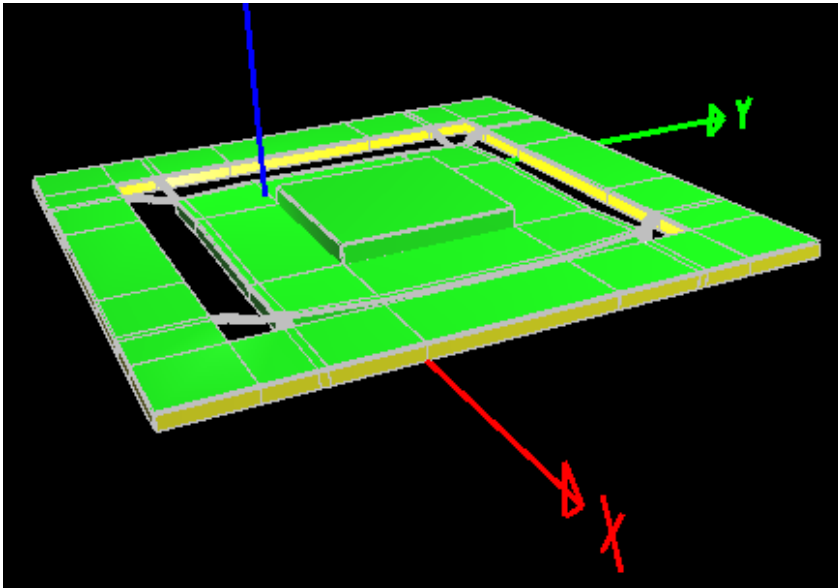
Figure 4.6. The results from an FEA simulation illustrating the exaggerated mode 4 response.
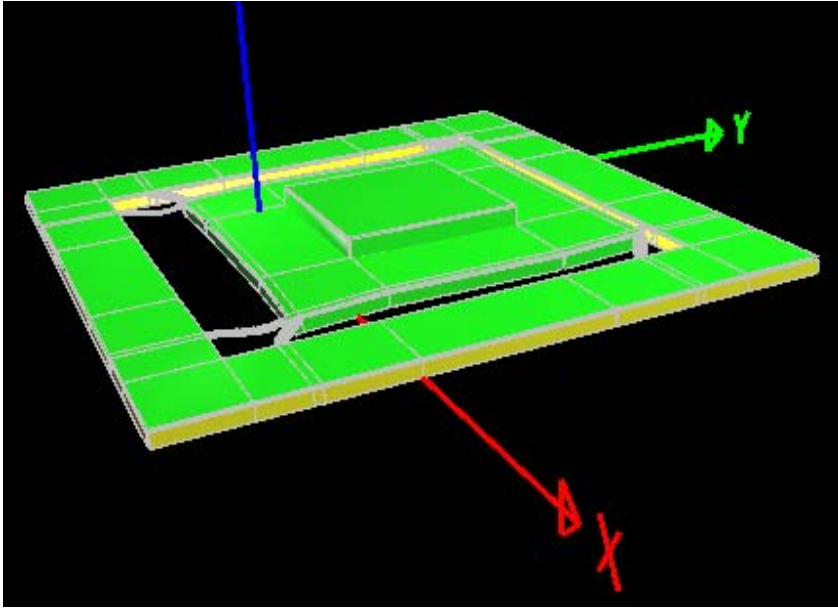
Figure 4.7. The results from an FEA simulation illustrating the exaggerated mode 5 response.

Utilizing (4.1) and (4.2), the estimated mode 1 natural frequency was calculated to be 902.698Hz for a 30μm spring thickness. The IntelliSuite™ FEA simulation calculated a mode 1 natural frequency of 901.992Hz, which is within 0.08% of the value calculated using (4.1) and (4.2).

Electrical traces were fabricated on top of the filter spring structures to connect wirebond pads on the frame to wirebond pads on the proof mass pad. This was accomplished by electron beam depositing titanium and gold layers onto a silicon dioxide layer on top of the springs, and then patterning the traces prior to the DRIE fabrication of the springs. After fabrication of the filter chip, the MBARS device was attached to the center of the filter proof mass pad with silver filled conductive die attach adhesive. Then the MBARS device was wirebonded to the wirebond pads on the proof mass pad. The

wirebond pads on the filter frame were designed to provide electrical connection to the package. Each of the filter's eight springs had two electrical traces on its top surface that electrically connected wirebond pads on the proof mass pad with wirebond pads on the frame. Although sixteen wirebond pads were available, the MBARS die only required ten wirebonds for operation. Figure 4.8 presents a photograph of an MBARS gyroscopic sensor attached and wirebonded to a micromachined vibration isolation filter.

Figure 4.9 presents the measured mechanical frequency response from dynamic testing of a prototype passive filter, similar to the one shown in Figure 4.8, except that a silicon test die replaced the MBARS MEMS gyro on the filter proof mass pad. Dynamic testing was accomplished using an electromechanical shaker with a laser displacement measurement system. The silicon test die had a reflective surface more suitable for laser displacement measurement of the filter dynamic characteristics. The primary resonant peak occurred at 885Hz. An underdamped response with a mechanical quality factor of approximately 20 is evident in the plot of the recorded test data.

The uncontrolled underdamped response of the passive filter can potentially result in excessive proof mass pad z-axis motion where the proof mass pad comes into contact with the package beneath it if the device is excited by external vibrations at the filter resonant frequency. Velocity feedback using a PPA, where the electrodes are the backside of the filter proof mass pad and the package beneath the proof mass pad, can be used to control the filter mechanical quality factor by adjusting it to an acceptable level, resulting in the realization of an active vibration isolation filter. Figure 4.10 illustrates the integration of a PPA with the passive filter structure.
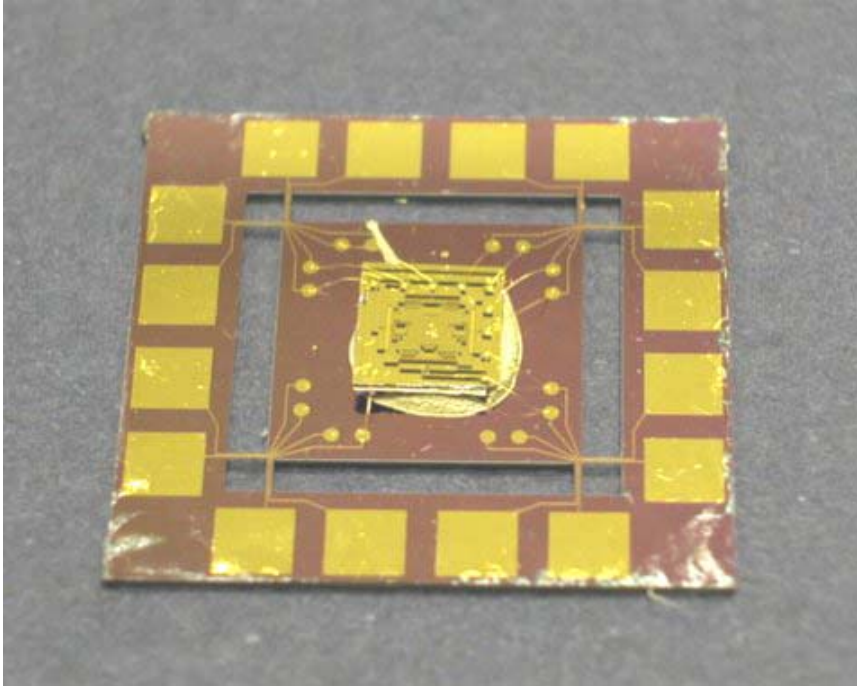
Figure 4.8. A photograph of an MBARS gyroscopic sensor die attached to a passive filter die.
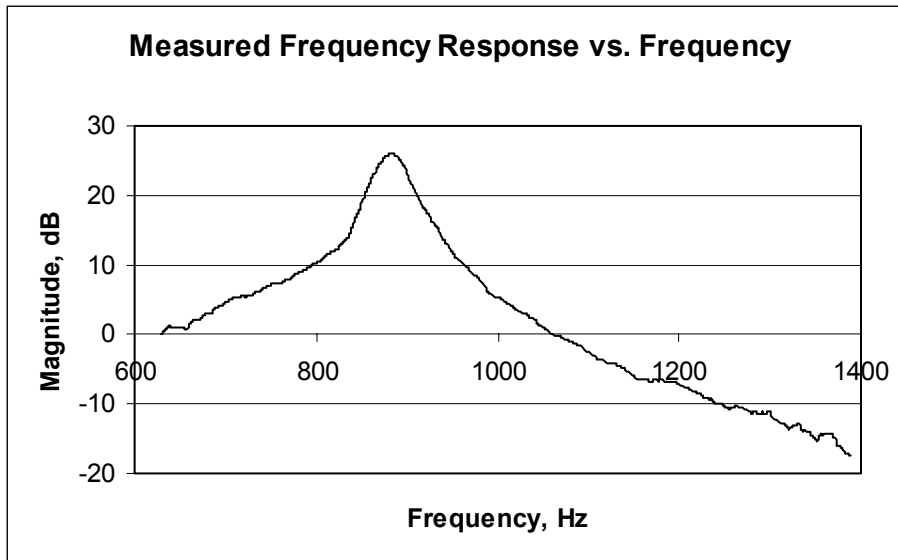
Figure 4.9. The measured mechanical frequency response from dynamic testing of a passive filter prototype.
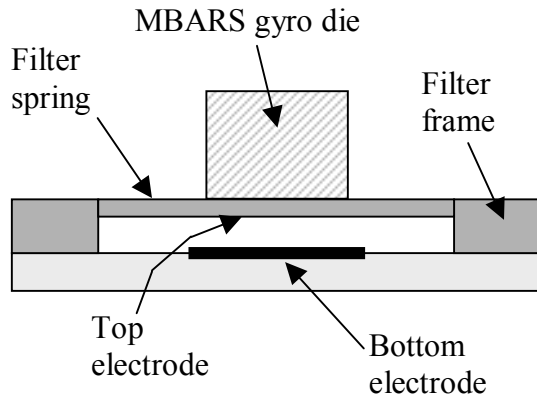
Figure 4.10 An illustration of a PPA implemented between the filter proof mass pad and the package beneath it.

Suppose that relative velocity measurement could be obtained by utilizing part of the electrode area for velocity detection while the remaining electrode area is used to implement the PPA. Then velocity feedback could by employed to adjust the damping of the mechanical filter. This is illustrated in Figure 4.11, where the top electrode is common to both the PPA and the relative velocity sensor. The bottom electrode has been segmented into two electrodes, a small circular center electrode and a larger annular ring outer electrode. The smaller circular center electrode is used to measure the relative velocity between the proof mass pad and the frame, while the larger annular ring outer electrode is used to realize the PPA with the proof mass pad electrode. The control algorithm and associated electronics are not illustrated in Figure 4.11.
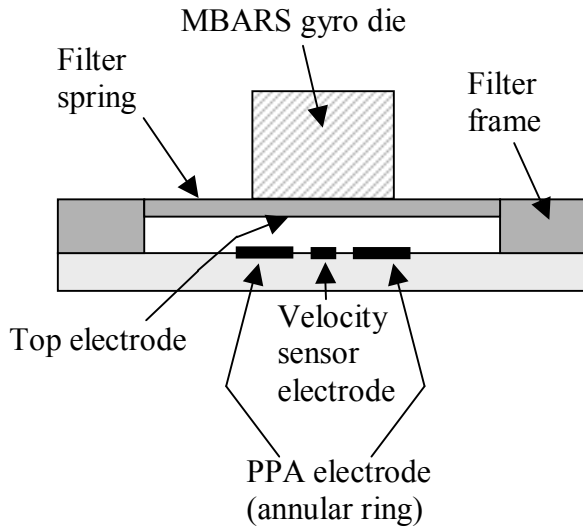
Figure 4.11 An illustration of the integration of a PPA and a relative velocity sensor with the passive filter structure.

4.2 Fabrication of the Micromachined Device

A prototype of the relative velocity sensor was developed to validate the model for the two electrode relative velocity sensor presented in Chapter 3 based on the illustration in Figure 4.11 with the PPA electrode unused. The prototype consisted of a micromachined silicon planar spring-mass-damper platform that was suspended over a second planar electrode.   The design for the micromachined spring-mass-damper platform was based on the design for the passive filter structure developed for isolating the MBARS MEMS gyroscope from high frequency vibrations present in its anticipated operating environment, a photograph of which was presented in Figure 4.8.   It consisted of a square proof mass pad attached to a surrounding frame by eight springs. The bottom side of the proof mass pad formed the upper or movable electrode.   The passive filter

structure was mounted onto the back side of a double layer printed circuit board directly over a planar electrode using a nonconductive spacer, which set the rest distance between the two electrodes. The relative velocity sensor interface electronics were integrated onto the front side of the printed circuit board.

A nominally 375µm thick, 100mm diameter, n-type (100) silicon double-side polished wafer with a resistivity of 1-10Ωcm was utilized to fabricate the spring-mass-damper platform. The layout was identical to the layout of the passive filter device in Figure 4.8, and consisted of a square center proof mass pad connected to a square surrounding frame by eight springs. The frame and proof mass pad had a nominal thickness of 375µm, the thickness of the silicon wafer. The spring thickness was set during microfabrication by the length of time the wafer was etched. The surrounding frame was 19.6mm long and 3.5mm across, and the center square proof mass pad was 10mm across. Each of the eight springs was 1300µm long and 225µm wide. A bare silicon die, nominally 5mm by 5mm by 560µm thick, was attached to the proof mass pad using cyanoacrylate glue in order to increase the mass of the proof mass so that a reasonable mechanical natural frequency could be obtained with springs that were thick enough to survive handling. For the prototype, a reasonable natural frequency was one that allowed the resulting system to be evaluated with available test equipment. 40µm was selected as the designed spring thickness, which resulted in a designed mechanical natural frequency of 1.39KHz. A lower natural frequency would have required thinner springs or a heavier proof mass, while a higher natural frequency would have increased the operating requirements of the sensor interface circuitry and the data collection instrumentation, since it was desirable to collect information on higher harmonics

74

produced by the nonlinear distortion inherent in the parallel electrode velocity sensor architecture.

Two photolithographic masks were required to fabricate the micromachined silicon devices. Since the devices had relatively large features, the masks were laid out using the CAD tool ViewMaster 8.4.50 and were implemented on high resolution laser photoplots with a 10,000 dots-per-inch (DPI) resolution. For micromachined devices with large features, high resolution photoplots are less expensive and quicker to obtain than glass mask sets. A photoplot is used in the mask aligner by attaching it to a glass plate with double sided tape such that the laser written side of the photoplot is facing away from the glass. The photoplot side of the glass plate is then aligned to and brought into contact with the photoresist covered wafer. Seven devices were arrayed on the mask design for fabrication on 100mm diameter silicon wafers.

The fabrication process for producing the micromachined silicon spring-mass-damper platform is summarized below. The detailed fabrication process flow utilized for actual fabrication of the devices is presented in Appendix B. A nominally 375μm thick (100) n-type Si double-side polished wafer with a resistivity of 1-10Ωcm was used to fabricate the spring-mass-damper platform. After the wafer was cleaned, it was subjected to a two hour wet thermal oxidation to grow a layer of silicon dioxide on both sides of the wafer, nominally 0.5μm thick. The wafer was processed in preparation for photolithography and the first mask was aligned to the wafer flat. The mask pattern was then transferred to the photoresist layer. This side was subsequently referred to as the top side of the wafer. The exposed silicon dioxide on the top side of the wafer was removed by reactive ion etching (RIE) using a CF_4 and CHF_3 plasma chemistry. Then the exposed

silicon on the top side of the wafer was dry etched using DRIE to a depth of approximately 40μm, which set the thickness of the springs. After DRIE was completed, the remaining photoresist on the top side of the wafer was removed with oxygen plasma. Then the bottom side of the wafer was prepared for photolithography and the second mask pattern was aligned to the etched pattern on the top side of the wafer and transferred to the photoresist on the bottom side. The wafer was then dipped in buffered oxide etchant (BOE) to remove the exposed silicon dioxide on the bottom side of the wafer and all remaining silicon dioxide on the top side of the wafer. After cleaning with de-ionized (DI) water, the exposed silicon on the bottom side of the wafer was DRIE etched to a depth of approximately 100μm. Then the wafer was carefully cleaved to separate each of the seven partially etched devices. Each device was then mounted on a holder wafer with photoresist so that the partially etched bottom side was exposed. Each die was then independently DRIE etched approximately 235μm until the proof mass was fully released. Each die was independently etched because the DRIE etch rate across the face of a wafer varied and if all seven devices were etched together, some would be overetched by the time all of the devices had been fully released. Overetching would reduce the thickness of the 40μm thick springs once the proof mass had been released. After a device had been released, it was removed from the holder wafer and cleaned in separate acetone and DI water baths, and allowed to air dry. Multiple devices were then placed in the electron beam deposition system where the top side of each device was cleaned by 2min of argon ion sputtering followed by the deposition of thin film metallization. Several different metallizations were investigated. However, 800A of titanium for an adhesion layer to the bare silicon followed by 2000A of gold provided a

satisfactory low resistance electrical path to the silicon device. After micromachining was complete, a 5mm by 5mm bare silicon die was attached to the device proof mass pad, using cyanoacrylate glue, to increase the total proof mass. A photograph of a micromachined silicon spring-mass-damper platform is presented in Figure 4.12.
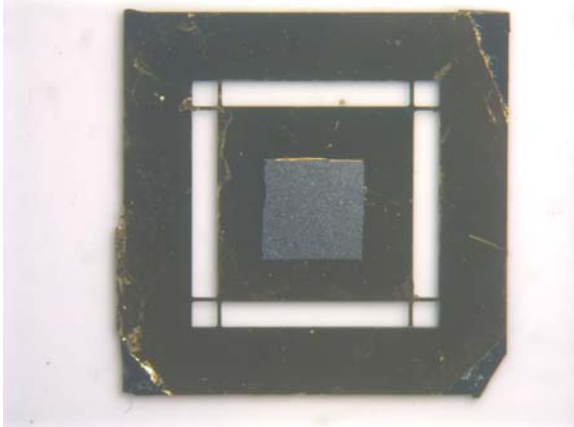
Figure 4.12. A photograph of a micromachined silicon spring-mass-damper platform.

4.3 Development of the Sensor Interface Electronics

A round, 3.4mm diameter metallized landing on the backside of the printed circuit board (PCB) containing the sensor interface electronics was utilized for the second electrode. An approximately 100μm thick nonconductive polyester spacer was used to mount the micromachined silicon spring-mass-damper platform over the bottom electrode on the circuit board. After assembly, the 3.4mm diameter bottom electrode rested approximately under the center of the micromachined top electrode, with a rest gap of nearly 100μm.

The fabricated prototype interface circuit consisted of three stages and used the Texas Instruments OPA445 FET-input op amp. This amplifier was selected due to its high input impedance, wide power supply operating range ($\pm$10V to $\pm$45V), high slew rate (15V/μs), surface mount footprint and commercial availability. The interface circuit was powered with $\pm$25V, with +25V applied across the velocity sensing capacitor, C_s. A schematic diagram of the first stage is presented in Figure 4.13, consisting of a low impedance current to voltage conversion amplifier and an output low pass filter. Since the operational amplifier had a tendency to become unstable with a capacitive input, the 10kΩ R8 was added between the positive and negative inputs of the op amp. The 100kΩ R1 resulted in a first stage gain of -100,000Ω. The amplifier gain was measured in Ohms because the input was a current and the output was a voltage. C1 and R2 formed a one pole passive low pass filter with a designed cutoff frequency of 28.421KHz and was used to attenuate any high frequency noise present in the first stage.
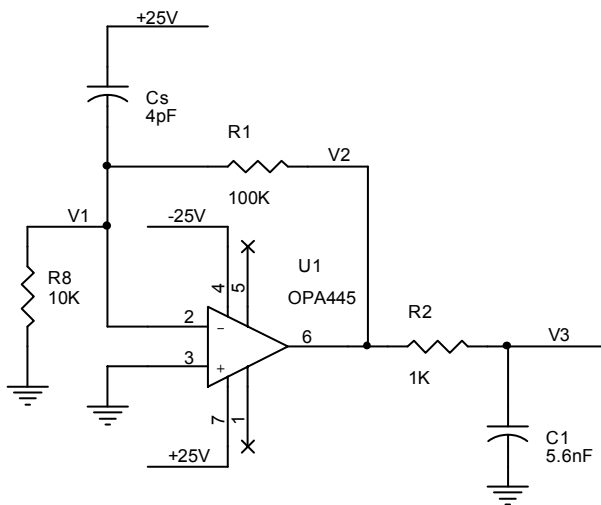
Figure 4.13. A schematic diagram of the first stage of the sensor interface circuit.

A schematic diagram of the second stage is presented in Figure 4.14. It consisted of a noninverting amplifier circuit with a gain of 101. The third stage, presented in Figure 4.15, consisted of an input high pass filter and an inverting amplifier with a gain of -100. The input high pass filter was a one pole passive RC filter consisting of C2 and R5, with a designed cutoff frequency of 33.86Hz and was used to AC couple the output voltage from the second stage to the third stage. Without the high pass filter, the DC offset voltage from the op amp in the first stage would be amplified by 101 in the second stage and then by -100 in the third stage and would become large enough to saturate the third stage amplifier. Three stages were used to produce the required gain while maintaining sufficient bandwidth in each amplifier stage.
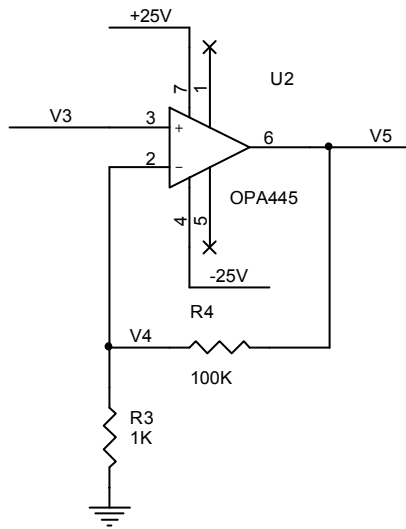
Figure 4.14. A schematic diagram of the second stage of the sensor interface circuit.
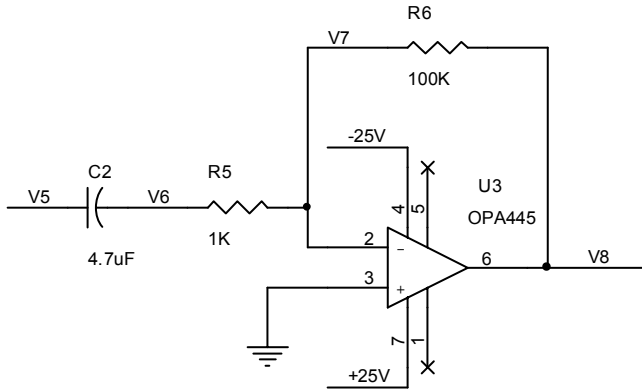
Figure 4.15. A schematic diagram of the third stage of the sensor interface circuit.

The interface circuit was simulated in PSPICE and the input data file is presented in Appendix C. The frequency response magnitude and phase plots of the output voltage, V8, from the PSPICE AC analysis of the interface circuit are presented in Figure 4.16. The circuit had a band pass response with 3dB cutoff frequencies at approximately 33.2Hz and 11.22KHz. Therefore the velocity sensor with the interface electronics included was potentially useful over this frequency range.
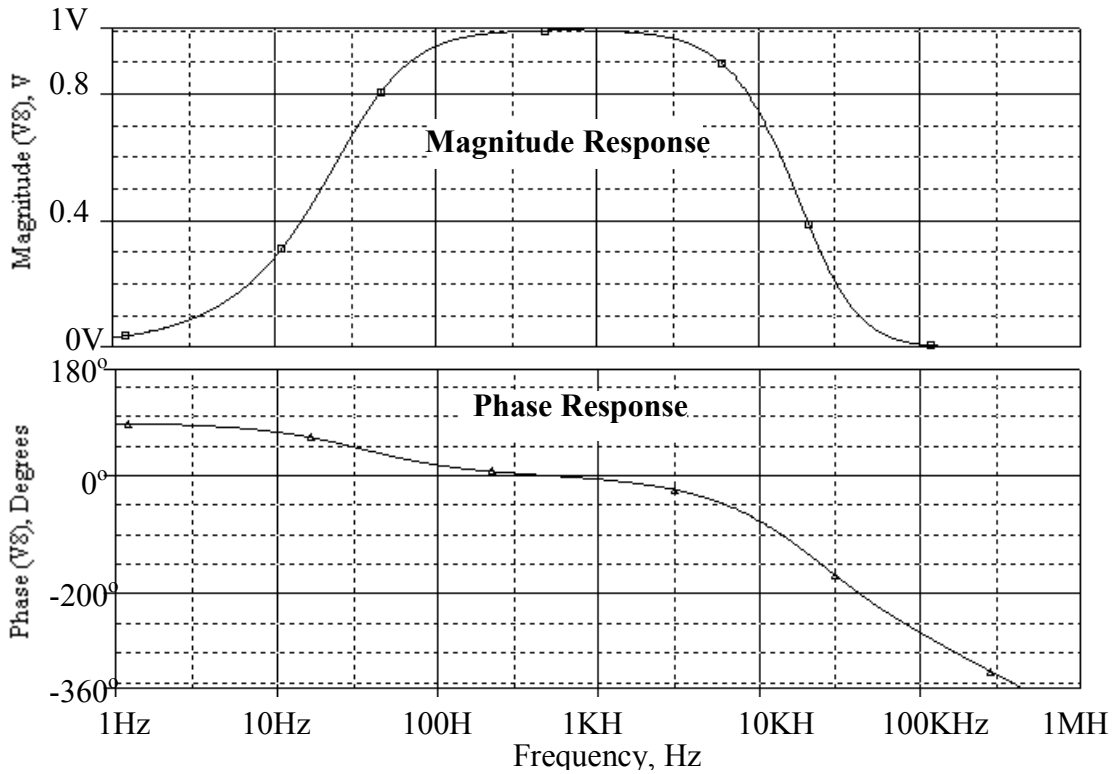
Figure 4.16. The interface circuit frequency response magnitude and phase plots of V8 from the PSPICE AC analysis.

The sensor interface circuit was implemented in surface mount components on the front side of a double layer printed circuit board, with the bottom electrode of the relative velocity sensor implemented on the back side of the circuit board. Photographs of the front and back sides of the sensor interface circuit printed circuit board are presented in Figure 4.17. The four large plated holes were for mounting screws. A center 508μm diameter plated via electrically connected the 3.4mm diameter bottom electrode to the sensor interface circuitry on the opposite side of the printed circuit board. The annular ring electrode was left unused, but was intended for future applications that could utilize a PPA in conjunction with the relative velocity sensor. The mounting frame on the

printed circuit board was not electrically connected to the sensor interface circuit. It was the same height as the bottom electrode and was utilized as a platform onto which the nonconductive polyester spacer was placed.
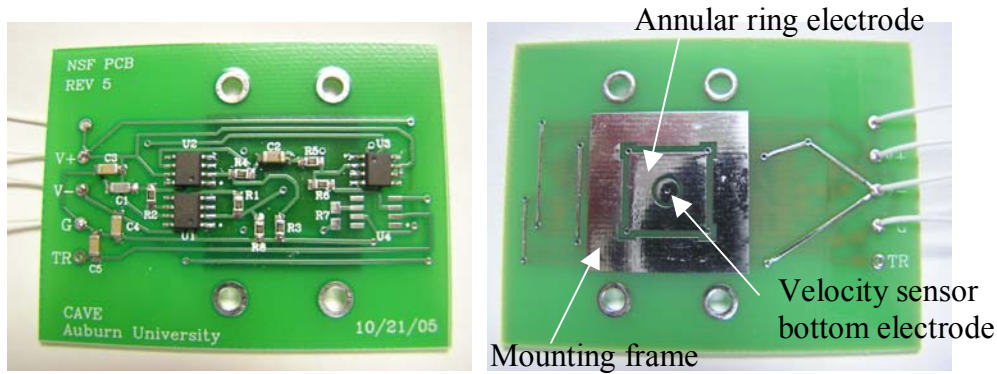
Figure 4.17. Photographs of the (a) front and (b) back sides of the printed circuit board used to implement the relative velocity sensor interface circuit.

Substituting the designed values for x_o (100μm), R_b (100KΩ), ε_o (8.854pF/m), ε_r (1) and A (9.0792E-6m^2) into (3.7) and multiplying the result by the second and third stage amplifier gains (10100), the equation for the sensor output voltage becomes

$$V_o(t) = \frac{(8.1191x10^{-8})V_b \omega x_A \cos(\omega t)}{(1x10^{-4} + x_A \sin(\omega t))^2} .$$

(4.3)

4.4 Assembly of the Prototype Relative Velocity Sensor

The micromachined silicon spring-mass-damper platform, the polyester spacer and the interface circuit printed circuit board were assembled together to realize the

prototype relative velocity sensor. A machined plastic housing was used to hold the components of the prototype relative velocity sensor with a pressure fit obtained using four screws. An exploded view photograph of the prototype relative velocity sensor is presented in Figure 4.18. The components in the photograph in Figure 4.18, from top left to lower right, are the top section of the plastic housing with the micromachined silicon spring-mass-damper platform in its center, the bottom section of the plastic housing, four metric 3-12 stainless steel socket head cap screws, a nominally 320μm thick black plastic shim, the nonconductive plastic spacer and the interface electronics printed circuit board. The machined plastic housing consisted of a top and a bottom section. The bottom section had a screw protruding out of its bottom side so that the prototype relative velocity sensor could be easily mounted onto the head of an electromechanical shaker for evaluation. The top side of the bottom section had a trench machined into its face that allowed room for the electronic components on the front side of the interface circuit printed circuit board. Four metric #3 threaded screw holes had been tapped into the bottom section for holding the other sensor components in place. The top section of the plastic housing was covered with copper foil tape, except over the four screw holes and a center square hole that the springs and proof mass pad of the silicon device were aligned to. The top side frame of the silicon device rested on the copper foil, which achieved a low resistance electrical connection between the copper foil and the silicon device. On one end, the copper foil tape extended beyond the edge of the top section of the plastic housing so that a wire could be soldered to the copper foil tape in order to establish an electrical contact with the sensor top electrode.
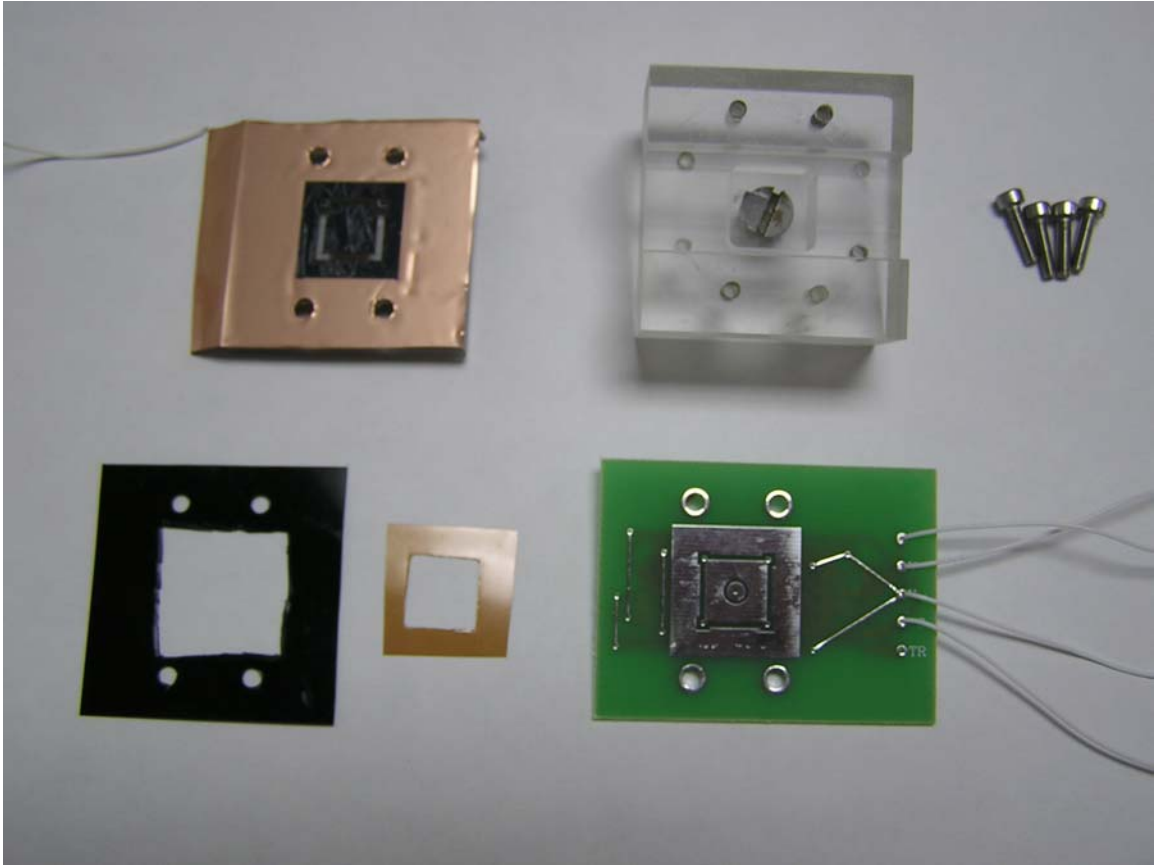
Figure 4.18. An exploded view photograph of the prototype relative velocity sensor.

The assembly procedure began with placing the printed circuit board on top of the bottom section of the plastic housing such that the sensor bottom electrode faced up and the four mounting holes in the printed circuit board were aligned with the four tapped holes in the plastic housing. Then the 100μm plastic spacer was placed on top of the mounting frame that surrounds the bottom electrode. Next, the 320μm thick black plastic shim was placed on top of the assembly such that the four holes in it were aligned with the tapped holes in the plastic housing. This resulted in the plastic spacer residing in the large hole in the center of the shim. The thickness of the shim was close to the thickness of the silicon die and therefore minimized bending in the top section of the plastic

housing after the unit had been assembled. Then the micromachined silicon device was carefully placed on top of the plastic spacer and aligned so that it was approximately centered over the bottom electrode. The top section of the plastic housing was then placed on top of the assembly and aligned so that the screw holes were aligned. The head cap screws were then inserted into the top section of the plastic housing and tightened. The top section of the plastic housing pressed against the frame around the periphery of the micromachined silicon device and pressed it against the plastic spacer, which held it securely in place.

CHAPTER 5

TESTING AND RESULTS

This chapter presents the procedure for and results from testing the fabricated prototype relative velocity sensor that was discussed in Chapter 4. The testing included capacitance measurement of the sensor at rest, functional testing of the sensor interface circuit and dynamic evaluation of the prototype relative velocity sensor. The data collected from testing the prototype sensor was analyzed and compared with the predicted sensor behavior to validate the theoretical development of the relative velocity measurement technique developed in Chapter 3. Discrepancies between the theoretical model and observed data are noted and explained.

5.1 Rest Capacitance Measurement

A capacitance of 1.2pF was measured between the two electrodes of the assembled prototype relative velocity sensor while using air as the dielectric material between the electrodes. Using the equation for calculating the capacitance of a simple parallel plate capacitor (2.1) with a fixed rest gap, the calculated rest gap distance was 66.99μm, even though the plastic spacer was approximately 100μm thick. The difference between the calculated rest gap distance and the nominal thickness of the plastic spacer

can be attributed to the measurement of stray capacitance in the capacitance measurement setup, compression of the spacer during assembly and fringing effects between the two electrodes that are not accounted for in (2.1)

5.2 Electrical Testing of the Sensor Interface Circuit

After verifying that the sensor interface circuit was correctly assembled, the fabricated prototype sensor was electrically tested by connecting a function generator directly to the relative velocity sensor top electrode and a sinusoidal voltage input was applied across the sensor capacitor. Since the bottom electrode was connected to a virtual ground, the current flowing through the sense capacitor was theoretically equal to

$$\bar{I} = j\omega\bar{V} \,. \tag{5.1}$$

Therefore by sweeping the frequency of the sinusoidal input over the operating range of the relative velocity sensor, the characteristics of the interface circuit could be evaluated. Specifically, this test was performed to determine if the interface circuit possessed any resonances over the operational bandwidth of the sensor that would result in additional distortion in the relative velocity sensor response. Therefore, the frequency of the sinusoidal input was stepped in 50Hz increments from 50Hz to 4KHz. From 50Hz through 2KHz, a $1V_{pp}$ amplitude was used. From 2KHz through 4KHz, the amplitude was reduced to $0.5V_{pp}$ to keep the interface circuit third stage voltage amplifier from saturating. The data was then normalized for an equivalent sinusoidal input with an

amplitude of $1V_{pp}$ and was plotted as function of frequency. A plot of the normalized

data versus frequency is presented in Figure 5.1 with the theoretical response computed

using (5.1) and the designed input current to output voltage gain of the interface circuit.

The measured linear response obtained from this test verified that the sensor interface

circuit performed as designed.

Vout Vs. Input Sinusoid Frequency
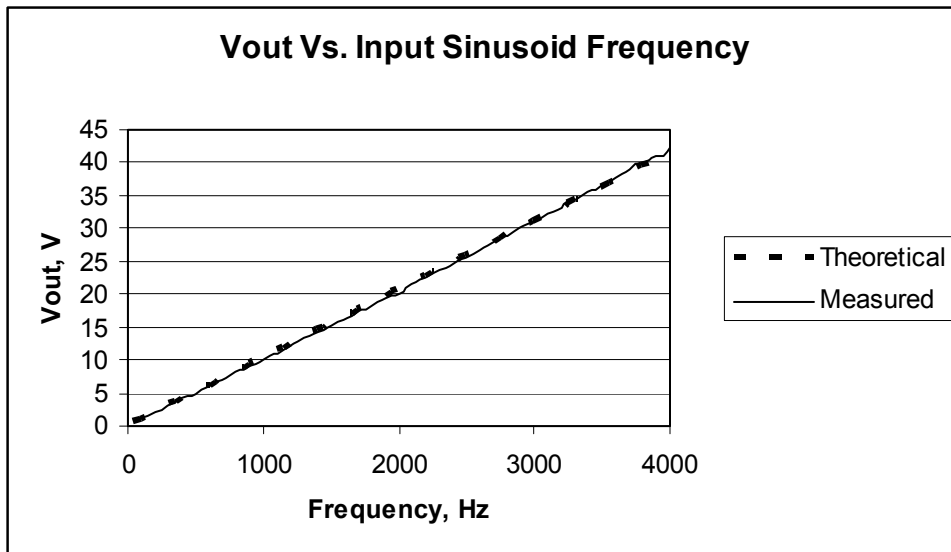
Figure 5.1. A plot of the interface circuit output voltage versus frequency for a constant

amplitude sinusoidal input voltage.

5.3 The Mechanical Set Up for Dynamic Testing

The prototype relative velocity sensor was evaluated by mounting it on the head

of an LDS model V408 electromechanical shaker so that it could be mechanically excited

in a controlled manner. Figure 5.2 presents a photograph of the electromechanical shaker

used to evaluate the performance of the prototype relative velocity sensor. The shaker

Figure 5.2. A photograph of the electromechanical shaker used in evaluating the prototype relative velocity sensor.

was driven by an LDS model PA500L power amplifier that had an uncalibrated gain adjustment knob. Once a gain setting had been selected on the power amplifier, a secondary controller was used to adjust that gain setting from zero to its maximum value by sending a user selected sinusoidal signal with an amplitude ranging from 0V to 3.5355V. During a given test where the excitation level was varied, it was varied by adjusting the secondary controller signal amplitude, V_d. However, since the PA500L power amplifier gain adjustment knob was not calibrated, V_d values have no meaning between different sets of tests. The device mounted on the shaker head in Figure 5.2,

with a white cable connected to it, was an accelerometer that allowed the shaker system to be calibrated before testing of the prototype relative velocity sensor began.
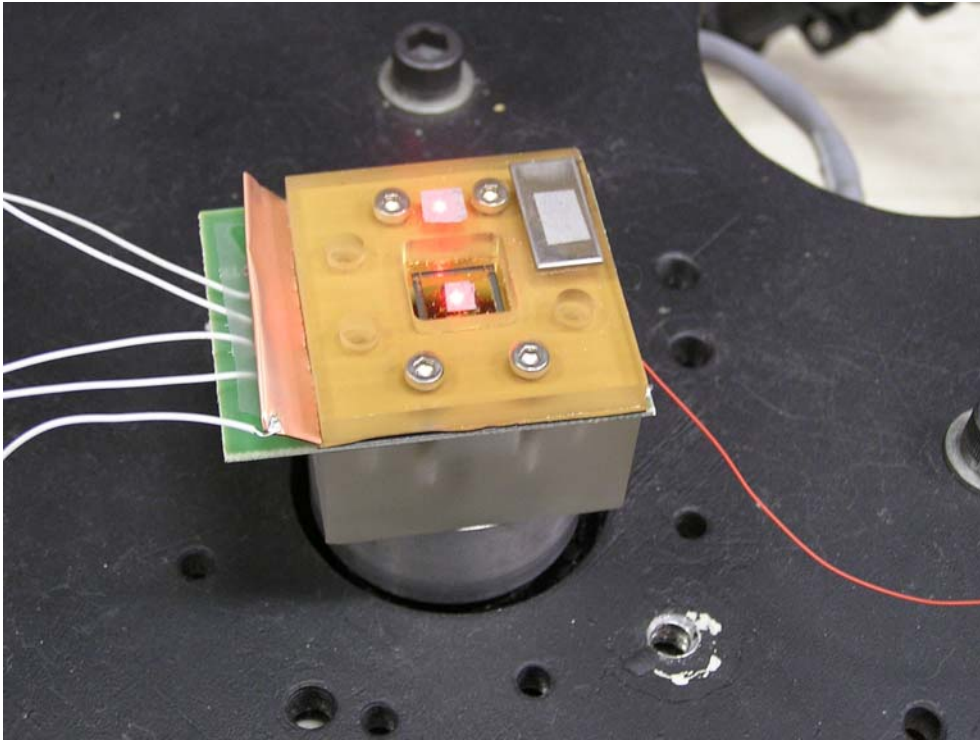

Figure 5.3. A photograph of the prototype relative velocity sensor attached to the shaker head.

Figure 5.3 presents a photograph of the prototype relative velocity sensor attached to the shaker head. The two bright red spots are from two Polytec OFV 353 laser interferometric displacement measurement systems. The laser spot on the proof mass in the center of the sensor unit was used to measure the displacement of the proof mass or upper electrode, while the other laser spot was used to measure the displacement of the frame or lower electrode. The difference between the two laser measurements yielded the relative displacement between the two electrodes. A difference amplifier was

constructed to take the difference between the output voltages from the two laser displacement measurement systems. A schematic diagram of the difference amplifier is presented in Appendix D.

A photograph of the mechanical shaker with the attached sensor unit and the two Polytec laser displacement measurement systems is presented in Figure 5.4. The voltage

Figure 5.4. A photograph of the shaker and the two Polytec laser systems.

output from the sensor interface circuit was run through a two stage analog buffer so that it experienced approximately the same signal delay that the relative displacement voltage incurred through the difference amplifier. The schematic drawing of the two stage analog buffer is presented in Appendix D with the schematic drawing of the difference ampler.

Figure 5.5 presents a photograph of the test set up that includes the breadboarded difference amplifier, the ±25V DC power supplies used to power the prototype relative velocity sensor and the difference amplifier, and an HP 35665A dynamic signal analyzer that was used to capture the relative displacement and the sensor output signals.
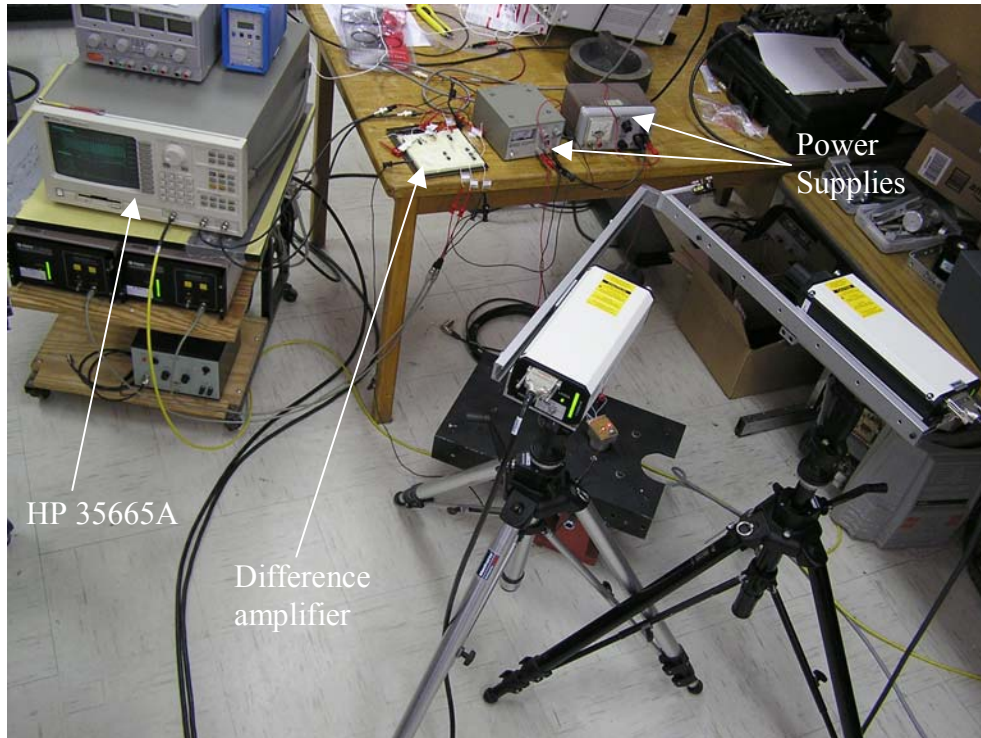

Figure 5.5. A photograph of the sensor evaluation equipment.

5.4 Measurement of the Sensor Mechanical Frequency Response

The mechanical frequency response, or transmissibility, of the unpowered prototype relative velocity sensor was obtained by exciting the device with a wide bandwidth noise source. For single frequency excitation, however, the LDS model V408

electromechanical shaker was only capable of producing a few microns of motion in the 1KHz to 2KHz range. Since the passive micromachined spring-mass-damper device was designed with a natural frequency of 1.39KHz, once the resonant frequency had been determined, the sensor could be tested at that frequency to take advantage of the motion amplification afforded by the underdamped response of the micromachined sensor element. By using this approach, it was determined that the exact resonant frequency of the prototype sensor slightly changed if the unit was disassembled and reassembled or if a different micromachined silicon device was utilized. Changing the tightness of the four mounting screws changed the pressure applied to the micromachined silicon device, which altered its mechanical resonant frequency by pre-stressing the eight springs that attached the proof mass pad to the surrounding frame. However, this had no effect on the experimental verification of the relative velocity measurement technique.

Figure 5.6 presents a measured mechanical frequency response plot of the prototype relative velocity sensor with the interface electronics unpowered. The device had a second order underdamped low pass response with a resonant frequency at 1.34KHz and a mechanical Q factor of approximately 20. Therefore a 1µm amplitude excitation at 1.34KHz could excite motion in the proof mass with an amplitude of approximately 20µm.
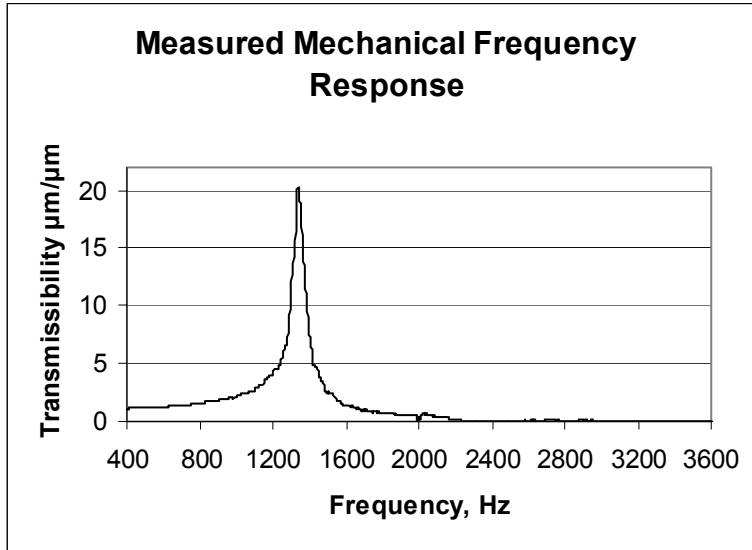
Measured Mechanical Frequency Response

Figure 5.6. The measured mechanical frequency response of the unpowered prototype relative velocity sensor.

5.5 Velocity Sensor Prototype Single Point Testing

Utilizing the results of the mechanical frequency response measurement, the shaker was programmed to excite the test article at the resonant frequency, 1.34KHz, while the time responses of the relative displacement between the two electrodes and the sensor interface circuit output voltage were recorded, as presented in Figure 5.7. The relative electrode displacement had the strongest component at 1.34KHz. with smaller components at other frequencies. Figure 5.8 presents a spectral response from computing a 512 point FFT on the measured relative displacement and velocity sensor output data.
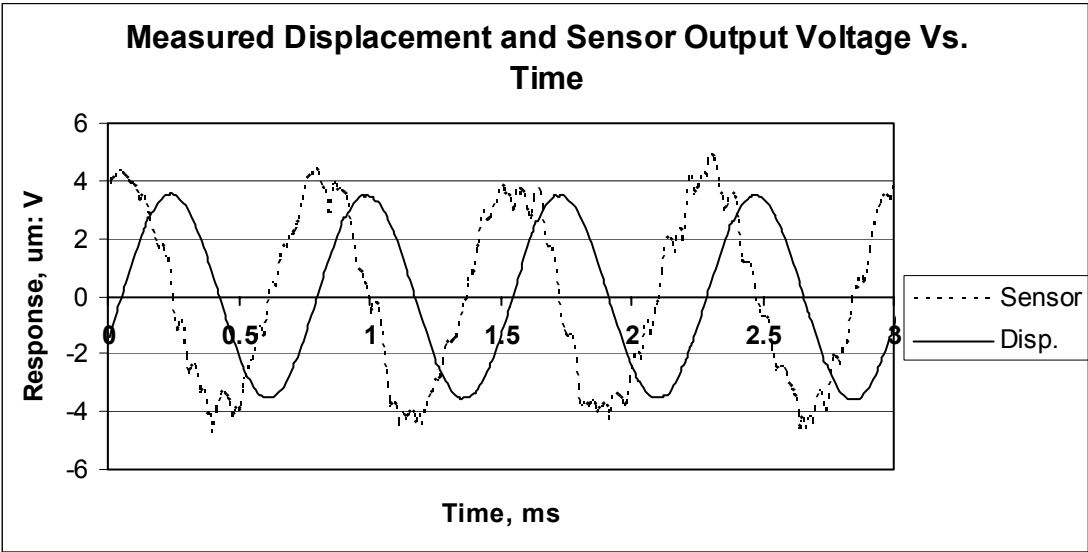
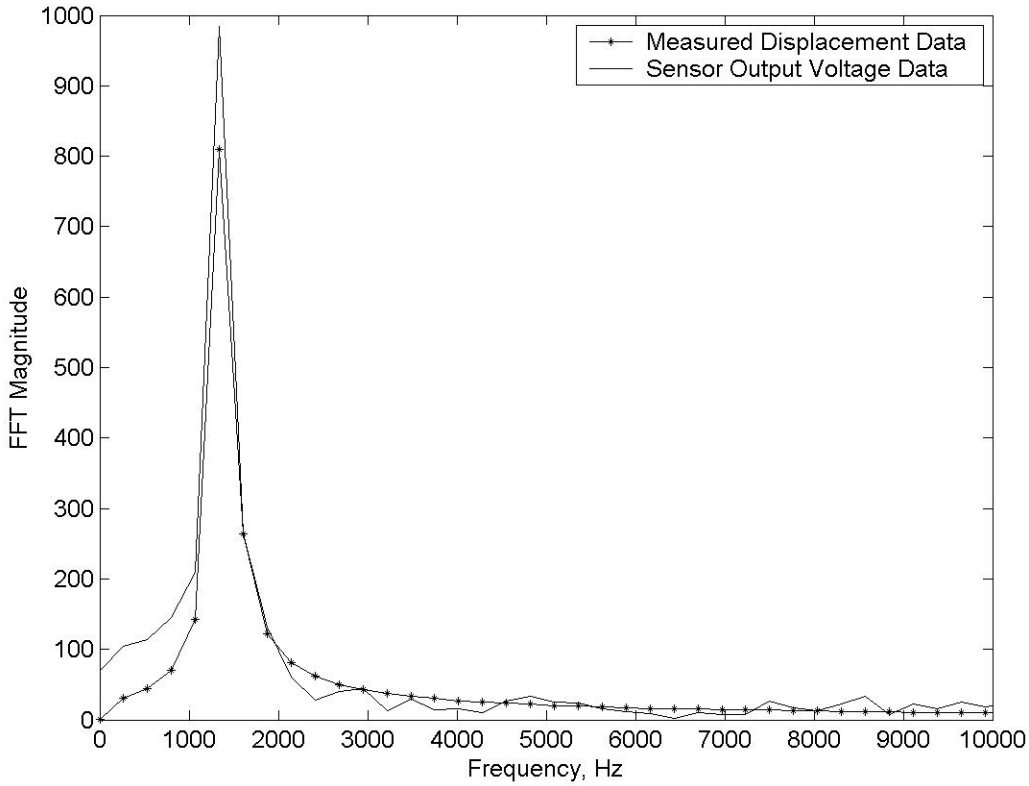Figure 5.7. 3ms of measured relative displacement and velocity data for the 1.34KHz test.

Figure 5.8. Spectral response of the relative displacement and velocity data.

Analysis of the recorded data revealed that the fundamental frequency in the sensor interface circuit output signal was 90° out of phase with the relative electrode displacement signal such that the sensor output was positive only when the displacement was increasing, which would be characteristic of the relative velocity between two electrodes experiencing a sinusoidal displacement. This can be observed by numerically calculating the time derivative of the measured relative displacement data, as presented in Figure 5.9, and comparing it with the measured output signal from the relative velocity sensor. The resulting waveform from calculating the time derivative of the measured displacement data was amplified so that the amplitude of the fundamental component was approximately the same as the amplitude of the fundamental component of the sensor output voltage waveform, so that the quality of the two signals could be compared. Although the overall sensor output signal was somewhat distorted, it was relatively clean at the crossover points where the direction of velocity changed. Therefore this sensor may be particularly useful for detecting the direction of relative velocity as opposed to measuring the absolute relative velocity. From the 512 point FFT of the recorded sensor output voltage data, the amplitude of the sensor output voltage at the fundamental frequency of 1.34KHz was 3.844V. The 512 point FFT of the measured displacement data revealed an amplitude of 3.1623µm at 1.34KHz. This compares to a predicted sensor output voltage amplitude of 5.40V using (4.3) with a V_b of 25V and a x_A of 3.1623µm with the $x_A\sin(\omega t)$ term in the denominator neglected. The discrepancy between the measured and predicted relative velocity signal amplitudes can be attributed to constants in (4.3), such as the rest gap distance, the voltage across the sense capacitor, the gains of the three amplifier stages, etc… having slightly different values than those

96

designed and modeled in (4.3). The distortion of the relative velocity waveform was due to several factors. One factor was the nonlinearity of the sensor response as modeled by (4.3) and previously demonstrated in Figure 3.7, which produces high frequency harmonics in the output signal.
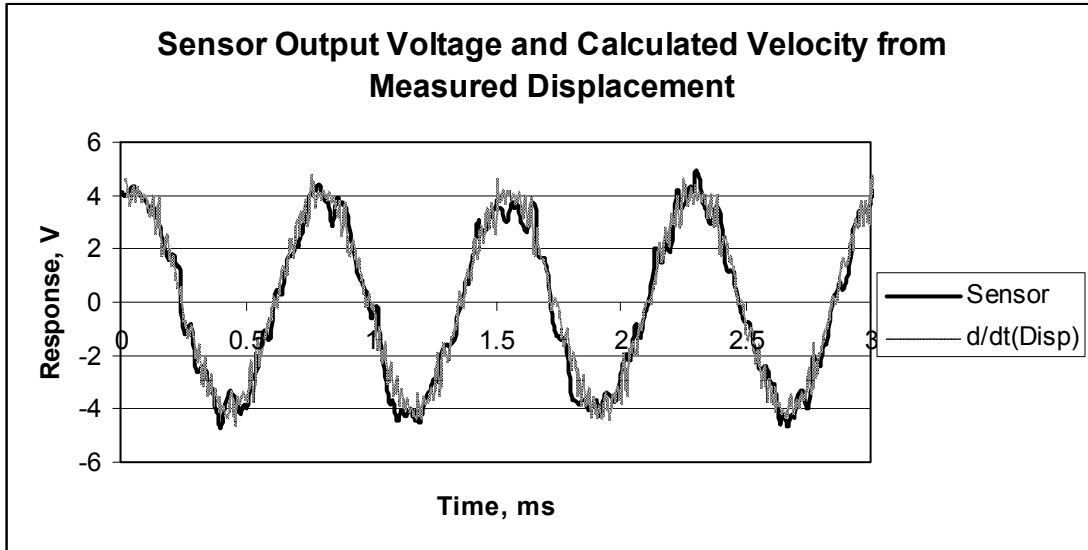

Figure 5.9. The calculated time derivative of the measured relative displacement data and the measured relative velocity sensor data for the 1.34KHz test.

Another contributing factor to signal distortion is noise in the first stage of the interface circuit. Using (4.3) with the assumption the $x_o >> x_A$ so that the $x_A \sin(\omega t)$ term can be neglected, the first stage amplifier output voltage, V2, in Figure 4.13 would have an amplitude of 535.1μV and an RMS value of 378.4μV. Using the specified 3dB bandwidth for the sensor interface circuit from Figure 4.16, and the input voltage noise density and the current noise density specifications for the OPA445 op-amp [49], the noise voltage at V2 resulting from the sum of the squares of the corresponding V2

voltage terms arising from the thermal noise voltages for R1 and R8, the input noise voltage of the op amp at the non-inverting input and the input noise current of the op amp at the inverting input is calculated to be 22.56µV, which is approximately 6% of the magnitude of the sensor output voltage at V2 [50, 51]. This results in a theoretical SNR of 24.5dB. External sources of noise and interference can also contribute to distortion in the measured velocity waveform, since the output current of the sensor is relatively small, with an amplitude on the order of 5nA to 6nA in the prototype evaluated. Higher order effects such as fringing which have not been included in the sensor model could also result in a small increase in distortion.

The velocity sensor prototype consisted of a highly underdamped MEMS spring-mass-damper structure that was externally excited at its resonant frequency of 1.34KHz. However, consider the application of the velocity sensor when it is utilized over a wider bandwidth, such as through internal excitation using a PPA. Assume for discussion purposes that the single frequency sinusoidal motion still has a fixed amplitude of 3.1623µm and a rest gap of 100µm. The relative velocity is then proportional to frequency according to (3.2). If a detection technique such as carrier detection using a second order phase-locked loop (PLL), which generally requires a minimum SNR of 3dB [52], is utilized to detect the sensor output signal, then the minimum detectable sinusoidal velocity frequency can be calculated for a constant amplitude electrode motion using

$$SNR = 20Log(\frac{378.4f}{1340*22.56}).$$

(5.2)

For a frequency of 1.34KHz, the SNR is 25.4dB as previously discussed. Therefore, for the prototype velocity sensor evaluated, the estimated minimum detectable sinusoidal velocity frequency with a 3.1623µm amplitude electrode motion is 112.8Hz.

5.6 Velocity Sensor Prototype Swept Gain Testing

A second test of the prototype relative velocity sensor was performed where the sensor was excited at the measured passive mechanical resonant frequency as the amplitude of excitation was varied. This test was performed to investigate the SNR of the sensor output and the occurrence of higher harmonics due to the nonlinear characteristics of the sensor. Since the prototype sensor had been disassembled and then reassembled with a different interface electronics circuit board than was used during the first test, the passive frequency response was again measured to determine the passive resonant frequency of the micromachined spring-mass-damper device. A plot of the measured passive frequency response is presented in Figure 5.10. This time the device also had a resonant frequency of 1.34KHz and a mechanical quality factor of approximately 22. The control voltage transmitted to the shaker power amplifier was varied from 200mV to 3.4008V. Below 200mV the sensor output was extremely noisy. 3.4008 was close to the maximum output voltage of the controller, 3.5355V. At each controller voltage interval, 2048 data samples were recorded while the shaker was excited with a 1.34KHz sinusoidal input. Each time trace shows the first 3ms of measured relative displacement and sensor output voltage data. Each spectral response was

generated by performing a 2048 point FFT on the 2048 relative displacement and sensor output voltage samples using MATLAB.

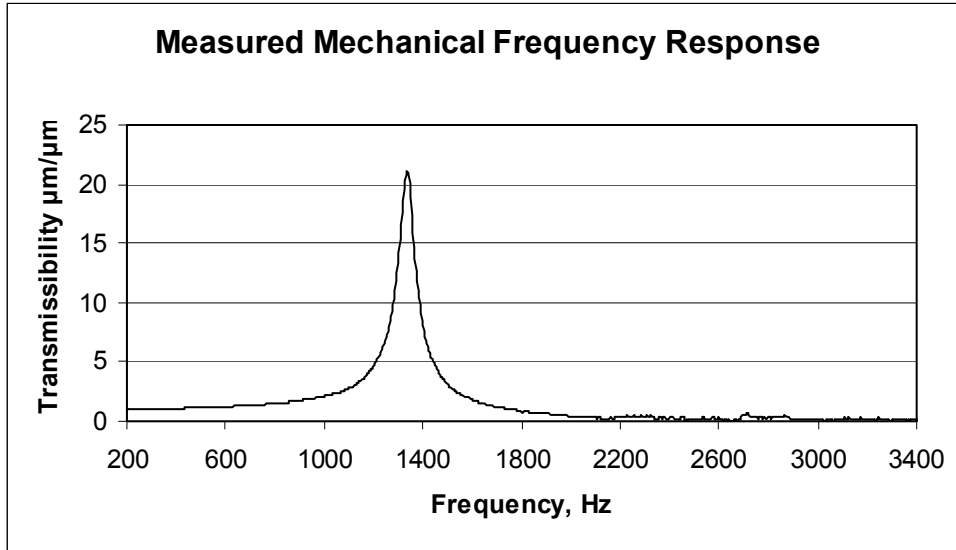**Measured Mechanical Frequency Response**

Figure 5.10. The measured mechanical frequency response of the unpowered prototype relative velocity sensor.

Figures 5.11 and 5.12 present the time trace data and spectral responses for the data collected with the shaker controller set at 200.13mV. From the time trace of the sensor output voltage, it was evident that the sensor output signal strength was relatively low compared to the noise floor. From the FFT of the measured data, the amplitude of the relative displacement was approximately 0.86μm and the amplitude of the velocity sensor output was approximately 1.32V. Using $22.56\mu V_{RMS}$ as the noise floor for the output voltage from the first stage of the interface circuit, the estimated SNR of the sensor output voltage at 1.34KHz was 12.3dB. Assuming that the electrode rest gap distance was 100μm, then the x_o/x_A ratio was 115.7 to 1. Higher harmonics from the

nonlinear characteristics of the sensor were not visible in the spectral response in Figure
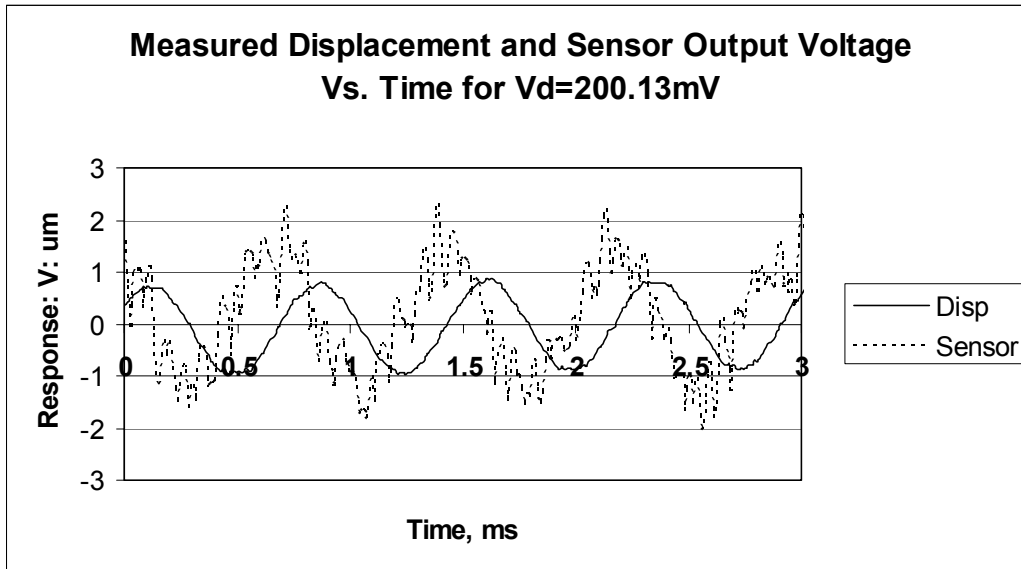
5.12.

Measured Displacement and Sensor Output Voltage Vs. Time for Vd=200.13mV

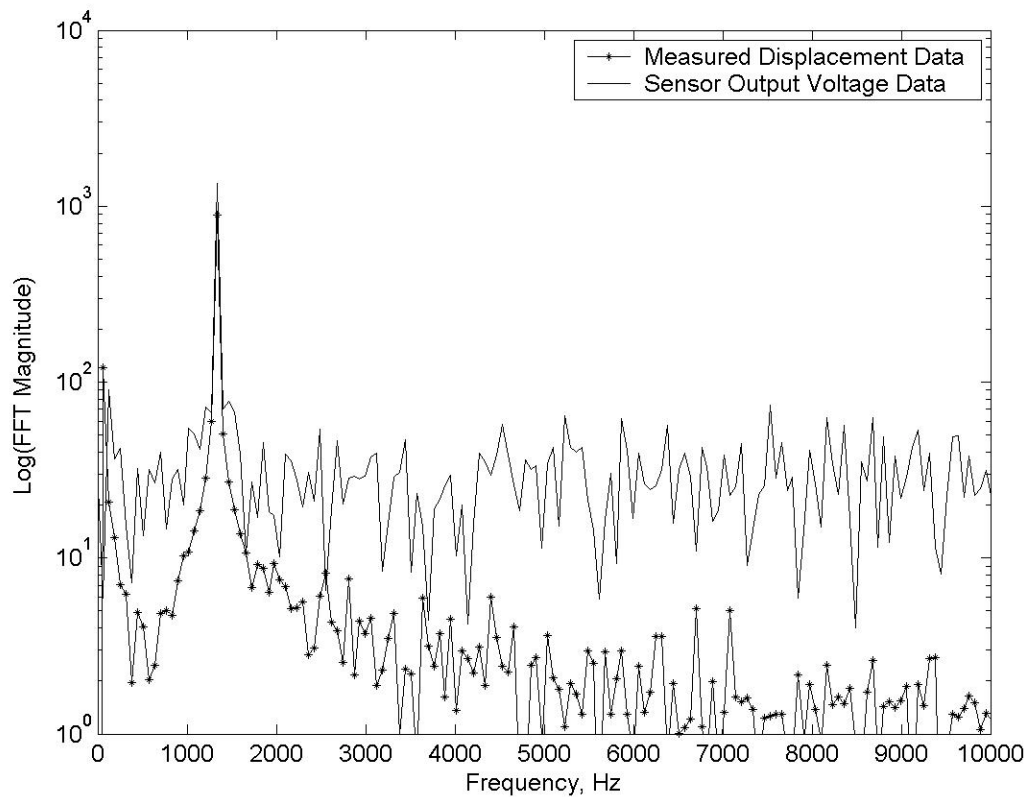Figure 5.11. 3ms of measured relative displacement and velocity data for V_d=200.13mV.

Figure 5.12. Spectral response of the relative displacement and velocity data for V_d=200.13mV.

Figures 5.13 and 5.14 present the time trace data and spectral responses for the data collected with the shaker controller set at 400.62mV. From the time trace of the sensor output voltage, it was evident that the sensor output signal strength was stronger than in the previous case when the shaker controller was set at 200.13mV. From the FFT of the measured data, the amplitude of the relative displacement was approximately 1.68μm and the amplitude of the velocity sensor output was approximately 2.58V. The estimated SNR of the sensor output voltage at 1.34KHz was 18.1dB and the estimated

x_o/x_A ratio was 59.4 to 1. Higher harmonics were still not discernable in the spectral response in Figure 5.14.
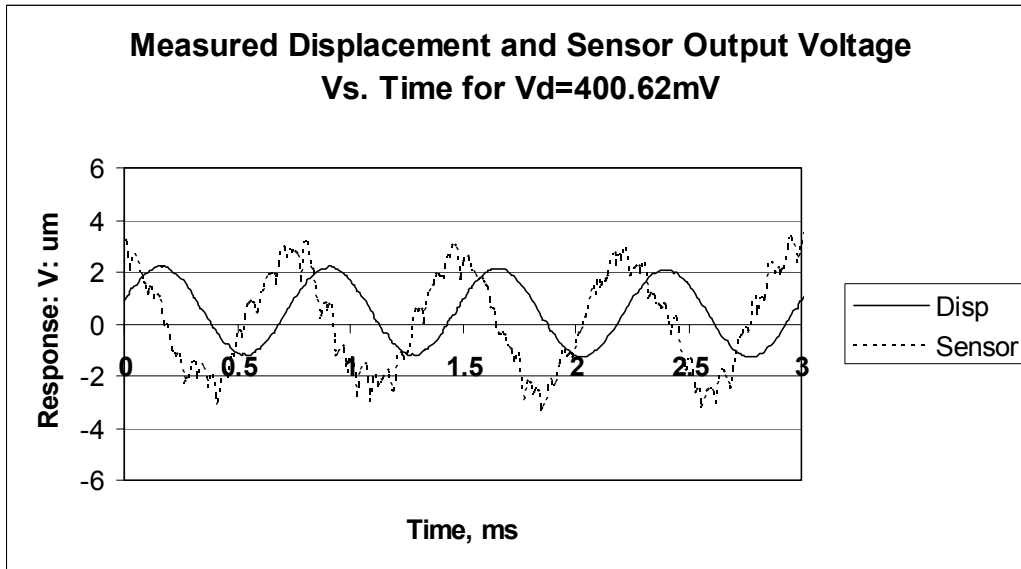
Measured Displacement and Sensor Output Voltage Vs. Time for Vd=400.62mV

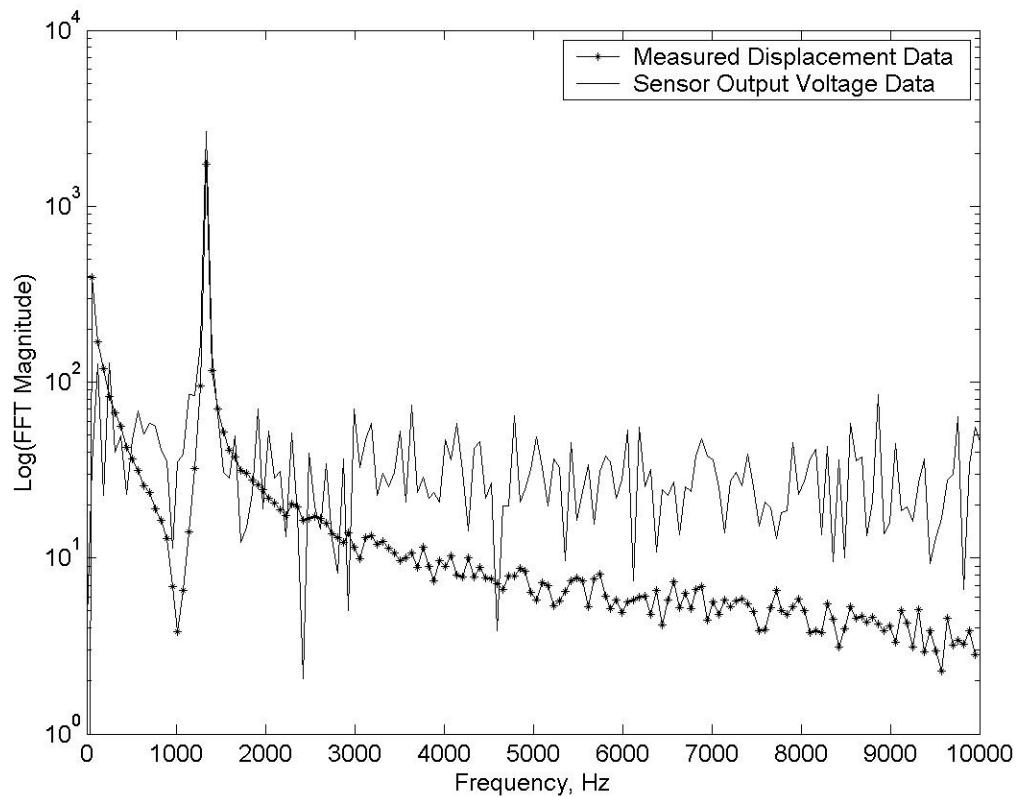Figure 5.13. 3ms of measured relative displacement and velocity data for V_d=400.62mV.

Figure 5.14. Spectral response of the relative displacement and velocity data for V_d=400.62mV.

Figures 5.15 and 5.16 present the time trace data and spectral responses for the data collected with the shaker controller set at 1.0006V. The sensor output signal was much larger and cleaner than in the previous two cases. From the FFT of the measured data, the amplitude of the relative displacement was approximately 4.00μm and the amplitude of the velocity sensor output was approximately 6.37V. The estimated SNR of the sensor output voltage at 1.34KHz was 25.9dB and the estimated x_o/x_A ratio was 25.0 to 1. The first harmonic at 2.68KHz was clearly visible in the spectral response in Figure 5.16.
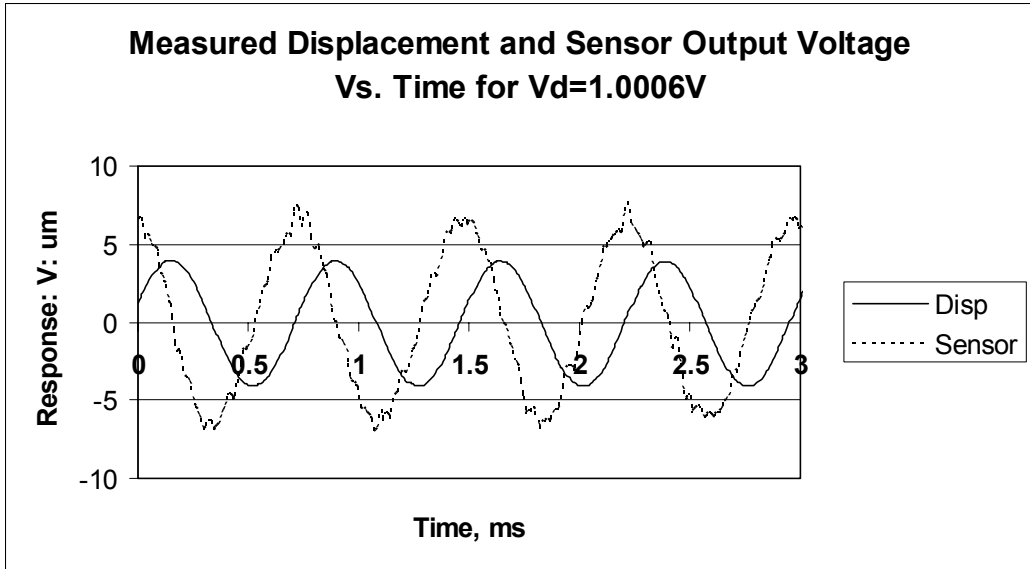
Figure 5.15. 3ms of measured relative displacement and velocity data for V_d=1.0006V.
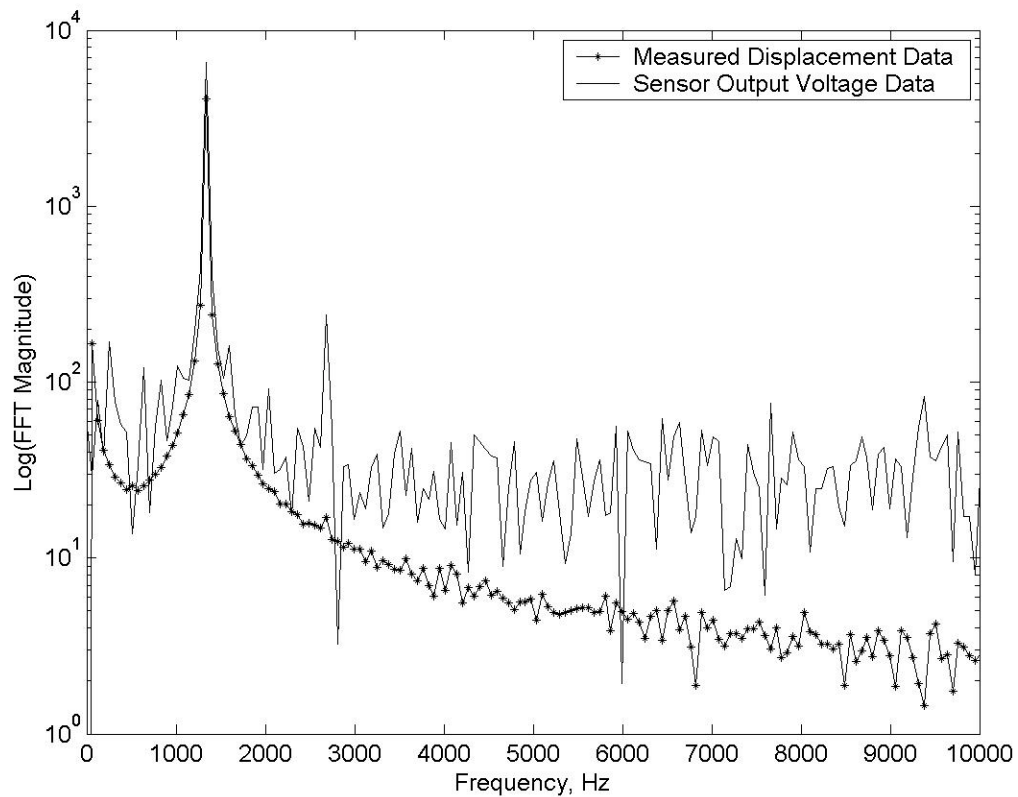
Figure 5.16. Spectral response of the relative displacement and velocity data for V_d=1.0006V.

Figures 5.17 and 5.18 present the time trace data and spectral responses for the data collected with the shaker controller set at 1.8001V. From the FFT of the measured data, the amplitude of the relative displacement was approximately 7.11μm and the amplitude of the velocity sensor output was approximately 11.29V. The estimated SNR of the sensor output voltage at 1.34KHz was 30.9dB and the estimated x_o/x_A ratio was 14.1 to 1. Once again, the first harmonic at 2.68KHz was clearly visible in the spectral response in Figure 5.18, but higher harmonics were not discernable.
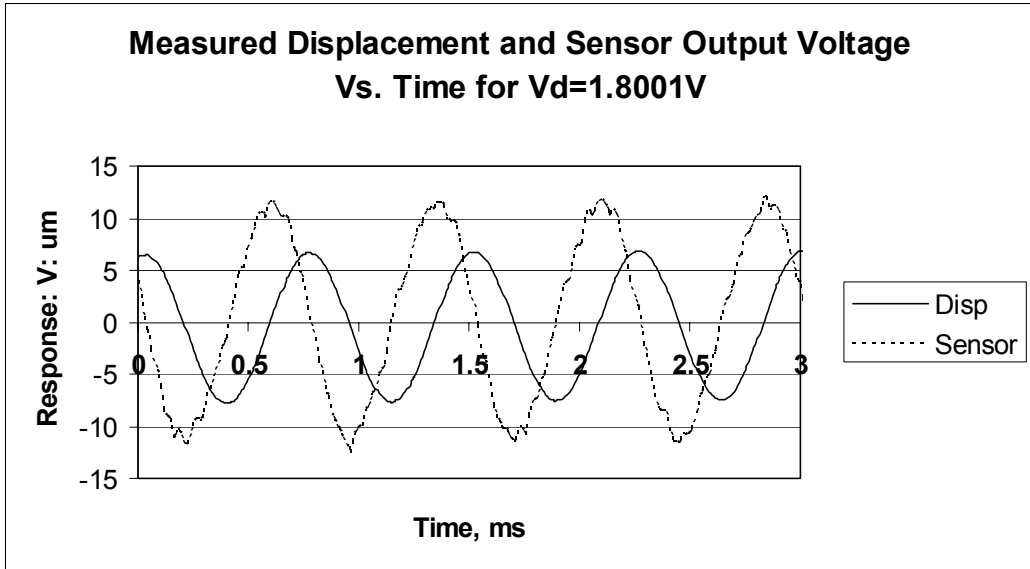
Figure 5.17. 3ms of measured relative displacement and velocity data for V_d=1.8001V.
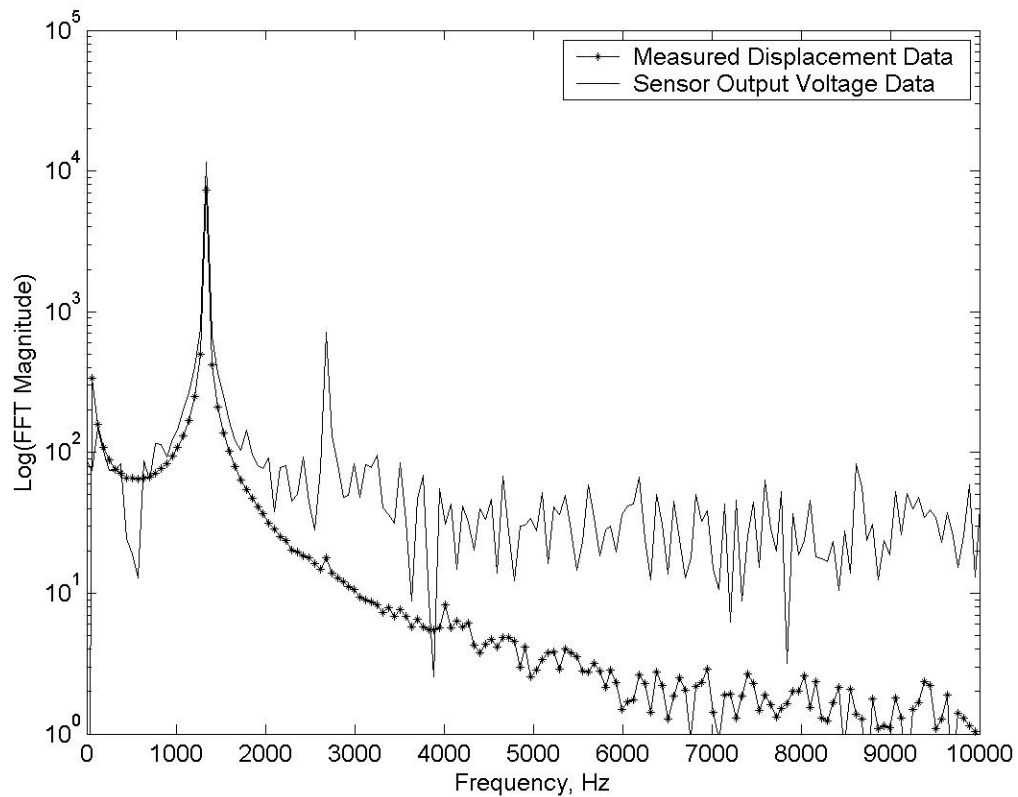
Figure 5.18. Spectral response of the relative displacement and velocity data for V_d=1.8001V.

Figures 5.19 and 5.20 present the time trace data and spectral responses for the data collected with the shaker controller set at 2.8007V. The sensor output signal was large and relatively clean in this case. From the FFT of the measured data, the amplitude of the relative displacement was approximately 10.32μm and the amplitude of the velocity sensor output was approximately 16.57V. The estimated SNR of the sensor output voltage at 1.34KHz was 34.2dB and the estimated x_o/x_A ratio was 9.7 to 1. The first harmonic at 2.68KHz was clearly visible in the spectral response in Figure 5.20, but higher harmonics were not readily discernable.
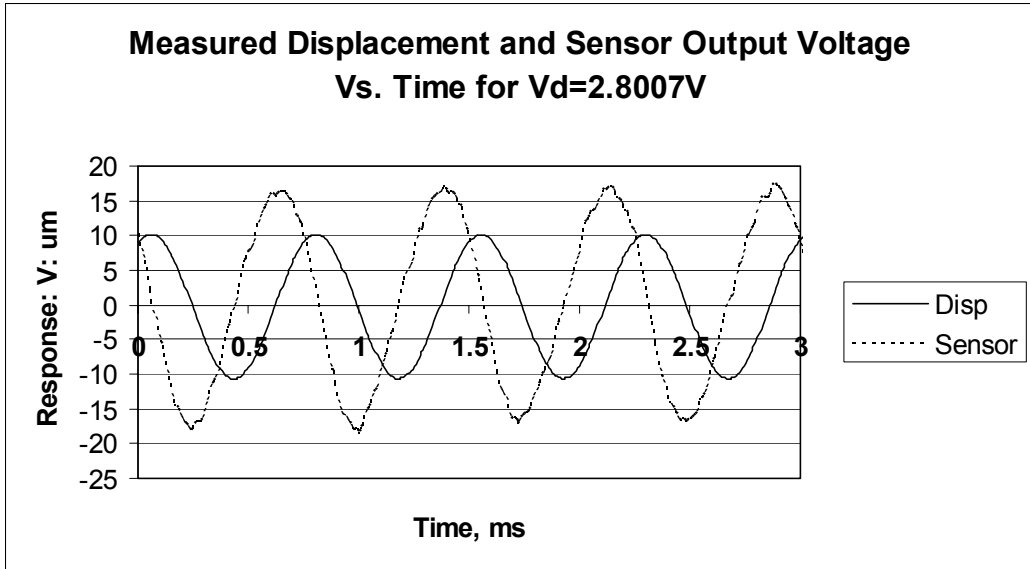
108

Figure 5.19. 3ms of measured relative displacement and velocity data for V_d=2.8007V.
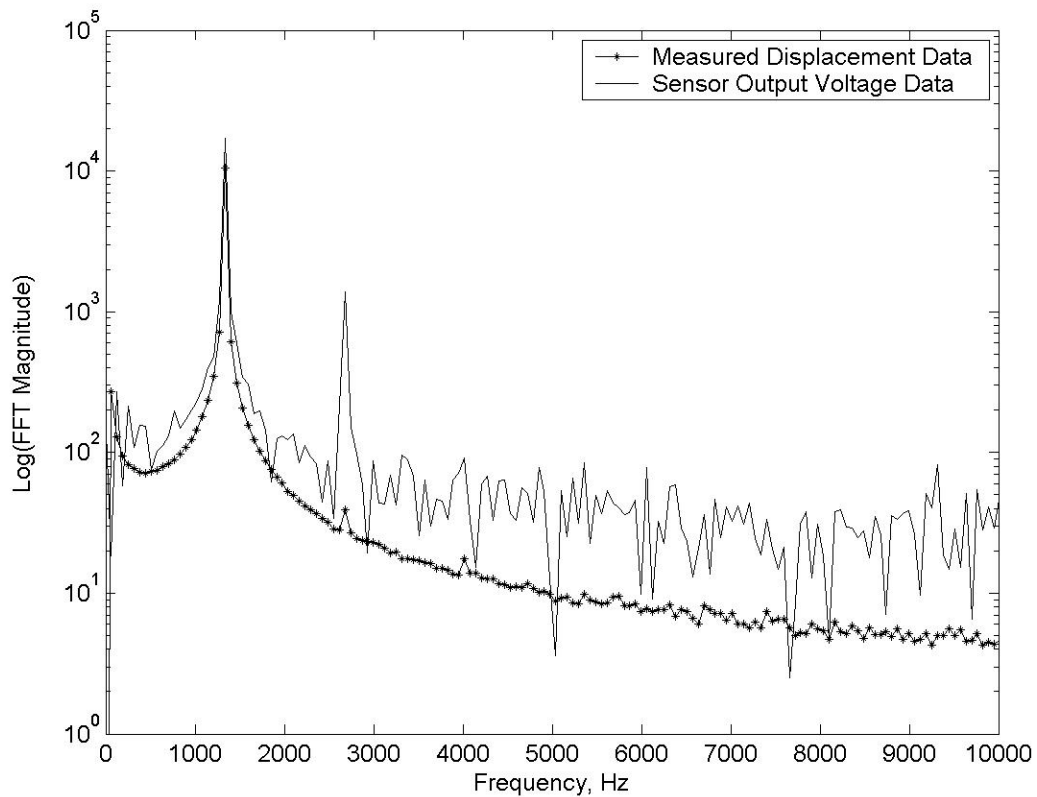
Figure 5.20. Spectral response of the relative displacement and velocity data for V_d=2.8007V.

Figures 5.21 and 5.22 present the time trace data and spectral responses for the data collected with the shaker controller set at 3.4008V. From the FFT of the measured data, the amplitude of the relative displacement was approximately 11.90μm and the amplitude of the velocity sensor output was approximately 19.08V. The estimated SNR of the sensor output voltage at 1.34KHz was 35.5dB and the estimated x_o/x_A ratio was 8.4 to 1. The first harmonic at 2.68KHz was clearly visible in the spectral response in Figure 5.22. The second and third harmonics, at 4.02KHz and 5.36KHz, were also visible in the spectral response.

110

Figure 5.21. 3ms of measured relative displacement and velocity data for V_d=3.4008V.
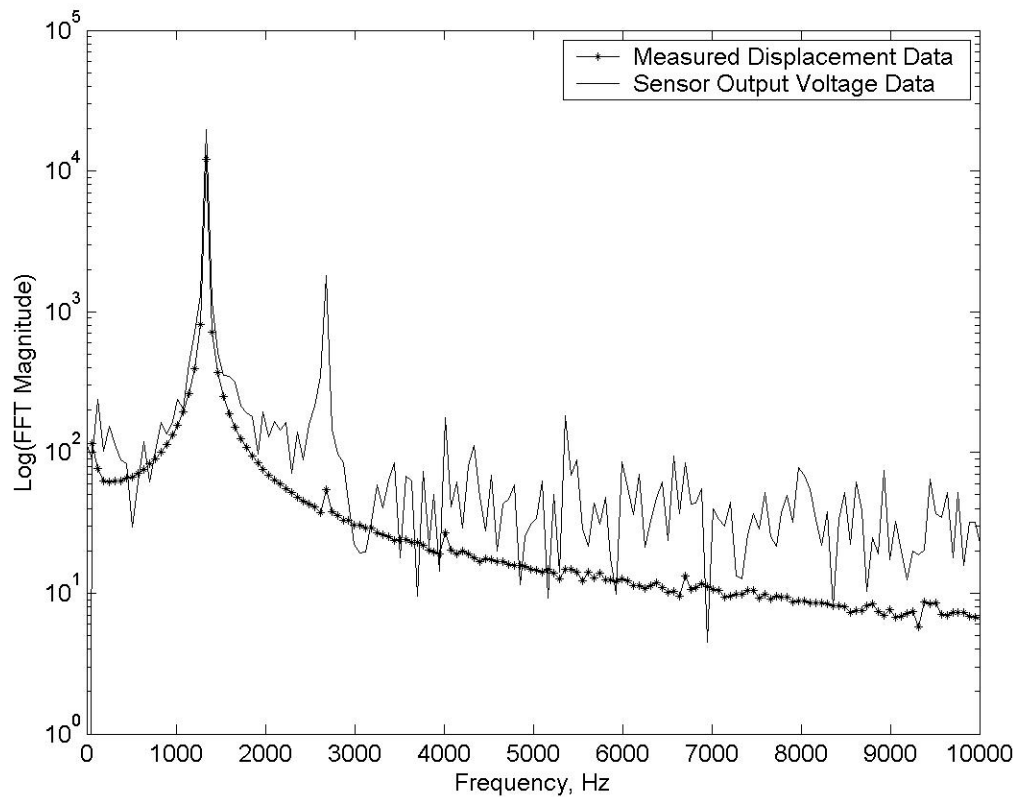
Figure 5.22. Spectral response of the relative displacement and velocity data for V_d=3.4008V.

5.7 Velocity Sensor Prototype Swept Frequency Testing

For this test, a series of runs were performed to evaluate the performance of the prototype relative velocity sensor as the shaker frequency was varied between 700Hz and 1.7KHz in 100Hz intervals, while operating the shaker at the same power level. This frequency spacing conveniently missed the peak resonant frequency of the device and allowed the evaluation at relatively low x_o/x_A ratios. The purpose of this test was to evaluate the linearity of the prototype relative velocity sensor's output voltage with

regard to excitation frequency, since (3.2) predicted a linear relationship. For this test, the shaker amplifier was set on a relatively high, however uncalibrated, setting and the amplifier controller was set on 3.001V so that the electromechancial shaker would produce a large motion close to its maximum capability at each frequency. Figures 5.23 through 5.43 present plots of the measured time responses for the first 3ms of recorded data for the measured relative displacement and the corresponding output voltage from the relative velocity sensor, and 2048 point FFT generated spectral responses of the measured data, for each run except for the 1.5KHz run. Unfortunately, 1.5KHz was close enough to the sensor mechanical resonant frequency that the large signal saturated the third amplifier stage in the interface circuit and severely distorted the output voltage, as shown in the time trace in Figure 5.39. Therefore the data from this run was not used in evaluating the sensor. The data from some of the runs performed during this test had significant low frequency components resulting from the sensor and the measurement system detecting low frequency mechanical noise that was present in the laboratory during the time that this test took place. However, the low frequency noise had no impact on the test itself. A typical frequency response of the background vibration noise components present in the measurement laboratory between DC and 200Hz was measured using one of the Polytec OFV 353 laser interferometric displacement measurement systems and is presented in Appendix E.
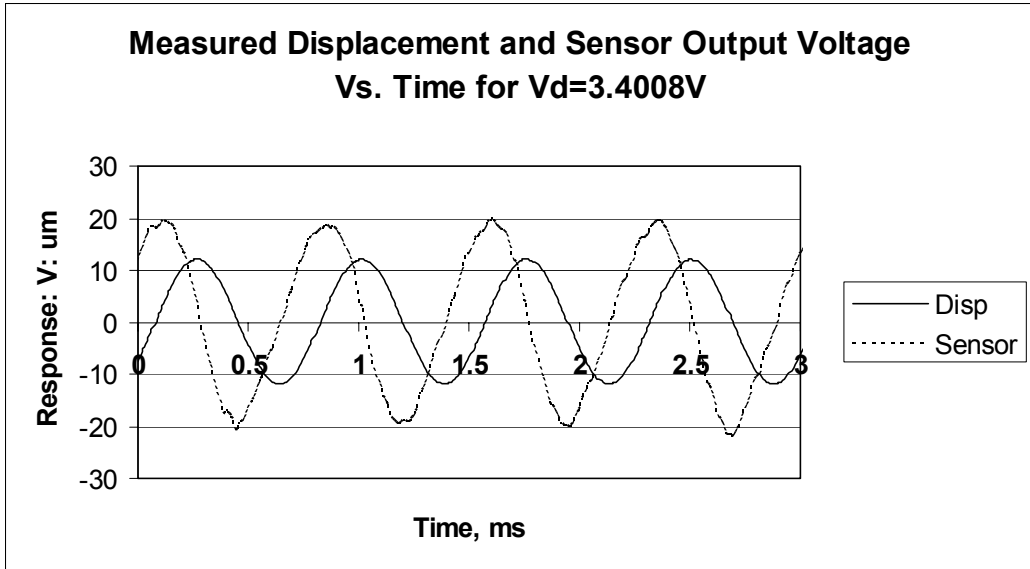
Figure 5.23. 3ms of measured relative displacement and velocity data for the 700Hz run.

Figure 5.24. Spectral response of the relative displacement and velocity data for the 700Hz run.

114

Measured Displacement and Sensor Output Voltage Vs. Time for Vd=3.001V and Fd=800Hz

Figure 5.25. 3ms of measured relative displacement and velocity data for the 800Hz run.

Figure 5.26. Spectral response of the relative displacement and velocity data for the 800Hz run.

Figure 5.27. 3ms of measured relative displacement and velocity data for the 900Hz run.

Figure 5.28. Spectral response of the relative displacement and velocity data for the 900Hz run.

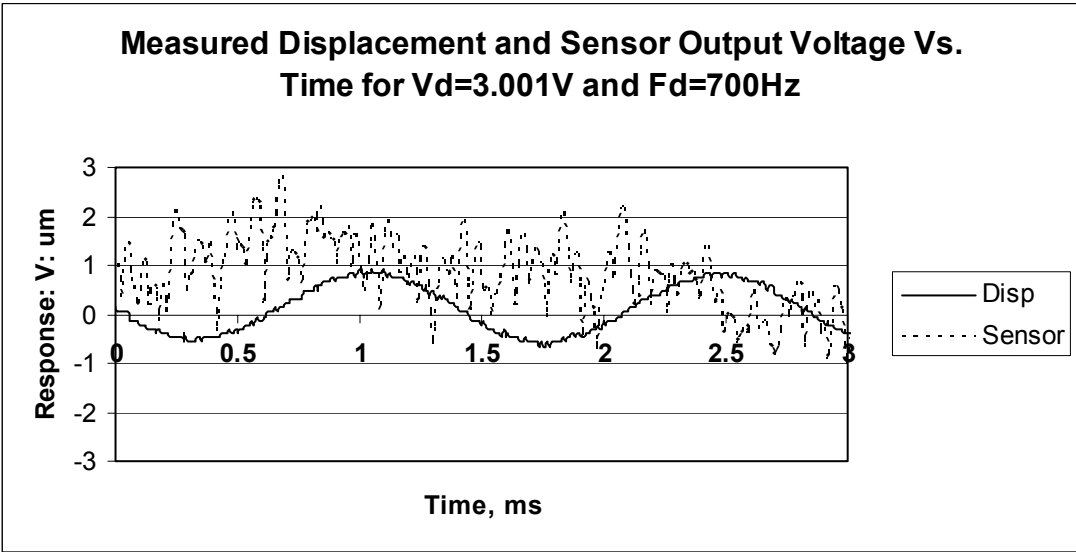**Measured Displacement and Sensor Output Voltage Vs. Time for Vd=3.001V and Fd=1KHz**

Figure 5.29. 3ms of measured relative displacement and velocity data for the 1KHz run.

Figure 5.30. Spectral response of the relative displacement and velocity data for the 1KHz run.

117

Measured Displacement and Sensor Output Voltage Vs. Time for Vd=3.001V and Fd=1.1KHz

Figure 5.31. 3ms of measured relative displacement and velocity data for the 1.1KHz run.

Figure 5.32. Spectral response of the relative displacement and velocity data for the 1.1KHz run.

118
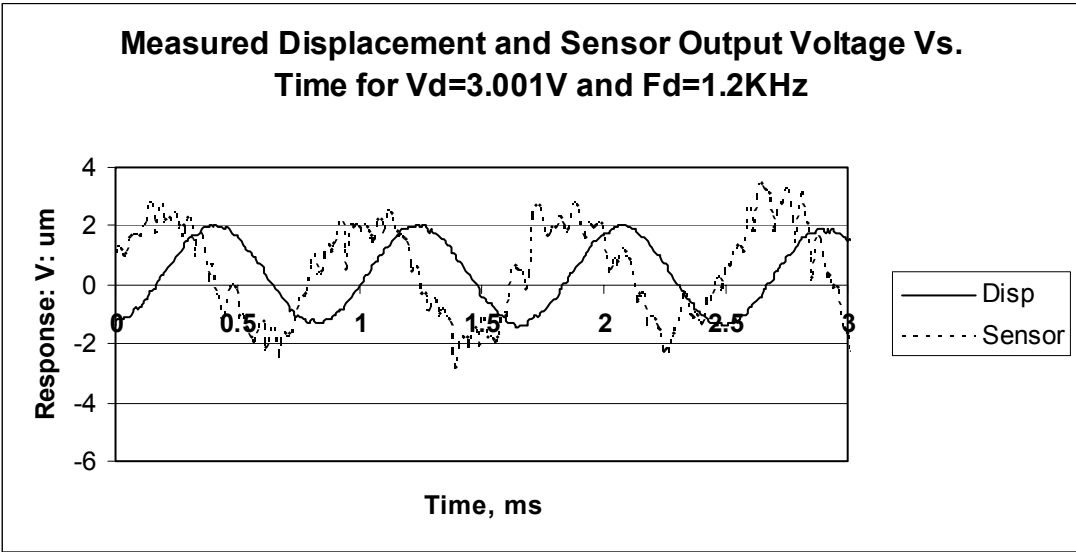
Figure 5.33. 3ms of measured relative displacement and velocity data for the 1.2KHz run.
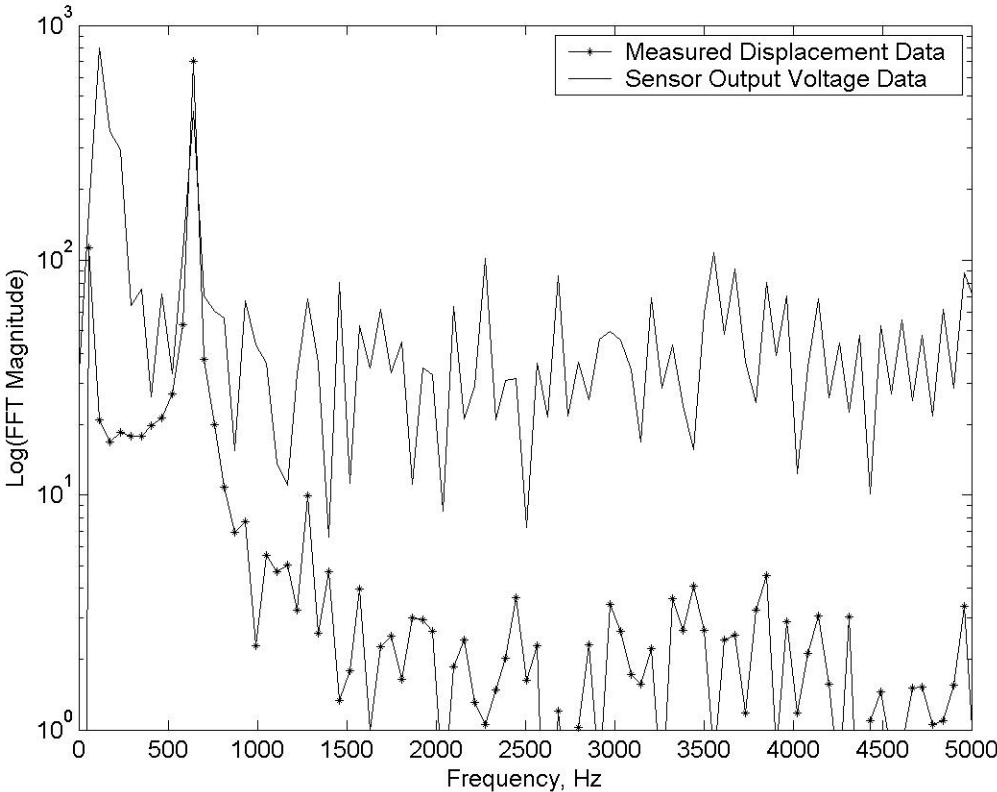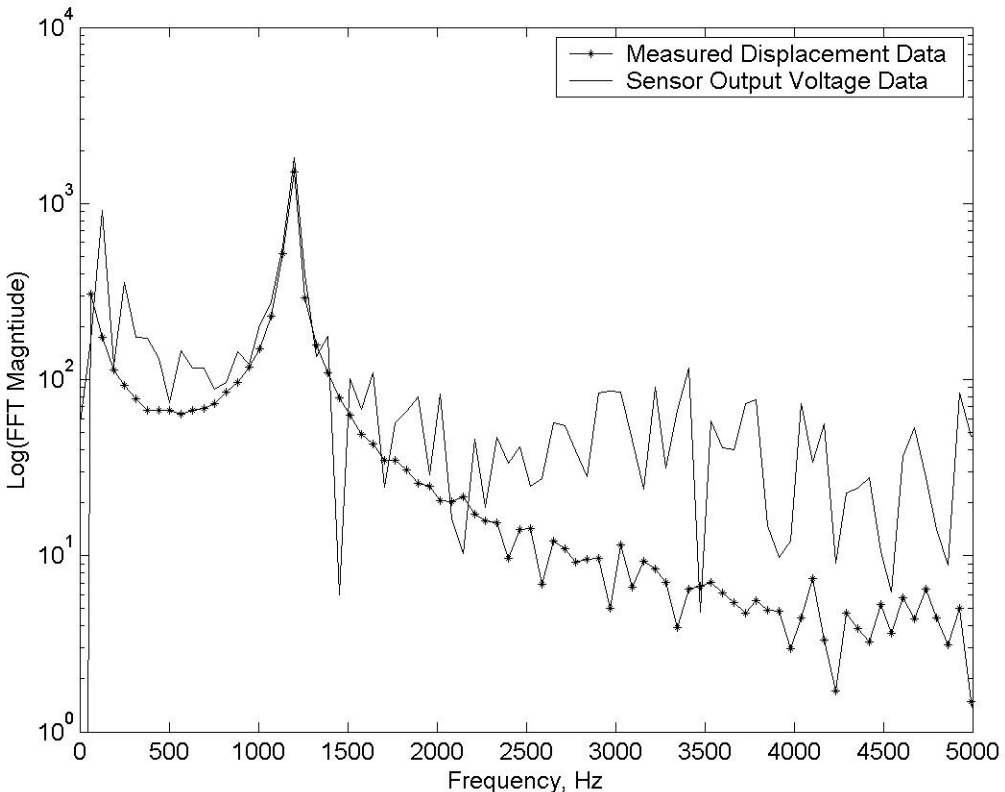

Figure 5.34. Spectral response of the relative displacement and velocity data for the 1.2KHz run.
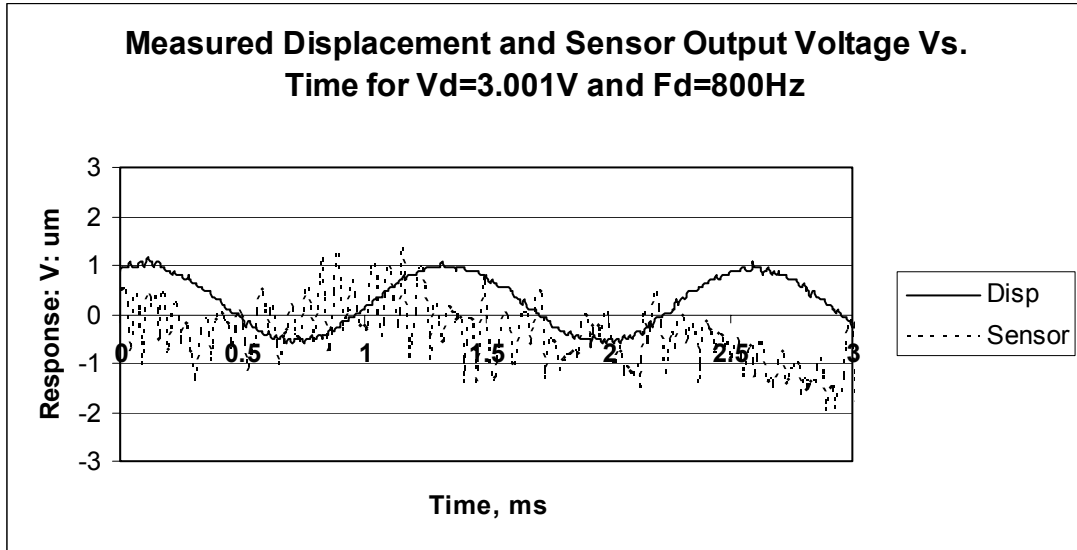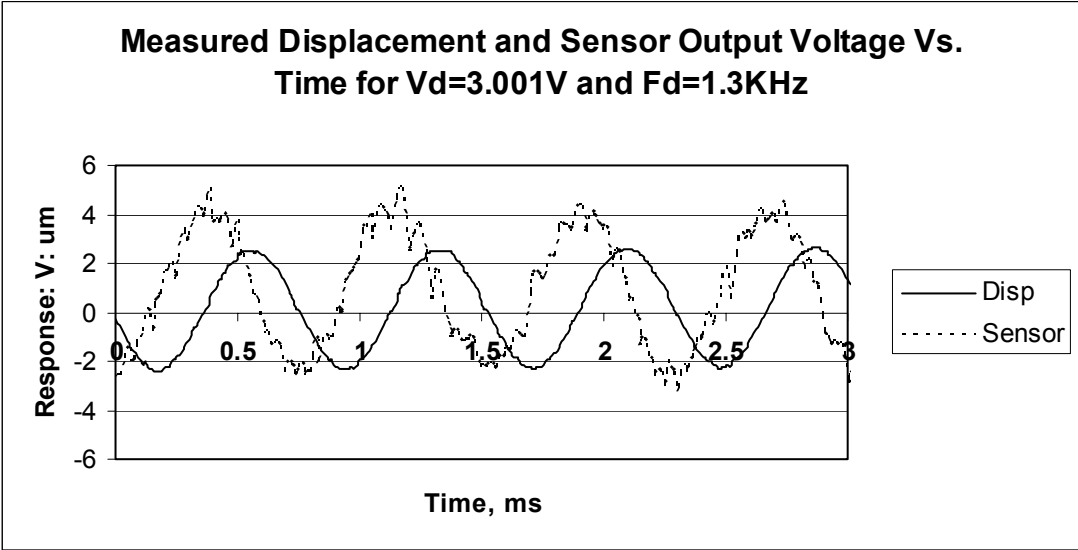
Figure 5.35. 3ms of measured relative displacement and velocity data for the 1.3KHz run.
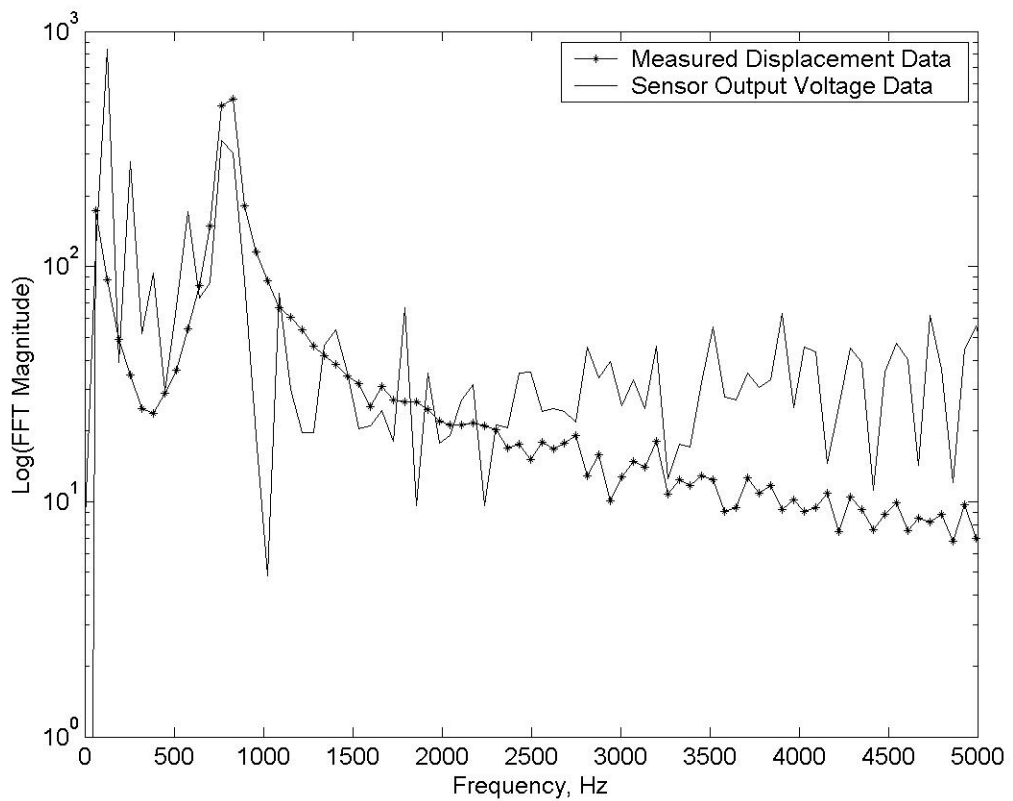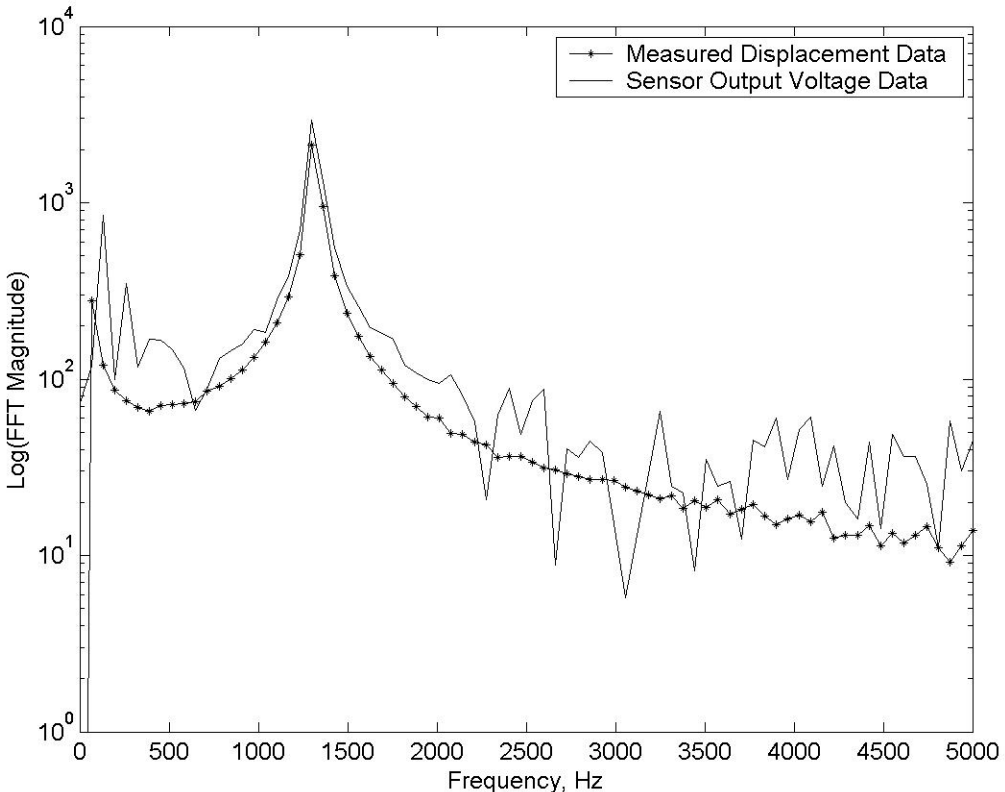

Figure 5.36. Spectral response of the relative displacement and velocity data for the 1.3KHz run.

120
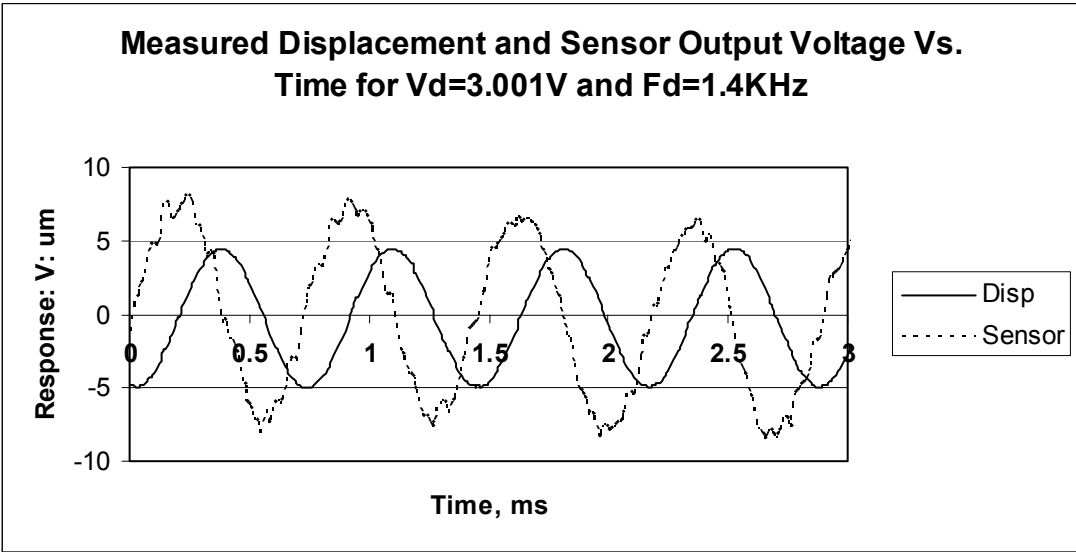
Figure 5.37. 3ms of measured relative displacement and velocity data for the 1.4KHz run.
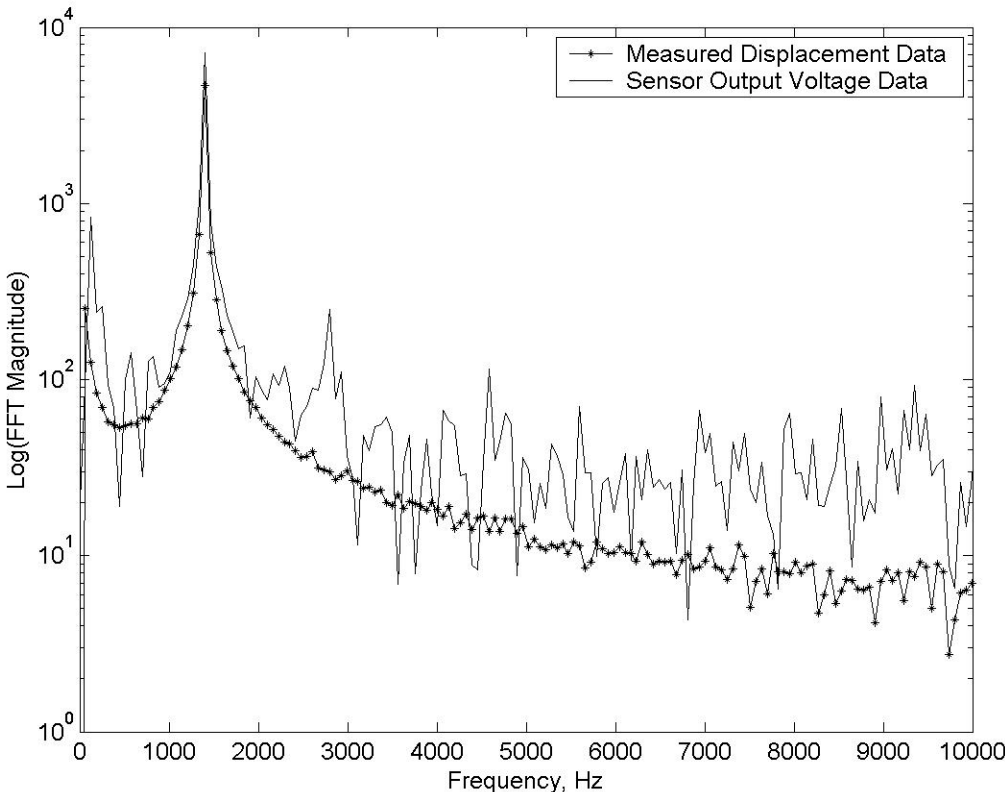
Figure 5.38. Spectral response of the relative displacement and velocity data for the 1.4KHz run.

121
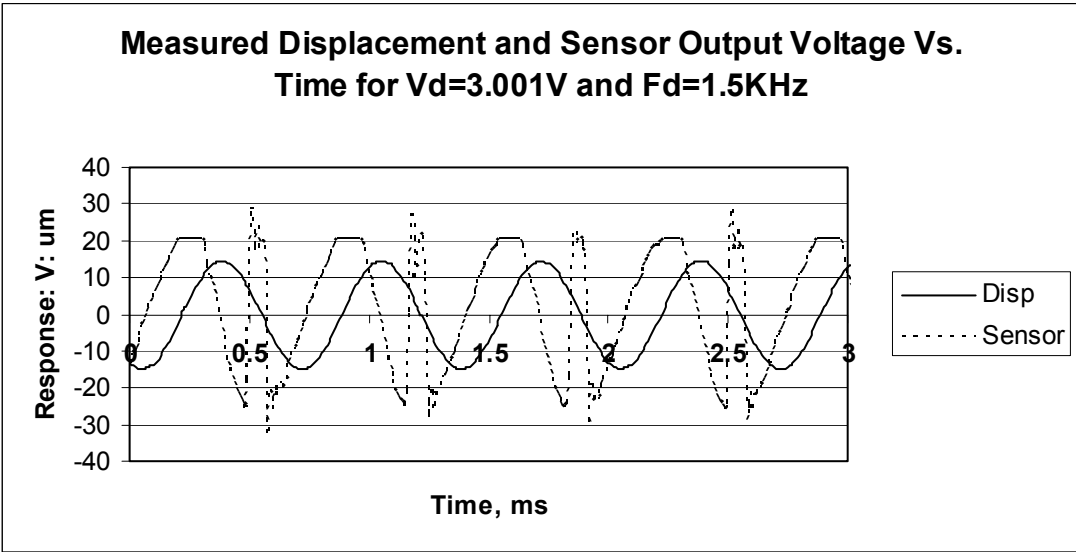
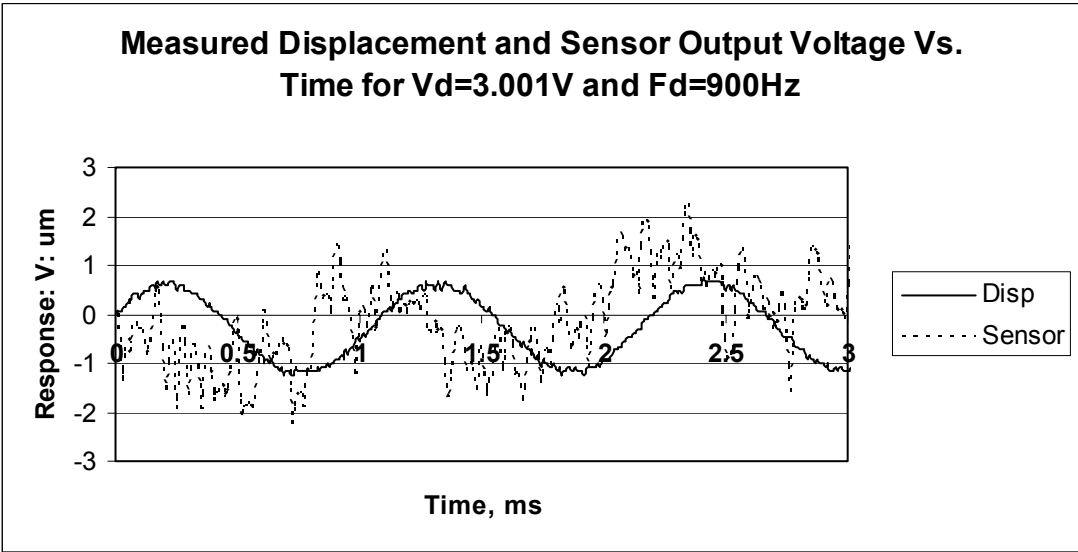Figure 5.39. 3ms of measured relative displacement and velocity data for the 1.5KHz run.

Figure 5.40. 3ms of measured relative displacement and velocity data for the 1.6KHz run.
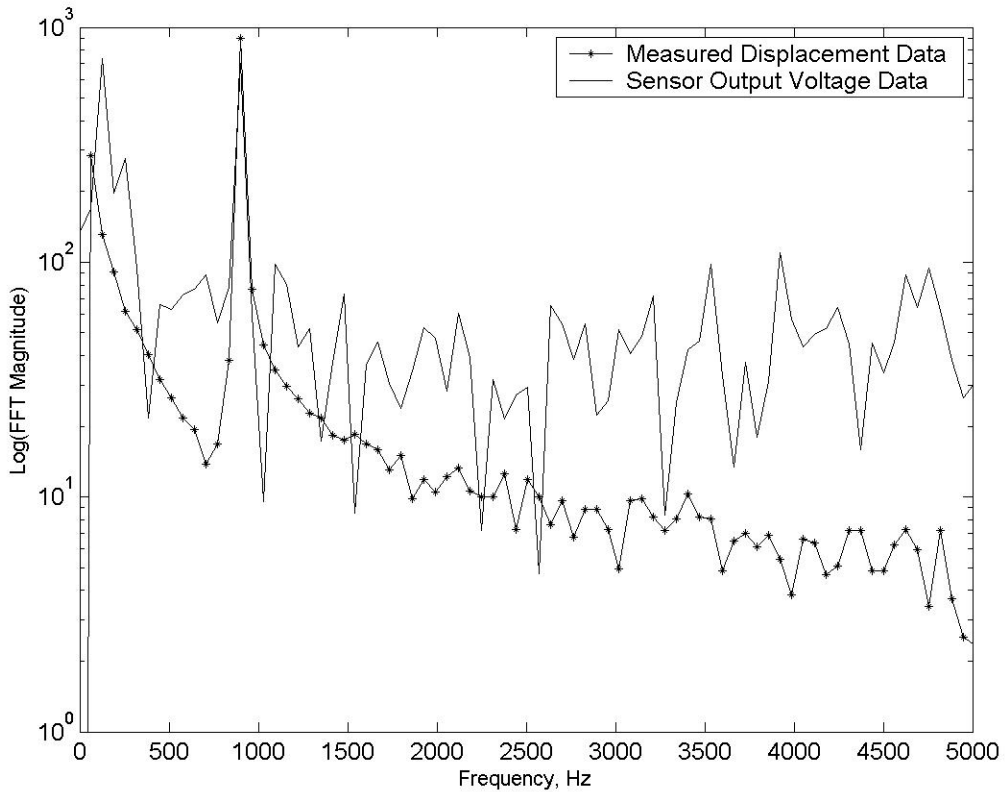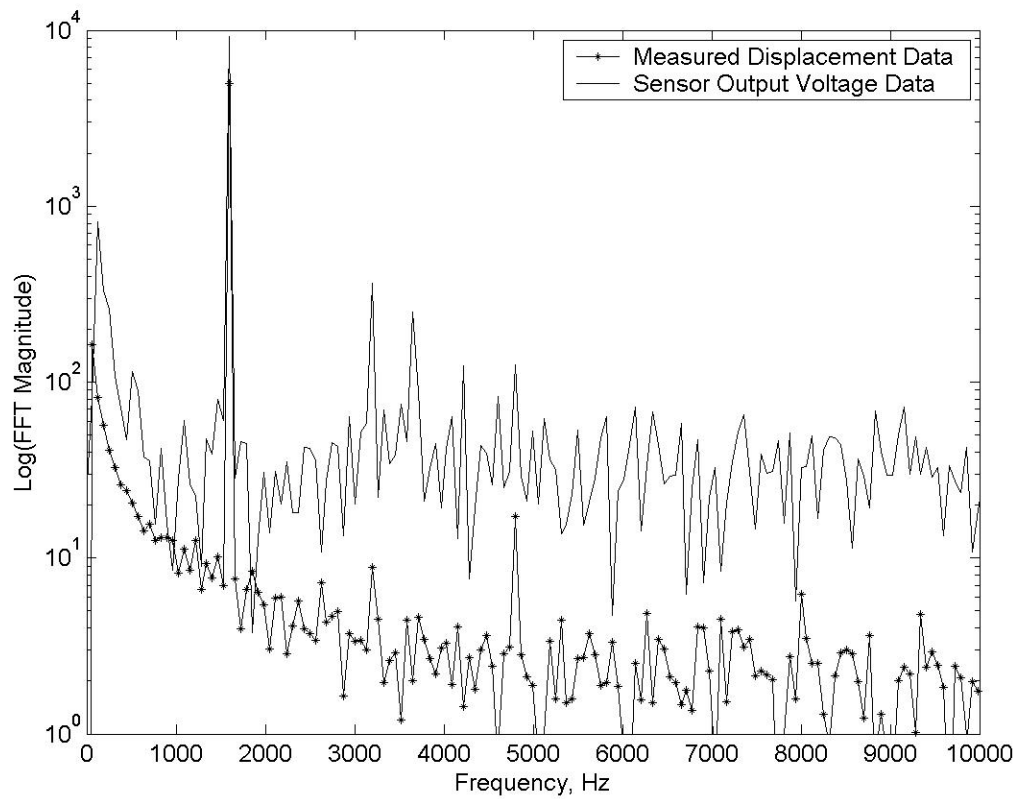
Figure 5.41. Spectral response of the relative displacement and velocity data for the 1.6KHz run.
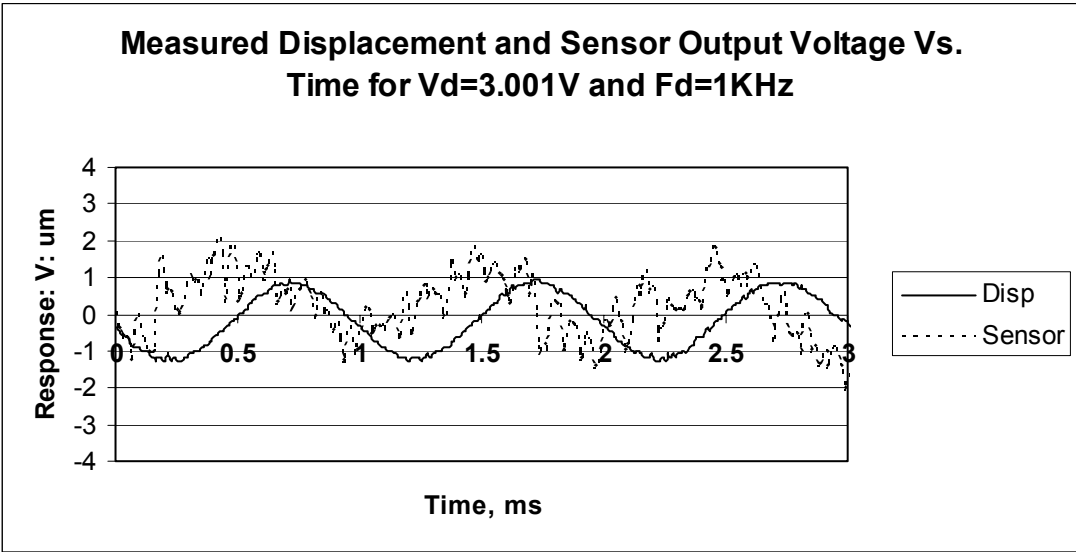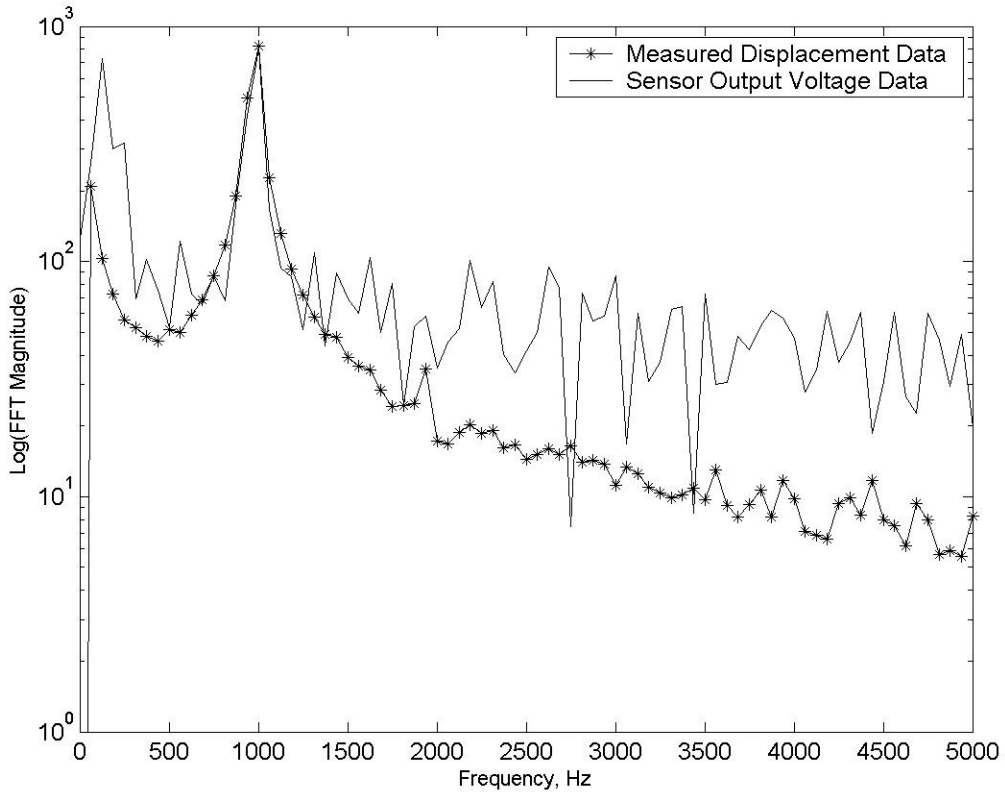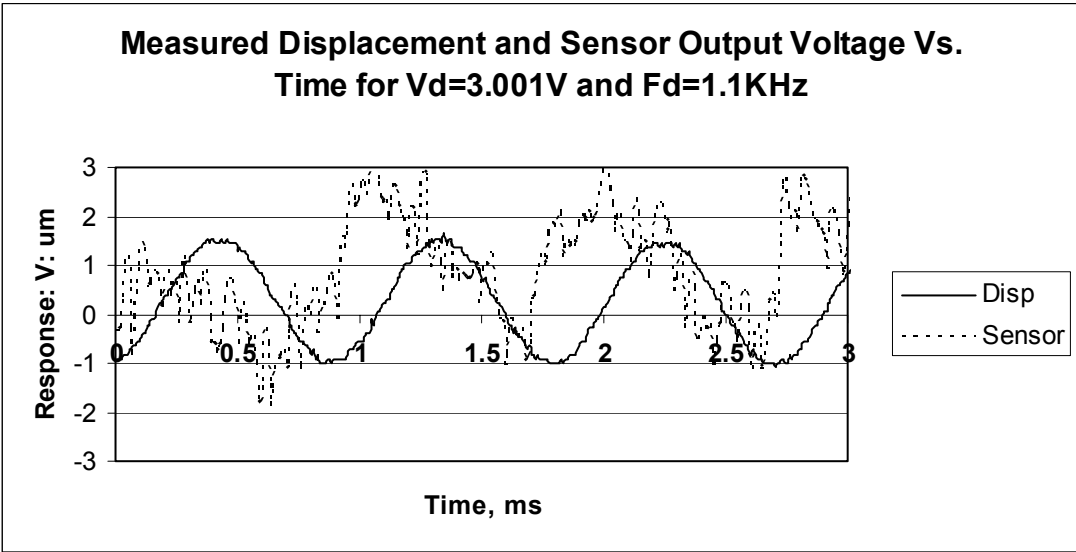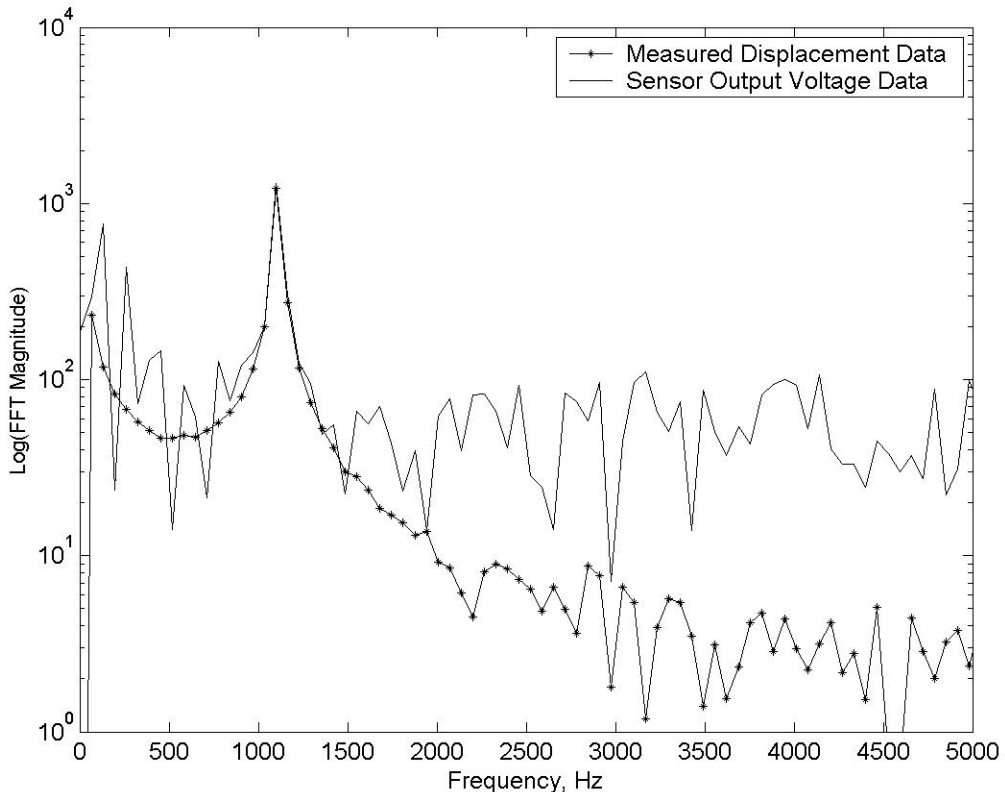

Figure 5.42. 3ms of measured relative displacement and velocity data for the 1.7KHz run.
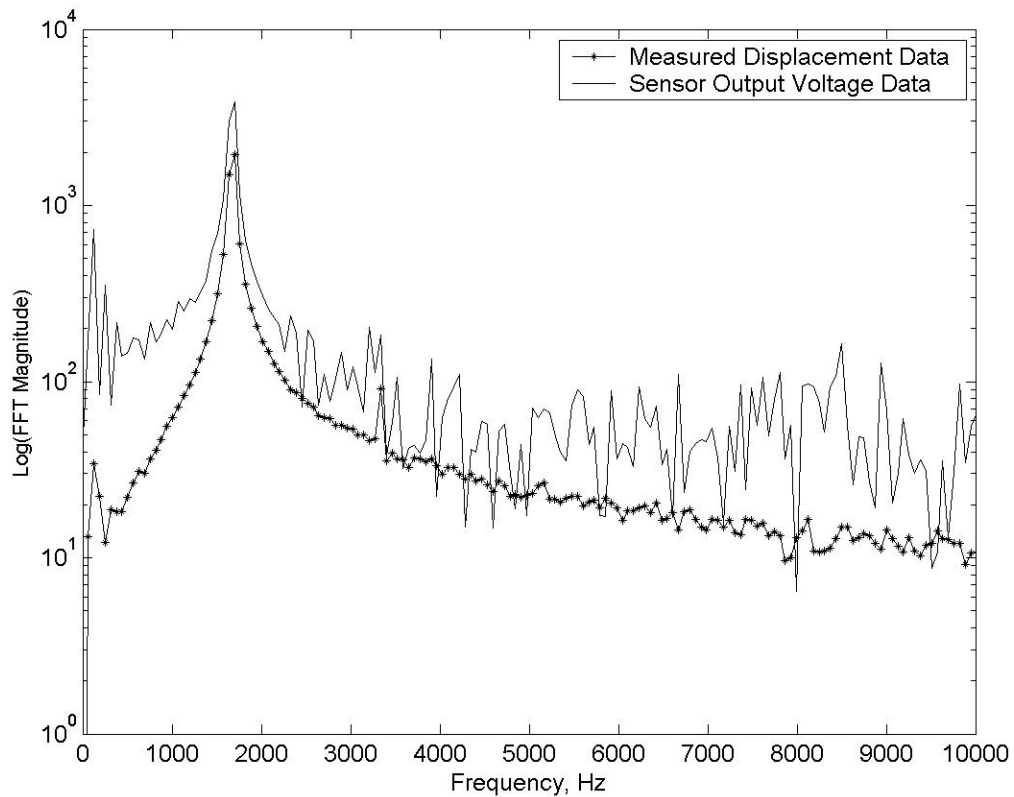
Figure 5.43. Spectral response of the relative displacement and velocity data for the 1.7KHz run.

The spectral responses were used to obtain the amplitude values for the measured electrode displacement and sensor output voltage for each case. Then a normalized output voltage with respect to a 1μm electrode displacement was computed for each case by dividing the sensor output voltage amplitude by the electrode displacement amplitude. Figure 5.45 presents a plot of the normalized sensor output voltage amplitudes versus shaker excitation frequency. Using (4.3) with V_b equal to 25V and x_A equal to 1μm, a MATLAB simulation was performed to record 1024 time samples of simulated sensor responses at each test frequency. Then the simulated output voltage time traces were

added together and a 1024 point FFT was performed on the data. Summing the signals together allowed the spectral responses to be easily presented on one graph. The calculated spectral response of the simulated sensors' output signals are presented in Figure 5.44, showing the linear increase in amplitude with increasing frequency. The simulated amplitudes were then calculated, by dividing the
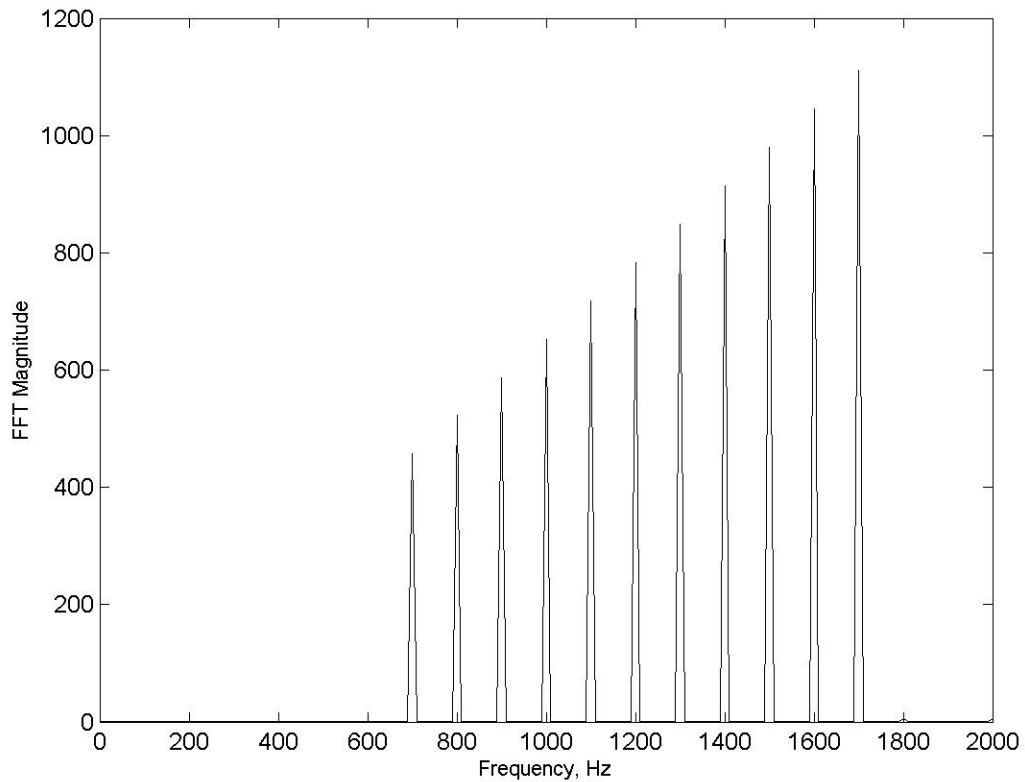
Figure 5.44. Spectral response of the simulated sensor over the frequency range of interest.

1024 point FFT peak values by 512, and plotted in Figure 5.45 with the normalized amplitudes computed from the test data for comparison. Both the normalized amplitudes generated from measured test data and the amplitudes generated by simulation produced

125

similar responses. The main difference between the two plots was an offset between them, which can be attributed to errors in the measurement of the test data. Since the slope of each line is proportional to a number of constants, such as x_A, V_b, R_b, etc…, the difference in the slopes of two plots of data is attributed to the differences in these constants between the fabricated prototype sensor and the modeled sensor. The nearly linear response of the prototype sensor closely matches the theoretical sensor response.
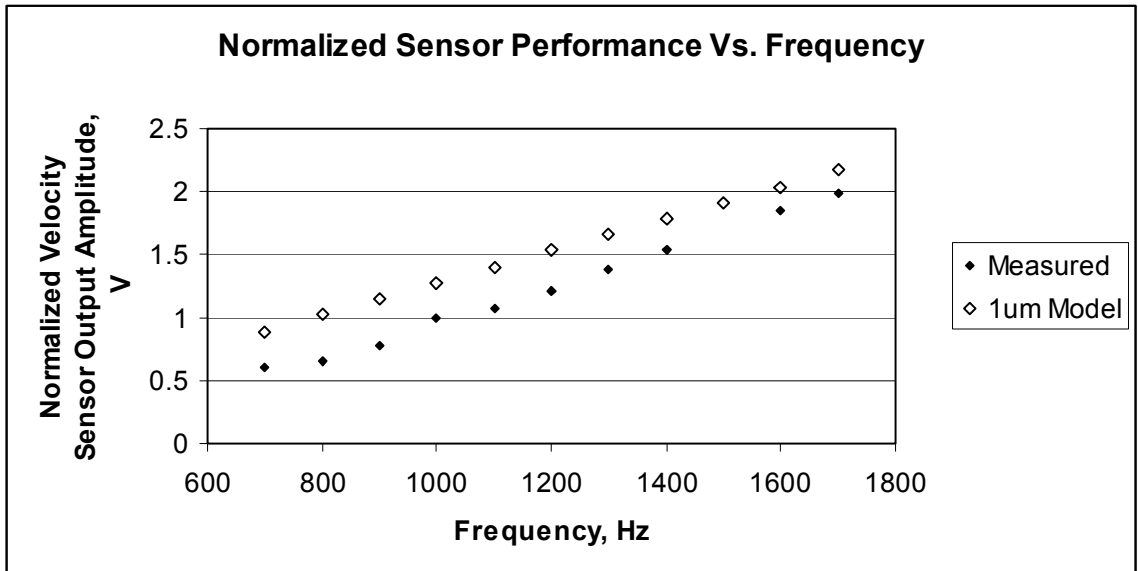
Figure 5.45. A plot of the normalized sensor output amplitudes for the measured data and the simulated data as a function of excitation frequency.

5.8 Velocity Sensor Prototype Nonlinear Distortion Testing

The purpose of this test was to excite the prototype velocity sensor near its resonant frequency with a large displacement to evaluate the harmonics produced from

the nonlinear characteristics of the sensor. For this test, the prototype relative velocity sensor was powered with ±40V DC power supplies. The excitation was increased to a high level close to but not at the point of saturating the third stage amplifier in the interface electronics. Figures 5.46 and 5.47 present the time trace data and spectral responses for the measured displacement and sensor output voltage data collected during this test. The spectral response was calculated by performing a 1024 point FFT on the measured data.
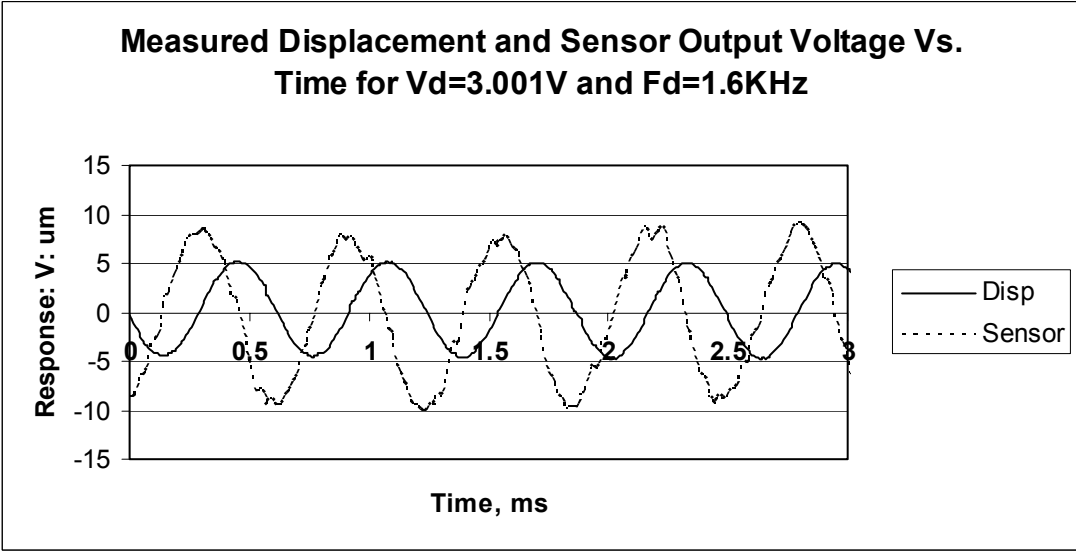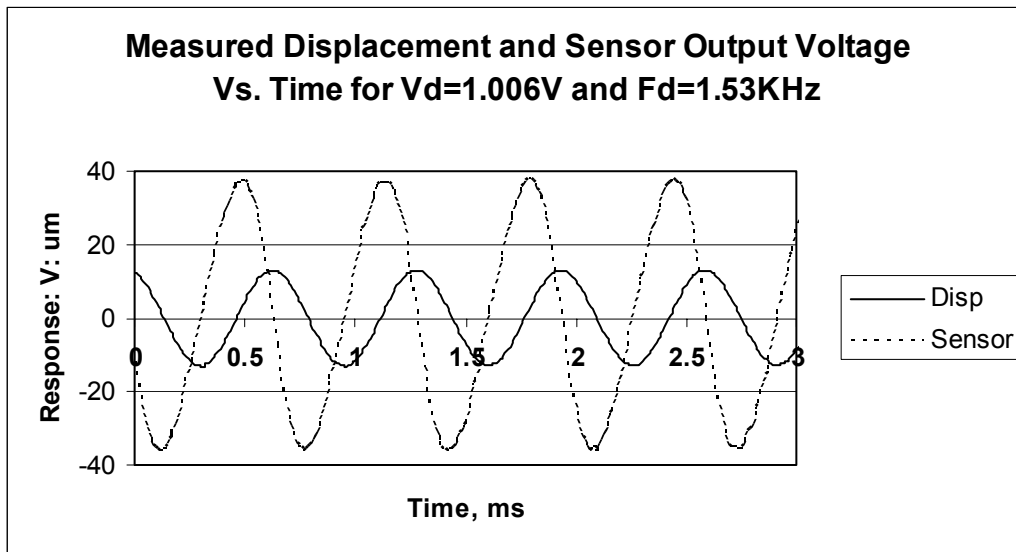

Figure 5.46. 3ms of measured relative displacement and velocity data.

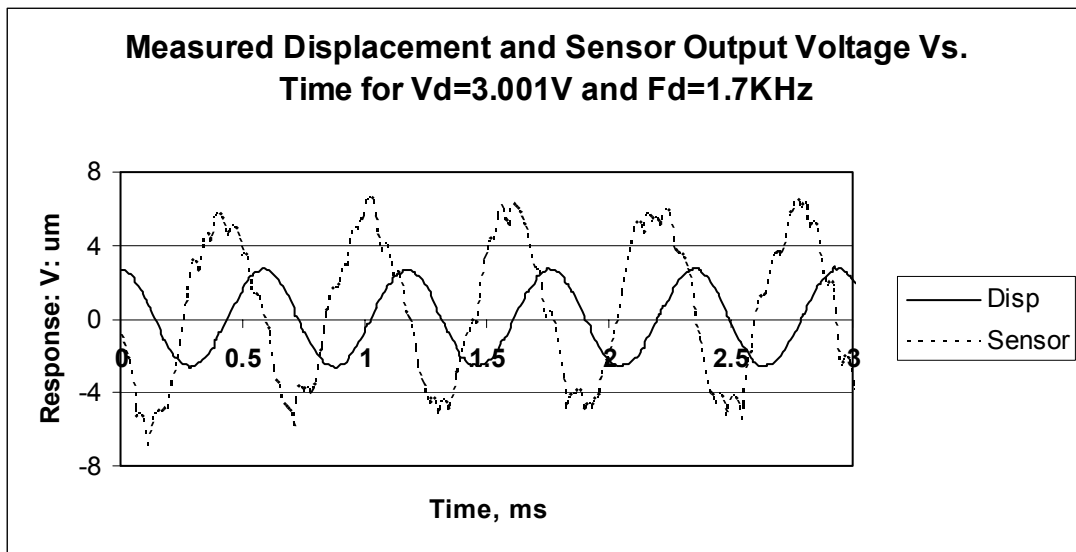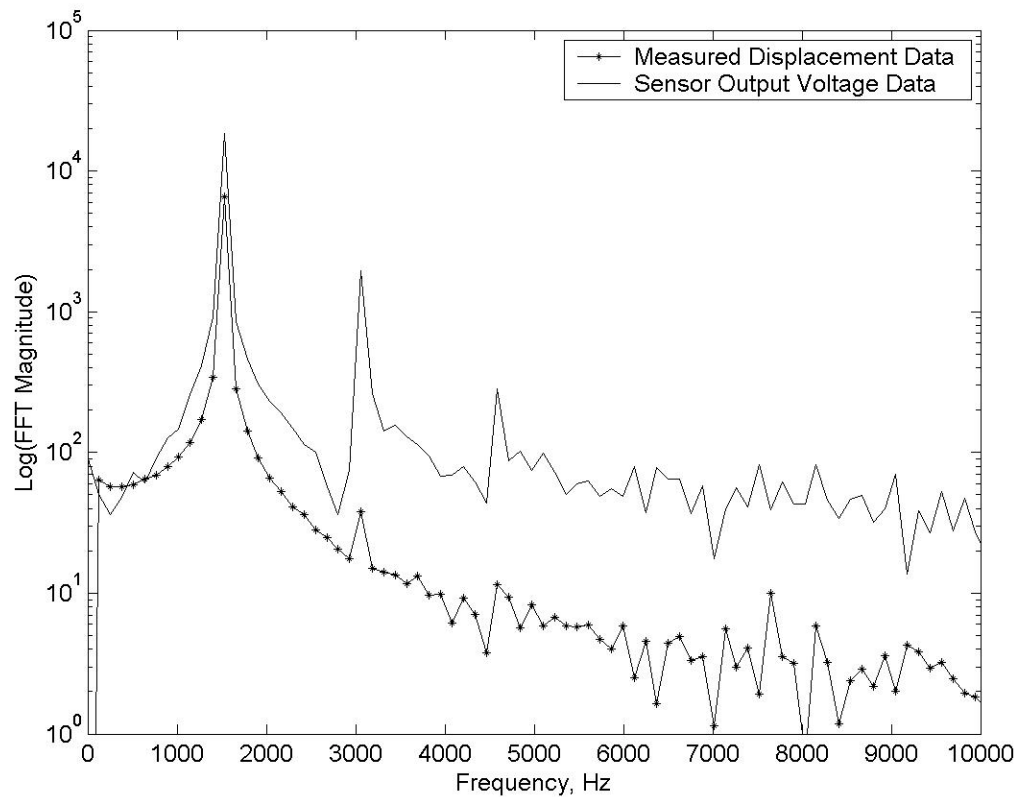Figure 5.47. Spectral response of the measured relative displacement and velocity data.

The spectral response of the measured displacement data was used to calculate the amplitude of the relative displacement experienced by the electrodes. The calculated amplitude of displacement was 12.89μm at 1.53KHz. Using (4.3) with a V_b of 40V, an excitation frequency of 1.53KHz and x_A equal to 12.89μm, a MATLAB simulation was performed to generate 2048 time samples of a simulated sensor response using a 97.65625μm time step. A spectral response was then calculated by performing a 2048 point FFT on the resulting data, and is presented in Figure 5.48.

128
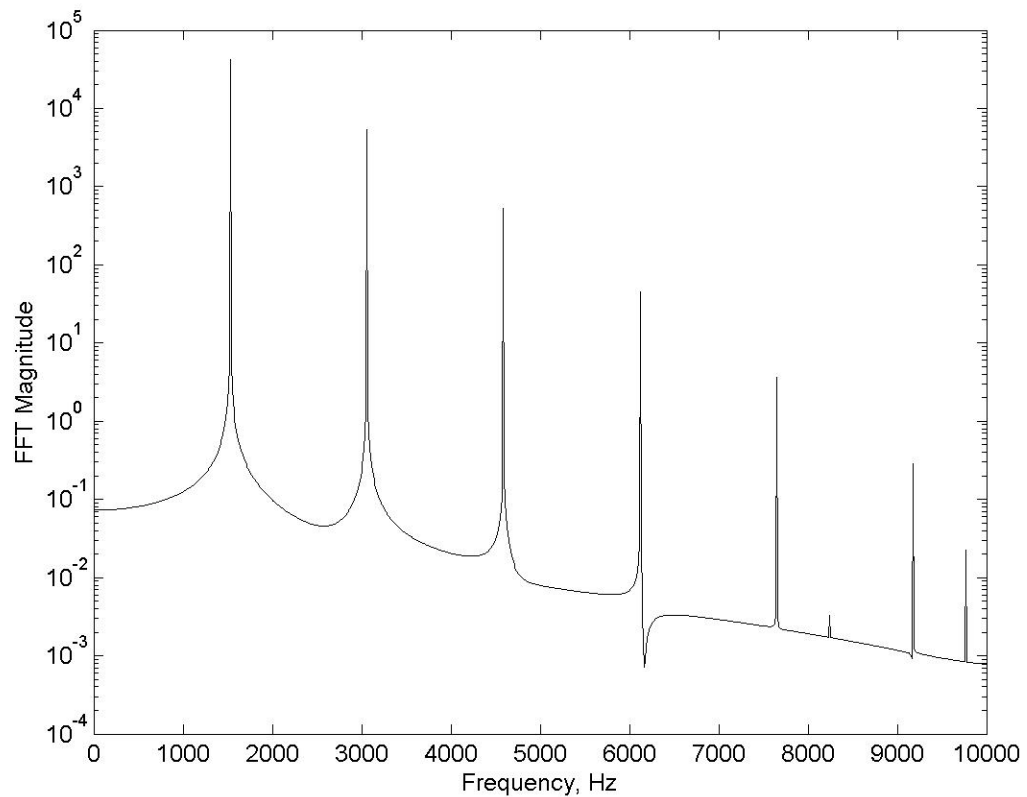
Figure 5.48. Spectral response of the simulated sensor velocity data.

The spectral responses of the measured velocity sensor output voltage data and the simulated velocity sensor output voltage data were used to obtain the amplitudes of the fundamental frequencies and the first two harmonics. These are presented in Table 5.1 with the ratios of the respective amplitudes of the fundamental frequencies to the amplitudes of the first two harmonics. The third harmonic and higher harmonics were not used because they were not clearly discernable in the spectral response of the measured test data. The comparison of the data from Table 5.1 and the spectral response plots, Figures 5.47 and 5.48, indicates that the measured sensor data and the simulated sensor data have the same form but differ in amplitude magnitudes. These differences

129

are primarily due to the prototype sensor having slightly different values for design constants, such as the rest gap distance, than were modeled in the simulated sensor. Also, the prototype sensor data was measured in the presence of noise and with instruments that may have introduced additional error. Additionally, observe that the measured relative displacement data has a component at approximately 3.06KHz, the same frequency as the first harmonic in the measured relative velocity data. During this test, the shaker was driven very hard in order to induce a large relative motion in the prototype sensor. It is likely that the shaker head was beginning to saturate from being driven so hard, which could result in the sinusoidal motion becoming distorted by introducing higher frequency components into the motion. Since the relative velocity sensor would respond to motion at 3.06KHz, this could partially explain why the ratio of the amplitude of the fundamental frequency component to the amplitude of the first harmonic frequency component from the measured sensor data was greater than the same ratio from the simulated sensor data. However, the prototype sensor data was reasonably close to the simulated sensor data in both form and magnitude such that it correlated well with the predicted model.

Component	Measured Data (V)	Simulated Data (V)	Percent Difference
Fundamental	36.278	40.747	10.97%
1st Harmonic	3.845	5.274	27.08%
2nd Harmonic	0.557	0.5119	-8.77%
Fundamental/1st Harmonic	9.434	7.727	-22.10%
Fundamental/2nd Harmonic	65.160	79.600	18.14%

Table 5.1. A comparison of the fundamental and first two harmonic frequency amplitudes

for the measured sensor data and the simulated sensor data.

CHAPTER 6

CONCLUSIONS

By reexamining the technique presented by Senturia [9] for measuring the relative

velocity between two electrodes in motion such that $\partial C/\partial x$ is constant, a technique was

developed for measuring the relative velocity between two parallel plate electrodes that

experience translational motion normal to their opposing faces such that $\partial C/\partial x$ is not

constant. For the two electrode relative velocity sensor, the nonlinearities resulting from

$\partial C/\partial x$ not being constant produce distortion in the sensor output signal resulting from the

presence of high frequency components at multiples of the relative velocity fundamental

frequency. The amount of distortion in the sensor output signal from the nonlinearities

inherent in the sensor can be quantified by examining the THD of the theoretical sensor

output as a function of the ratio of the rest gap distance, x_o, to the amplitude of the

relative electrode motion, x_A, and the THD increases as the ratio of x_o/x_A decreases. The

THD estimate can be used to determine the minimum x_o/x_A ratio that can be tolerated for

a particular application in order to maintain a minimum level of quality in the relative

velocity measurement. The relative velocity sensor's output signal, at the times during

each sinusoidal velocity cycle where the velocity changes direction, does not deviate

from the response of an ideal relative velocity sensor as the ratio of x_o/x_A varies.

Therefore the two electrode relative velocity sensor performs best as a relative

132

velocity direction sensor, where the polarity of the output signal from the sensor indicates the direction of relative velocity between the two electrodes. In addition to the distortion that corrupts the relative velocity measurements for small ratios of x_o/x_A, the sensor output voltage will spike negative and then positive during the second half of each velocity cycle. Therefore if the sensor is utilized to detect the direction of relative velocity for small ratios of x_o/x_A, the sensor interface circuit must be designed to handle the resulting voltage spikes in order to avoid amplifier saturation, which will further distort the signal and possibly corrupt the otherwise accurate information about when the relative velocity changes direction. Since the current flowing through the relative velocity sense capacitor can be very small, on the order of a few nA, the sensor interface electronics must be carefully designed so that the noise floor is low enough compared to the sensor output current in order to obtain a sufficiently large SNR in the sensor output signal for the application.

A prototype two electrode relative velocity sensor and interface circuit were designed, fabricated and evaluated. An electromechanical shaker was used to induce sinusoidal relative motion into sensor while the electrode relative displacement and the sensor output voltage were captured. The test data was compared with data generated from simulating the theoretical model for the relative velocity sensor, revealing a close correlation between the prototype sensor and the sensor model. Discrepancies between the test data and the sensor model were explained.

CHAPTER 7

RECOMMENDATIONS FOR FUTURE WORK

Although this investigation verified the developed technique for measuring relative velocity between two electrodes in motion normal to their opposing faces, through external excitation using an electromechanical shaker, the prototype sensor and the shaker itself limited the testing to about 20% of the rest gap distance. This limitation was partially due to the range of motion that the shaker was capable of producing at the resonant frequency of the sensor. It was also due to the fragility of the micromachined spring-mass-damper structure. At least one device broke during external excitation with the shaker while trying to achieve a large range of relative displacement between the electrodes. The optimal method for extending the relative range of electrode displacement would be to fabricate a new prototype sensor with a smaller rest gap, preferable 25μm or less. This could be accomplished by realizing the entire sense capacitor as a micromachined device. Additionally, if the interface electronics were integrated into a single integrated circuit die, it could be directly attached to the micromachined sense capacitor. This configuration might lower the noise floor and thereby increase the sensitivity of the relative velocity sensor. Additionally, it would useful to perform shaker testing over a range of temperatures in order to more fully characterize the prototype relative velocity sensor.

Under this investigation, only an external source was used to produce relative motion between the two electrodes for the relative velocity sensor to measure. This motion was limited to small amplitudes except near the sensor's resonant frequency. However, if a PPA were integrated into the prototype micromachined sensor structure, it could produce a relatively large amplitude of motion at a selectable frequency over a much wider bandwidth, and thereby allow greater evaluation of the relative velocity sensor.

The theoretical development and prototyping of the relative velocity sensor concept showed that the harmonics produced by the nonlinear characteristics of the relative velocity sensor occur at multiples of the excitation frequency. Therefore if the highest frequency of relative motion experienced by two microstructures in a common device was limited to less than twice the lowest frequency of relative motion, then the harmonics produced by the sensor nonlinearities could be attenuated by adding a low pass filter to the sensor interface circuit. This should be investigated.

A relative velocity sensor using a three electrode differential architecture was theorized in this investigation that should have a more symmetrical response than the two electrode relative velocity sensor that was prototyped and evaluated. This device has not been constructed and tested. Therefore prototyping and evaluating the device would be worthwhile.

Several techniques were described in Chapter 2 for measuring the relative displacement between two or more electrodes. It would be useful to integrate the relative velocity sensor with a relative displacement sensor to measure both states between

microstructures. This would be useful for implementing a variety of control laws if integrated with one or more MEMS actuators.

A number of active vibration isolation systems rely on velocity feedback or at least utilize the direction of velocity between moving structures to modify the mechanical damping between the structures. Since the technique for measuring relative velocity developed through this investigation is particularly suitable for measuring the direction of relative velocity between two micromachined electrodes, it would be worthwhile to integrate the technique into a micromachined active vibration isolation system.

BIBLIOGRAPHY

[1] S. Marco, J. Samitier, O. Ruiz, A. Herms and J. R. Morante, "Analysis of electrostatic-damped piezoresistive silicon accelerometers," *J. Sensors and Actuators A*, vol. 37-38, 1993, pp. 317-322.

[2] P. K. C. Wang, "Feedback control of vibrations in a micromachined cantilever beam with electrostatic actuators, *J. Sound and Vibration*, vol. 213(3), 1998, pp. 537-550.

[3] D. H. S. Maithripala, J. M. Berg and W. P. Dayawansa, "Control of an electrostatic MEMS using static and dynamic output feedback," *ASME J. of Dynamical Systems Measurement and Control*, vol. 127, 2005, pp. 443-450.

[4] D. H. S. Maithripala, J. M. Berg and W. P. Dayawansa, "A virtual velocity sensor for improved transient performance of electrostatically-actuated MEMS," *Proc. of 2003 IMECE*, Washington, DC, November 16-21, 2003.

[5] K. B. Lee and Y. H. Cho, "Electrostatic control of mechanical quality factors for surface-micromachined lateral resonators," *J. Micromech. Microeng.*, vol. 6, 1996, pp. 426-430.

[6] R. P. van Kampen, M. J. Vellekoop, P. M. Sarro and R. F. Wolffenbuttel, "Application of electrostatic feedback to critical damping of an integrated silicon capacitive accelerometer," *J. Sensors and Actuators A*, vol. 43, 1994, pp. 100-106.

[7] C. T.-C. Nguyen and R. T. Howe, "Quality factor control for micromechanical resonators," *International Electron Devices Meeting,* Technical Digest, San Francisco, CA, Dec. 13-16, 1992, pp. 505-508.

[8] Y. Liu, T. P. Waters, M. J. Brennan, "A comparison of semi-active damping control strategies for vibration isolation of harmonic disturbances", *J. of Sound and Vibration*, vol. 280, 2005, pp. 21-39.

[9] S. D. Senturia, *Microsystem Design*. Boston, MA: Kluwer Academic Publishers, 2001, pp. 502-503.

[10] J. D. Kraus, *Electromagnetics*. New York: McGraw-Hill Book Company, 1984, pp. 69-70.

[11] M. –H. Bao, *Handbook of Sensors and Actuators, Volume 8, Micro Mechanical Transducers, Pressure Sensors, Accelerometers and Gyroscopes.* S. Middelhoek, Ed. New York: Elsevier Science B. V., 2000, pp. 140-142, 158-159.

[12] J. I. Seeger and S. B. Crary, "Stabilization of electrostatically actuated mechanical devices," *Proc. of Transducers'97*, vol. 2, Chicago, IL, June 16-19, 1997, pp. 1133-1136.

[13] E. K. Chan and R. W. Dutton, "Electrostatic micromechanical actuator with extended range of travel," *J. Microelectromechanical Systems*, vol. 9, No. 3, Sept. 2000, pp. 321-328.

[14] M. H. Miller, J. A. Perrault, g. G. Parker, B. P. Bettig and T. G. Bifano, "Simple models for piston-type micromirror behavior," *J. Micromech. Microeng*, vol. 16, 2006, pp. 303-313.

[15] J. Q. Mou, Y. Lu, J. P. Yang, Q. H. Li and G. X. Guo, "Design, fabrication and characterization of single crystal silicon microactuator for hard disk drives," *J. Micromech. Microeng.*, vol. 14, 2004, pp. 1608-1613.

[16] S. Kim, Y. Yee, J. Choi, H. Kwon, M. Ha, C. Oh and J. U. Bu, "Integrated mems optical flying head with lens positioning actuator for small form factor optical data storage," *J. Sensors and Actuators A*, vol. 114, 2004, pp. 429-437.

[17] R. Dean, G. Flowers, N. Sanders, K. MacAllister, R. Horvath, A. S. Hodel, W. Johnson, M. Kranz and M. Whitley, "Active micromachined vibration isolation filters using electrostatic actuation to enhance packaging for mechanically harsh environments," *proc. IMAPS International Conference and Exhibition on Device Packaging*, Scottsdale, AZ, March 13-16, 2005, CD-only.

[18] K. Jono, M. Hashimoto, M. Esashi, "Electrostatic servo system for multi-axis accelerometers," *Proc. IEEE Workshop on Micro Electro Mechanical Systems*, Oiso, Japan, Jan. 25-28, 1994, pp. 251-256.

[19] P. B. Chu and K. S. J. Pister, "Analysis of closed-loop control of parallel-plate electrostatic microgrippers," *Proc. 1994 IEEE Int. Conf on Robotics and Automation*, vol. 1, San Diego, CA, May 8-13, 1994, pp. 820-825.

[20] F. Han, Z. Gao, Y. Wang, "A differential capacitance to voltage converter for electrostatic levitation applications," *J. Sensors and Actuators A*, vol. 99, 2002, pp.249-255.

[21] A. Dec and K. Suyama, "Micromachined electro-mechanically tunable capacitors and their applications to RF IC's," *IEEE. Trans. on Microwave Theory and Techniques*, vol. 46, No, 12, Dec. 1998, pp. 2587-2596.

[22] R. Ramadoss, S. Lee, Y. C. Lee, V. M. Bright and K. C. Gupta, "Fabrication, assembly and testing of RF MEMS capacitive switches using flexible printed circuit technology," *IEEE Trans. Adv. Packaging*, vol. 26, No. 3, Aug. 2003, pp. 248-254.

[23] W. Huang and G. Lu, "Analysis of lateral instability of in-plane comb drive MEMS actuators based on a two-dimensional model," *J. Sensors and Actuators A*, vol. 113, 2004, pp. 78-85.

[24] J. D. Grade, K. y. Yasumara, H. Jerman, "Advanced, vibration-resistant, comb-drive actuators for use in a tunable laser source," *J. Sensors and Actuators A*, vol. 114, 2004, pp. 413-422.

[25] J. M.-L. Tsai, H.-Y. Chu, and W. Fang, "The BELST II process for a silicon high-aspect-ratio micromachining vertical comb actuator and its applications," *J. Micromech Microeng.* vol. 14, 2004, pp. 235-241.

[26] B. D. Jensen, S. Mutlu, S. Miller, K. Kurabayashi and J. J. Allen, "Shaped comb fingers for tailored electromechanical restoring force," *J. Microelectromechanical Systems*, vol. 12, No. 3, June 2003, pp. 373-383.

[27] J. D. Grade, H. Jerman and T. W. Kenny, "Design of large deflection electrostatic actuators," *J. Microelectromechanical Systems*, vol. 12, No. 3, June 2003, pp. 335-343.

[28] W. C. Tang, T.-C. H. Nguyen, M. W. Judy and R. T. Howe, "Electrostatic-comb drive of lateral polysilicon resonators," *J. Sensors and Actuators*, vol. A21-A23, 1990, pp. 328-331.

[29] E. J. Garcia and J. J. Sniegowski, "Surface micromachined microengine," *J. Sensors and Actuators A*, vol. 48 1995, pp. 203-214.

[30] Z. f. Wang, W. Cao, X. C. Shan, J. F. Xu, S. P. Lim, W. Noell and N. F. de Rooij, "Development of 1x4 MEMS-based optical switch," *J. Sensors and Actuators A*, vol. 114, 2004, pp. 80-87.

[31] H. D. Nguyen, D. Hah, P. R. Patterson, R. Chao, W. Piyawattanametha, E. K. Lau and M. C. Wu, "Angular vertical comb-driven tunable capacitor with high-tuning capabilities," *J. Microelectromechanical Systems*, vol. 13, No. 3, June 2004, pp. 406-413.

[32] M. Kranz, S. Burgett, T. Hudson, M. Buncick, P. Ruffin, P. Ashley and J. McKee, "A wide dynamic range silicon-on-insulator MEMS gyroscope with digital force feedback," *Proceedings of the 12th International Conference on Solid State Sensors*, Actuators and Microsystems, Boston, June 8-12, 2003, pp. 159-162.

[33] A. Duwel, J. Gorman, M. Weinstein, J. Borenstein and P. Ward, "Experimental study of thermoelastic damping in MEMS gyros," *J. Sensors and Actuators A*, vol. 103, 2003, pp. 70-75.

[34] T.-R. Hsu, *MEMS & Microsystems Design and Manufacture*. New York: McGraw Hill, 2002, pp. 121-124.

[35] L. Meirovitch, *Elements of Vibration Analysis*. New York: McGraw-Hill Book Company, 1986, pp. 63-65.

[36] G. T. A. Kovacs, *Micromachined Transducers Sourcebook*. New York: WCB/McGraw-Hill, 1998, pp. 211-215.

[37] R. Dean, J. Pack, N. Sanders, P. Reiner, "Micromachined LCP for Packaging MEMS Sensors," IEEE IECON 2005 Conference, Raleigh, NC, Nov. 6-10, 2005.

[38] B. Borovic, A. Q. Liu, D. Popa, H. Cai and F. L. Lewis, "Open-loop versus closed-loop control of MEMS devices: choices and issues," *J. Micromech. Microeng.*, vol. 15, 2005, pp. 1917-1924.

[39] L. K. Baxter, *Capacitive Sensors*. New York: IEEE Press, 1997, pp. 51-52.

[40] R. A. Gayakwad, *Op-Amps and Linear Integrated Circuits, Second Edition*. Englewood Cliffs, New Jersey: Prentice Hall, 1988, p. 129.

[41] P. E. Allen, *Switched Capacitor Circuits*. New York: Van Nostrand Reinhold Company, 1984, pp. 39-126.

[42] C. Lu, M. Lemkin and B. E. Boser, "A monolithic surface micromachined accelerometer with digital output," *IEEE J. Solid State Circuits*, vol. 30, NO. 12, December 1995, pp. 1367-1373.

[43] M. V. Paemel, "Interface circuit for capacitive accelerometer," *J. Sensors and Actuators*, vol. 17, 1989, pp. 629-637.

[44] R. P. van Kampen, M. J. Vellekoop, P. M. Sarro and R. F. Wolfenbuttel, "Application of electrostatic feedback to critical damping of an integrated silicon capacitive accelerometer," *J. Sensors and Actuators A*, vol. 43, 1994, pp. 100-106.

[45] M. Kraft, C. Lewis, T. Hesketh and S. Szymkowiak, "A novel micromachined accelerometer capacitive interface," *J. Sensors and Actuators A*, vol. 68, 1998, pp. 466-473.

[46] H. Toshiyoshi, M. Mita and H. Fujita, "A MEMS piggyback actuator for hard-disk drives," *J. Microelectromechanical Systems*, vol. 11, No. 6, December 2002, pp. 648-654.

[47] R. Dean, G. Flowers, R. Horvath, N. Sanders, S. Hodel, J. Hung and T. Roppel, "A Relative Velocity Sensor for Improved Electrostatic Parallel Plate Actuator Control," IEEE Sensors Journal, paper submitted for review Nov. 7, 2005.

[48] R. Dean, G. Flowers, S. Hodel, K. MacAllister, R. Horvath, A. Matras, G. Robertson and R. Glover, "Vibration Isolation of MEMS Sensors for Aerospace Applications," *Proceedings of the IMAPS International Conference and Exhibition on Advanced Packaging and Systems*, Reno, NV, March 10-13, 2002, pp. 166-170.

[49] "OPA445 High Voltage FET-Input Operational Amplifier," Device Data Sheet, Texas Instruments Inc., Dallas, TX, 2003.

[50] J. Bryant and L. Counts, "OP-AMP ISSUES-NOISE," Ask the Application Engineer -7, Analog Devices Inc., www.analog.com/library/analogDialogue/Anniversary/7.html.

[51] J. Bryant, "OP-AMP ISSUES," Ask the Application Engineer -8, Analog Devices Inc., www.analog.com/library/analogDialogue/Anniversary/8.html.

[52] R. E. Best, *Phase-Locked Loops, Theory, Design and Applications*, New York: McGraw-Hill, 1993, p. 50.

APPENDICES

APPENDIX A

MATLAB M-file for THD Calculation:

```
%THD analysis 1/18/06 on 2 electrode velocity sensor

clear all;

format compact;

format long;

c=2*3.14159/1024

wt=0

ratio=1.1

xo=1e-5

xa=xo/ratio

K=xo^2/xa

for i=1:1024,

    y(i)=K*xa*cos(wt)/(xo+xa*sin(wt))^2

    z(i)=cos(wt)

    t(i)=i

    f(i)=wt

    wt=wt+c

end
```

```
p=fft(y,1024)

plot(t,y,t,z)

Vu=0

for i=3:1:512

    Vu=Vu+(abs(p(i)))^2

end

THD=(Vu^.5)/abs(p(2))

end
```

Detailed Microfabrication Process Flow

Device 3 Process Traveler

350um DSP Si wafer fabrication approach

I.   **Wafer Clean**

1) 50:1 H_2O:HF at ambient for 30s

2) 6:1:1 H_2O:HCL:H_2O_2 at 80°C for 10min

3) DI water rinse and blow dry

II.   **Oxidation**

1) Push in at 900C

2) Ramp to 1050C

3) N2 - 5 minutes

4) O2 - 5 minutes

5) O2, H2 - 1 hour

6) O2 - 5 minutes

7) N2 - 5 minutes

8) Ramp down to 900C and pull out

III.   **Top Side Photolithography**

1) 3min O2 clean in Matrix

2) 15min vapor phase HMDS deposition at ambient

3) PR spin: Clarient 5214E, 1000RPM, 30s

4) Softbake: 108°C for 2min on hotplate

5) MABA6: 6s exposure with photoplot "Pas Top 11/12/04"

6) Develop: Clarient AZ 400K, 2:1, 30s

7) DI water rinse and blow dry

IV. Top Side Dry Oxide Etch

1) RIE (350W), CF4 & CHF3, 5 to 7min

2) Inspect

3) Continue until complete

V. Condition STS ASE

VI. Top Side DRIE

1) 40um Si etch in STS ASE

2) Inspect often

3) As close to 40um as possible

VII. Top Side Photoresist Strip

1) 5min O2 clean in Matrix (500W, 5Torr)

VIII. Bottom Side Photolithography

1) 3min O2 clean in Matrix

2) 15min vapor phase HMDS deposition at ambient

3) PR spin: 1045, 1000RPM, 30s

4) Softbake: 108°C for 2min on hotplate

5) MABA6: 30s exposure with photoplot "Pas Bot 11/12/04"

6) Develop: Clarient AZ 400K, 2:1, 30s

7) DI water rinse and blow dry

8) Hardbake: 120°C for 2min on hotplate

9) DI water rinse and blow dry

IX. **BOE**

1) 3min BOE dip

2) Inspect

3) Continue until complete

4) DI water rinse

5) Blow dry

X. **Condition STS ASE**

XI. **Bottom Side DRIE 1**

1) ~100um Si etch in STS ASE

XII. **Cleave Wafer**

1) Carefully fracture wafer to separate the 7 die

XIII. **Die Mount 1**

1) Using a test wafer: 3min O2 clean in Matrix

2) Test wafer: 15min vapor phase HMDS deposition at ambient

3) Test wafer: PR spin: Clarient 5214E, 3000RPM, 30s

4) Hardbake: 120°C for 2min on hotplate

5) Set an individual dice onto test wafer in the center, bottom side up

6) Paint a small drop of Clarient 5214E photoresist onto each corner of the dice -

mounting wafer interface.

7) Softbake: 108°C for 10min on hotplate

XIV. Bottom Side DRIE 2

1) ~210um Si etch in STS ASE

2) Etch until part released

3) Check often to prevent over etching

XV. Post DRIE Clean

1) Dip into acetone bath to remove dice from mounting wafer

2) DI water bath

3) Air dry (do not blow dry)

4) 5min O2 clean in Matrix (500W, 5Torr) bottom side

5) 5min O2 clean in Matrix (500W, 5Torr) top side

XVI. E-Beam Metallization

1) 2min Ar ion clean

2) 800A Ti

3) 2000A Au

APPENDIX C

PSPICE Input File for Simulating the Velocity Sensor Interface Electronics

* NSF OP445 test circuit

* Robert Dean

* July 5, 2005

Vdd 10 0 DC 25

Vss 11 0 DC -25

X1 0 1 10 11 2 OPA445

X2 3 4 10 11 5 OPA445

X3 0 7 10 11 8 OPA445

Cs 10 1 4pF

Cx 10 13 20pF

C1 3 0 5.6n

C2 5 6 4.7u

R1 1 2 100K

R2 2 3 1k

R3 4 0 1K

R4 4 5 100K

R5 6 7 1K

R6 7 8 100K

R8 1 0 10k

* model for velocity capacitor current:

Rs 100 1 1000k

Is 0 100 AC 10e-9

*Is 0 100 sin(.000001 110n 1000)

*

* CONNECTIONS: NON-INVERTING INPUT

* | INVERTING INPUT

* | | POSITIVE POWER SUPPLY

* | | | NEGATIVE POWER SUPPLY

* | | | | OUTPUT

* | | | | |

.SUBCKT OPA445   1 2 3 4 5

*

C1   11 12 5.252E-12

C2   6 7 15.00E-12

DC   5 53 DX

DE   54 5 DX

DLP 90 91 DX

DLN 92 90 DX

DP   4 3 DX

EGND 99 0 POLY(2) (3,0) (4,0) 0 .5 .5

FB   7 99 POLY(5) VB VC VE VLP VLN 0 37.74E6 -40E6 40E6 40E6 -40E6

GA   6 0 11 12 188.5E-6

GCM   0 6 10 99 3.352E-9

ISS   3 10 DC 202.5E-6

HLIM 90 0 VLIM 1K

J1   11 2 10 JX

J2   12 1 10 JX

R2   6 9 100.0E3

RD1   4 11 5.305E3

RD2   4 12 5.305E3

RO1   8 5 25

RO2   7 99 25

RP   3 4 21.05E3

RSS 10 99 987.7E3

VB   9 0 DC 0

VC   3 53 DC 5

VE   54 4 DC 5

VLIM 7 8 DC 0

VLP 91 0 DC 26

VLN   0 92 DC 26

.MODEL DX D(IS=800.0E-18)

.MODEL JX PJF(IS=10.00E-12 BETA=87.73E-6 VTO=-1)
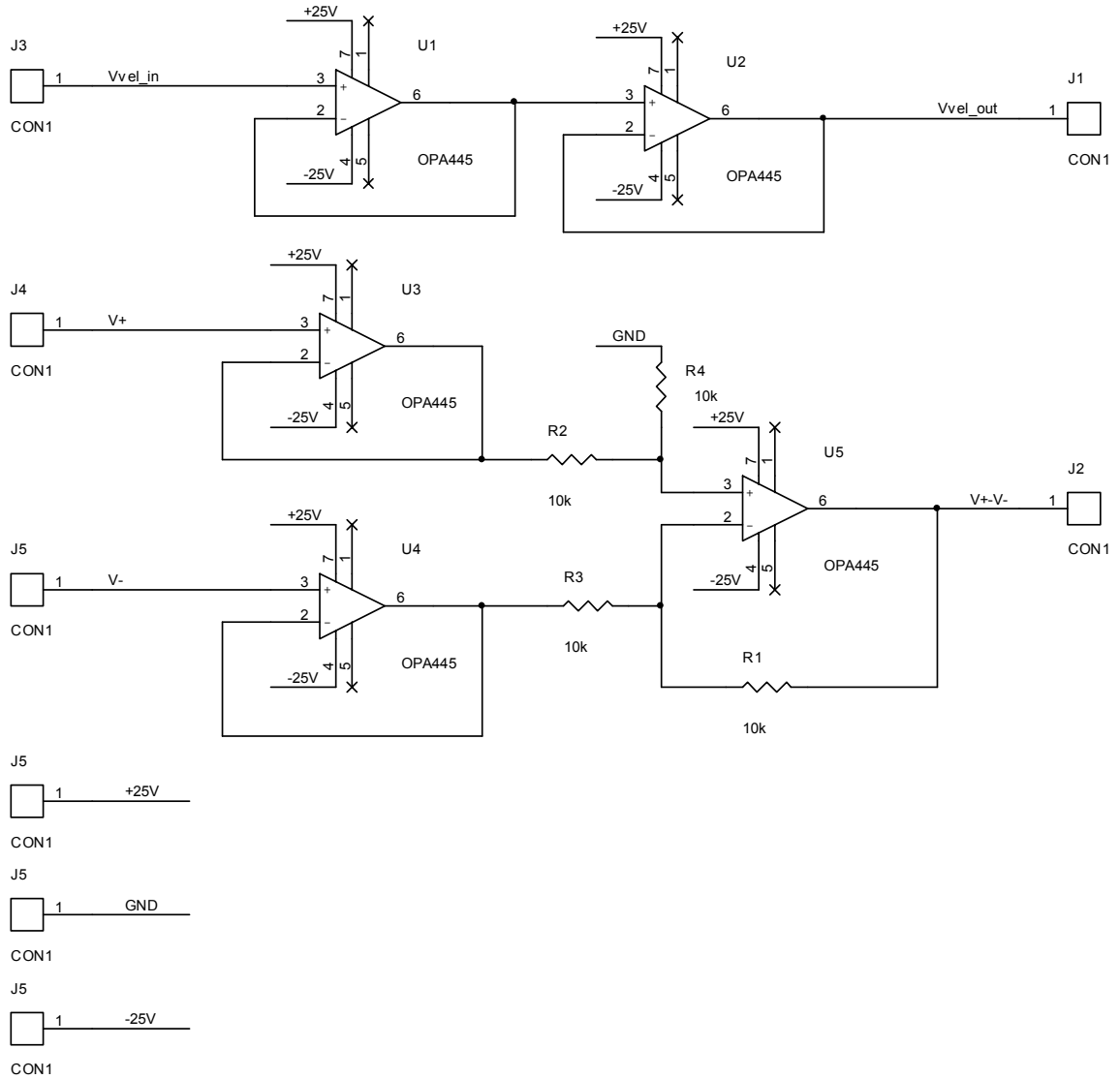
.ENDS

```
.AC DEC 100 1 1000000

*.TRAN 1U 1

.PROBE

.END
```

APPENDIX D

Schematic Drawing of the Difference Amplifier Circuit

APPENDIX E

A Typical Measured Frequency Response of Background Vibration Noise Present in

the Measurement Laboratory

Spectral Response of Low Frequency Vibration Noise Present in the Measurement Laboratory